Fall 2015

Coherence-based transmissibility as a damage indicator for highway bridges

Charles Joseph Schallhorn
University of Iowa

COHERENCE-BASED TRANSMISSIBILITY AS A DAMAGE INDICATOR FOR HIGHWAY BRIDGES

by

Charles Joseph Schallhorn

A thesis submitted in partial fulfillment
of the requirements for the Doctor of Philosophy
degree in Civil and Environmental Engineering in the
Graduate College of
The University of Iowa

December 2015

Thesis Supervisor: Associate Professor Salam F. Rahmatalla

Graduate College
The University of Iowa
Iowa City, Iowa

CERTIFICATE OF APPROVAL

_____

PH.D. THESIS

_____

This is to certify that the Ph.D. thesis of

Charles Joseph Schallhorn

has been approved by the Examining Committee for
the thesis requirement for the Doctor of Philosophy degree
in Civil and Environmental Engineering at the December 2015 graduation.

Thesis Committee: _____
Salam F. Rahmatalla, Thesis Supervisor

_____
Jasbir Arora

_____
Colby Swan

_____
Sharif Rahman

_____
Shaoping Xiao

Acknowledgements

I would like to thank my advisor, Salam Rahmatalla, for the opportunity, the patience, and the confidence in me that he has provided throughout this whole process.

I also wish to thank the members of my committee, Jasbir Arora, Colby Swan, Sharif Rahman, and Shaoping Xiao, who have aided in my advancement in knowledge.

Many thanks go to my parents, Tom and Char Schallhorn, for raising me to be whom I am today, and to the remainder of my family for their countless support.

Finally, I would like to give enormous praise to my wife and son, Kayla Weiss and Alexander Schallhorn, for putting up with me during this process and for giving me valuable critics and motivation that helped immensely.

Abstract

Vibration-based damage detection methods are used in structural applications to identify the global dynamic response of the system. The purpose of the work presented is to exhibit a vibration-based damage detection algorithm that calculates a damage indicator, based on limited frequency bands of the transmissibility function that have high coherence, as a metric for changes in the dynamic integrity of the structure. The methodology was tested using numerical simulation, laboratory experimentation, and field testing with success in detecting, comparatively locating, and relatively quantifying different damages while also parametrically investigating variables that have been identified as issues within similar existing methods. Throughout both the numerical and laboratory analyses, the results were used to successfully detect damage as a result of crack growth or formation of new cracks. Field results using stochastic operational traffic loading have indicated the capability of the proposed methodology in evaluating the changes in the health condition of a section of the bridge and in consistently detecting cracks of various sizes (30 to 60 mm) on a sacrificial specimen integrated with the bridge abutment and a floor beam. Fluctuations in environmental and loading conditions have been known to create some uncertainties in most damage detection processes; however, this work demonstrated that by limiting the features of transmissibility to frequency ranges of high coherence, the effect of these parameters, as compared to the effect of damage, become less significant and can be neglected for some instances. The results of additional field testing using controlled impact forces on the sacrificial specimen have reinforced the findings from the operational loading in detecting damage.

Public Abstract

The purpose of the work presented is to exhibit a damage detection algorithm that measures changes within a structure through a process of monitoring how the structure vibrates. The methodology was tested using computer modeling, laboratory experimentation, and field testing with success in detecting, comparatively locating, and relatively quantifying different damages while also investigating variables that have been identified as issues within similar existing methods. Among these variables include temperature effects, loading conditions, and sensor placement. The presented methodology shows that the damage indicator metric is more sensitive to effects of damage than from these geometric and environmental variables because of how the damage indicator is calculated.

Table of Contents

List of Figures

Chapter 1. Introduction

1.1. Purpose of Investigation

Thousands of old multiple-steel-girder bridges have been built in the US and are vulnerable to damage and cracking [1-3]. Considering that the US has over 500,000 highway bridges with a span over 25 ft [1], the traditional practice of structural inspection using human observers with local testing equipment such as tapping and mag-particle testing [4] will be very tedious and unsustainable process due to the inherent limitations and subjectivity of these approaches. The limitations of the current human inspection process and the critical health conditions of existing infrastructures have attracted public attention and have been an active area of research and development for the last several decades. This is due to the urgent demands for safer and longer-life structures and in response to sudden catastrophic failures. However, nearly all of these methods are still in their development stages and more research is needed to enable these methods to work under field conditions due to the random nature of the loading and environmental variation that brings various uncertainties to the dynamic response of the structure.

Aside from the challenges that arise from the environmental and loading conditions, damage detection methods have to work effectively with different types of damage including those resulting from complex stress distribution such as fatigue-type cracking. Fatigue cracking is common in many structures that work under vibration conditions. One major fatigue cracking issue is in steel-girder bridges, and it happens due to poor detailing and out-of-plane relative displacement, mostly in the web-gap area of the girder at the girder-floor beam (girder-diaphragm) connections. The out-of-plane motion is triggered by torsion of the girders as a result of bending in a plane perpendicular to the line of traffic. The deteriorated conditions of cracks on the current multiple-steel-girder bridge connections, including retrofitted bridges, may cause catastrophic consequences if the crack sizes grow beyond the acceptable limits and therefore may require immediate action by bridge repair planners and emergency responders.

Fatigue-type cracking can initiate and propagate quickly, thus causing critical deficiencies before the biennial visual inspection can identify and retrofit the structure. The implementation of retrofits to stop fatigue crack growth in steel-girder bridges has

shown variable success [5]. The stop-holes [6] retrofit, where holes are drilled at the tips of existing cracks, has been customarily adopted by many DOTs across the US as a common repair practice of highway bridges [4]. While the stop-holes method is effective in stoping fatigue crack growth, the choice of stop-hole sizes and locations relative to the crack tips may only temporarily hinder the propagation of the crack, leading to re-initiation [7]. Indeed, field studies [8,9] have shown that some of these cracks re-initiate around the stop-holes thus potentially causing a real danger to the integrity and safety of the bridges. While stop-hole retrofits reduce stress concentration at crack tips, such retrofits may generate a new map with different crack re-initiation and growth scenarios across the connection area, which may introduce great challenges to any structural health monitoring or damage-detection methodology [10].

1.2. Literature Review

Interest in damage-detection algorithms and health-monitoring systems has continually increased over the past few decades [11-15]. The goal of many of these applications is to determine the changes in the dynamic characteristics of a structure, using vibration-based methods [16] in order to objectively conclude whether or not damage has occurred. Vibration-based methodologies have become more popular with experimental and field applications due to their effectiveness in capturing changes in the dynamic response of the structure through non-destructive measurements [17-20]. In general, an ideal damage-detection system would address all four damage issues in bridges [21]: (1) detecting damage; (2) locating regions of damage; (3) quantifying the severity of damage; and (4) predicting remaining service life.

Among vibration-based damage-detection methods, algorithms based on changes in the modal parameters [17,22], the frequency response functions (FRF) [23], and modal curvatures [24,25] were heavily investigated with promising results using computer simulations and lab testing. However, these methods encounter major challenges when tested in field applications [12,26], especially with small local damage areas such as cracks on the web-gap area of the girder on highway bridges. One main reason behind this deficiency is that modal parameters and FRF contain global information and therefore will have difficulties detecting local changes in the response of the structure due

to damage [27,28] unless they are used with a very fine mesh of sensors. Another issue is the complexity of measuring the operational input excitation to the structure for the FRF calculation [29] and the limited capacity of the existing tools that can calculate modal parameters with a high degree of accuracy.

On the other hand, research has been conducted [29-32] showing the potential effectiveness of transmissibility in detecting damage within a system. The transmissibility contains valuable information about the dynamic characteristics of the structure, represented by the anti-resonance frequencies [29], and is therefore an effective, unbiased measure of local changes in the dynamic properties of the structure. This is triggered by the concept that transmissibility represents the response ratio between two degrees of freedom, and therefore the transmissibility is expected to be more sensitive to the local changes between these degrees of freedom than the FRF [28]. Still, the distance between these degrees of freedom, the size of the damage, the changes in the environmental parameters, the variability in the location and magnitude of the operational loading [27,32], and the existing level of noise will create uncertainties in detecting real changes in the dynamic characteristics of the structure in real field applications.

The decision process for detecting damage using the transmissibility function is normally represented by a damage index, which is traditionally based on changes in the transmissibility function for a given pair of sensors. For example, Worden [33] used the novelty index to detect damage by training a neural network architecture using features of the transmissibility function between two degrees of freedom of a spring-mass system. Also, it has been proposed [31,34] that one can use features around certain frequency bands or peaks of the transmissibility function. In a review article, Chesne et al. [19] discussed the effect of changing the input excitations on the characteristics of the transmissibility function; they also raised the issue of the sensitivity of limiting the frequency band of the transmissibility function on the damage index.

Kess and Adams [35] conducted a parametric study relating temperature, among other variables, and transmissibility in damage detection, and developed a variability test matrix that isolates the effect of each variability. The relationship between temperature and novelty index, which is based on transmissibility, is also well known [31].

Work has also been conducted to investigate the effect of force location and magnitude on transmissibility and furthermore transmissibility-based damage detection methodologies. The book chapter by Maia, et al. [28] discusses the derivation and properties transmissibility, including the characteristic in which the transmissibility can be independent from the applied force. In the same article [28], another attribute is described in that the transmissibility will remain unaffected by changes to the mass or stiffness at locations where the force is applied. The review by Chesne and Deraemaeker [19], however, utilized numerical simulations to discuss how the force location affects the damage detection methodology and found that damage localization was only possible when the force was near the damage location in non-dispersive systems, and that no localization could be attained for dispersive systems. Previous studies have indicated that operational and environmental parameters, among other things, are major sources of uncertainties in the dynamic response of structures [36-38]. The article by Sohn [36] gives an overview of variability types, such as temperature, boundary conditions, mass loading, and wind-induced variation, as well as methods and procedures to accommodate for these inconsistencies. Temperature has also been vaguely grouped with other parameters giving reason for possible sources of error within a damage detection methodology [39,40]. Work has been completed showing that force location and magnitude affect the structural dynamics of a system, furthermore affecting the damage detection methodologies [19,28]. Nonlinearity within damage detection algorithms has become increasingly popular with the advancement of technology and the demand for this type of analysis due to structures being constructed from lighter and thinner materials. An extensive review of nonlinearity in structural dynamics was compiled by Kerschen, et al. [38] and covers a large range of information regarding nonlinear system identification, detection, and characterization, as well as methods and applications for these parameters. The review article by Worden, et al. [41] details how the methodologies from nonlinear dynamics could be applied to structural health monitoring and damage detection of aerospace, civil and mechanical systems.

1.3. Contribution of This Work

A vibration-based damage-detection methodology is presented in this work, along with rigorous testing through numerical, experimental, and field analyses. The contribution of

the proposed methodology is to combine the transmissibility function, coherence function, and probabilistic schemes to construct a damage indicator that gives critical information about the health condition of a structure or mechanical system. While it is known that individually these functions and schemes are useful in structural health monitoring, it is the combination of these, mainly by utilizing the coherence function, which is unique. When constructing this methodology, the previously described uncertainty parameters were taken into account, as shown in Figure 1.

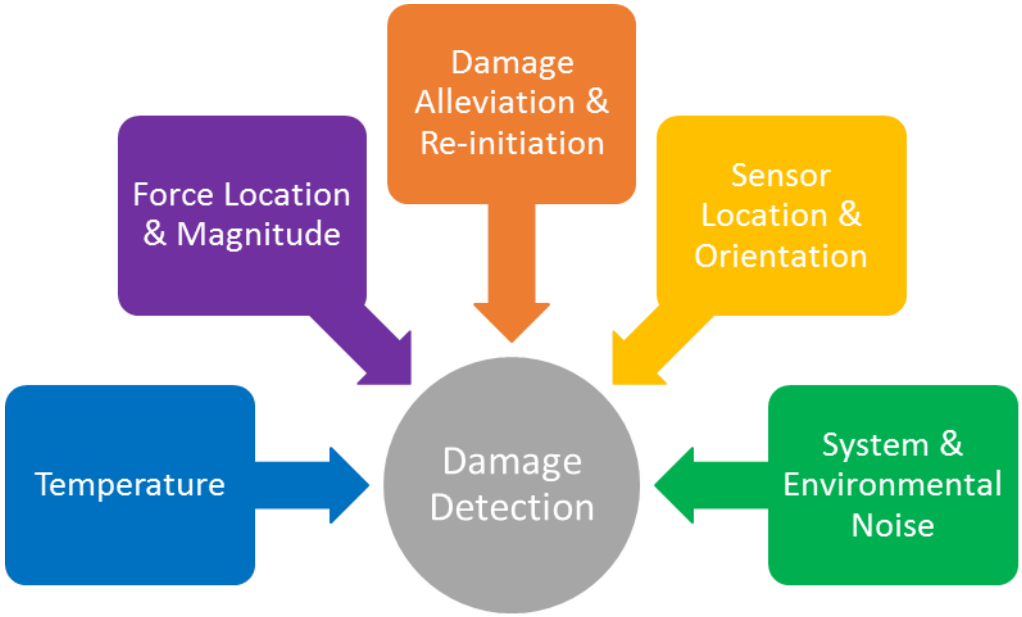

Figure 1 Uncertainty parameters investigated when constructing the proposed damage detection algorithm

Each of the items shown in Figure 1 is addressed in separate chapters throughout the entirety of this work, yet build on each other due to the interconnectivity of the presented damage detection algorithm. The contribution of the algorithm to be presented in this work is to limit features derived from the transmissibility function using a coherence function to create an effective methodology that is sensitive to local changes in structural response and is less susceptible to the aforementioned uncertainty parameters generated during numerical, experimental, and field applications. Chapter 2 will present the coherence-based damage indicator methodology and provide all relevant nomenclature and graphical examples to illustrate the process. Chapter 3 details the testing and

validation experiments for the proposed methodology. The presented experiments include impact testing of numerical models, experimental specimens, sacrificial specimens, and highway bridges, as well as operational load testing of sacrificial specimens and highway bridges, all of which aim to support the success of accurately detecting crack propagation and re-initiation. A parametric study on the effect of force location, boundary conditions, sensor location, and sensor orientation against the damage indicator is provided in Chapter 4. The study on the effect of temperature on transmissibility and the damage indicator is investigated in Chapter 5. Chapter 6 presents an overall discussion of the completed work, highlighting the important discoveries found throughout the completed testing.

Chapter 2. Coherence-Based Damage Indicator Methodology

2.1. Background Information

Thousands of existing, aging multiple-steel-girder bridges are vulnerable to fatigue cracking [2, 42-44]. This type of cracking can initiate and propagate quickly, thus causing critical deficiencies before the biennial visual inspection can identify and retrofit the structure. Fatigue cracking normally occurs due to poor detailing and out-of-plane relative displacement, mostly in the web area of the girder-diaphragm connections [45]. Figures from FHWA Publication No. FHWA-IF-13-020 depict common fatigue cracks that occur in steel-girder bridges, near the gap between the diaphragm (crossframe) and the girder web. The figures also show stop-hole retrofits with crack re-initiation. While stop-hole retrofit reduces stress concentration at crack tips, such retrofits may generate a new map with different crack re-initiation and growth scenarios across the connection area, which may introduce great challenges to any structural health monitoring or damage-detection methodology [10].

With a growing number of bridges in the US becoming structurally deficient or functionally obsolete, interest in damage-detection algorithms and health-monitoring systems has continually increased over the past few decades [15]. Vibration-based methodologies have become more popular in experimental and field applications due to their effectiveness in capturing changes in the dynamic response of the structure through non-destructive measurements [17-20]. Many approaches with the capability of sensing global changes in structural behavior have been introduced, such as those based on the changes in modal parameters [22, 46, 47], the frequency response function [23], and modal curvatures [24, 25]. However, many of these methodologies have shown to be limited when applied to complex structures, such as highway bridges, due to difficulties associated with accurately measuring excitation forces and predicting modal parameters [26, 48]. Therefore, the use of the transmissibility function has become effective in damage detection as it overcomes the need for input force measurement or subsequent modal parameter calculation. Extensive work [26, 29-32, 49] has been conducted showing the potential effectiveness of transmissibility in detecting damage within a system. The key concept for the effectiveness of these techniques is based on transmissibility representing the response ratio between two degrees of freedom in a

system, and is therefore expected to be more sensitive than the frequency response function to local changes in the dynamic characteristics of the system between these degrees of freedom [28]. When monitoring civil structures, such as highway bridges, this local sensitivity is preferred in order to increase the possibility of detecting relatively small crack-like damages, still, uncertainties in loading and environmental conditions will play critical roles in the decision-making process [49].

Along with transmissibility as a damage indicator, extensive works have also utilized control charts and statistical process control techniques that have been adapted for structural health monitoring and damage detection [52-56] and that deal with the uncertainty in the resulting data. The goal of most of these methods is to take a "real-time" look at whether or not a specific process is in control, or in the terms of structural health monitoring, whether or not different response features detect damage. Many of the works in this area have looked at the response of the structure in the time domain [52-54] as the process to be monitored. Although these methods and tests have shown potential in detecting damage in a controlled environment, the majority have been struggling to identify damage in real-life field applications.

The contribution of the algorithm to be presented in this work is to limit features derived from the transmissibility function using a coherence function and integrate these features with probabilistic process control techniques to create an effective methodology that is sensitive to local changes in structural response and is less susceptible to uncertainties generated in real-life field applications. This work strategically places sensors at damage-critical locations on the highway bridge and introduces a percent-violation that can assist bridge planners in their evaluation, maintenance, and decision making.

With complex types of failure in mind, the contribution of this work is to introduce a damage-detection algorithm with the capability of identifying crack growth and crack re-initiation near connections of structures with different initial conditions. Section 2.2 outlines the methodology and clarifies all the necessary background information. An alternative approach to the damage detection algorithm is presented in Section 2.3.

2.2. Explanation of Algorithm

Figure 2 shows the flowchart of the proposed vibration-based damage-detection algorithm. For purposes of clarification, an account of the data used within this algorithm as well as the terminology used to describe this data will be given. The majority of the experimentation completed in this work was based on impact testing in which the response due to an impulse loading of the structure was measured. A single impact is referred to as the acceleration response time-history for any predetermined length of time, preferably the length of time needed before the impact force dampens out of the structure. Two sets of data, each comprising a prescribed number of impacts, will be considered: baseline set (N impacts) and comparison set (M impacts). For many of the numerical analyses completed, the prescribed number of impacts (N and M) was one due to the repeatability of computational analyses. For the experimental analyses, the number of impacts varied in order to achieve a certain level of statistical significance for the current analysis. The baseline set is a collection of N impacts monitoring the state of the structure to which other states will be compared. Similarly, the comparison set is the collection of M subsequent impacts for which the state of the structure could be damaged or remain at the same state as the baseline set. A damage indicator will be introduced to give a numerical value to the damage detection. This damage indicator will be a comparable representation of each of the data sets so that damage detection can be objectively identified.

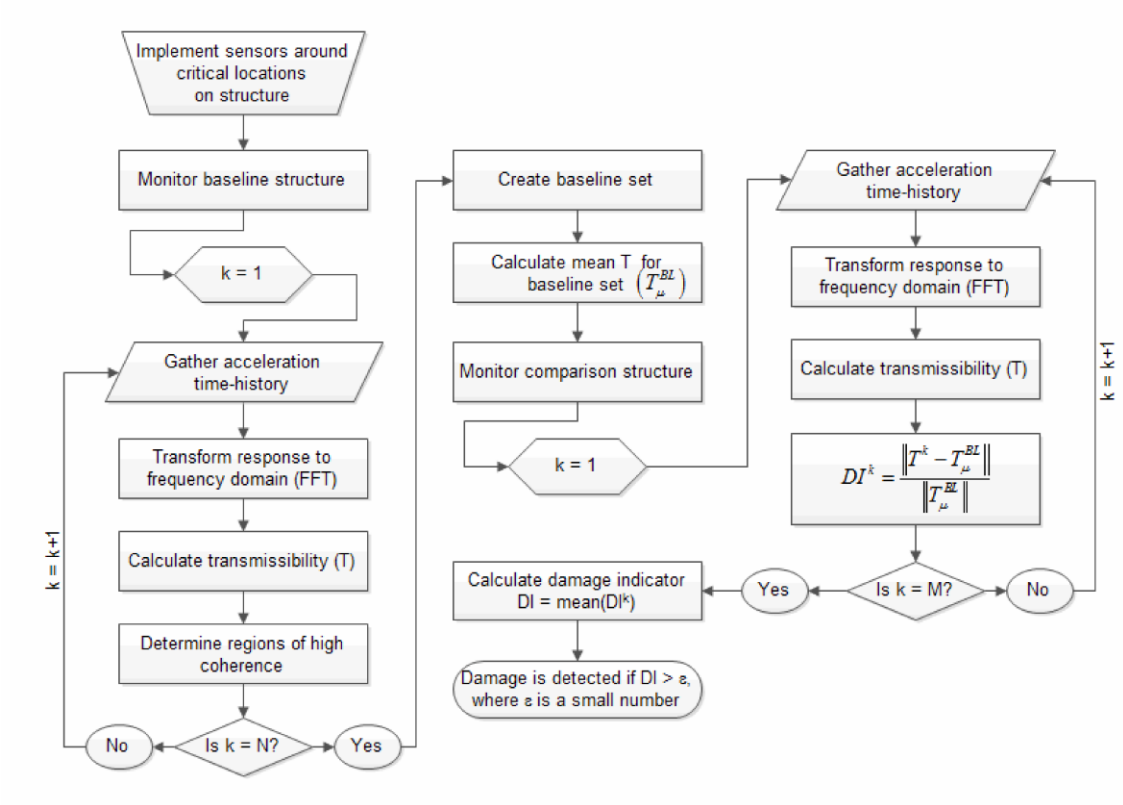

Figure 2 Outlined procedure for vibration-based damage-detection algorithm

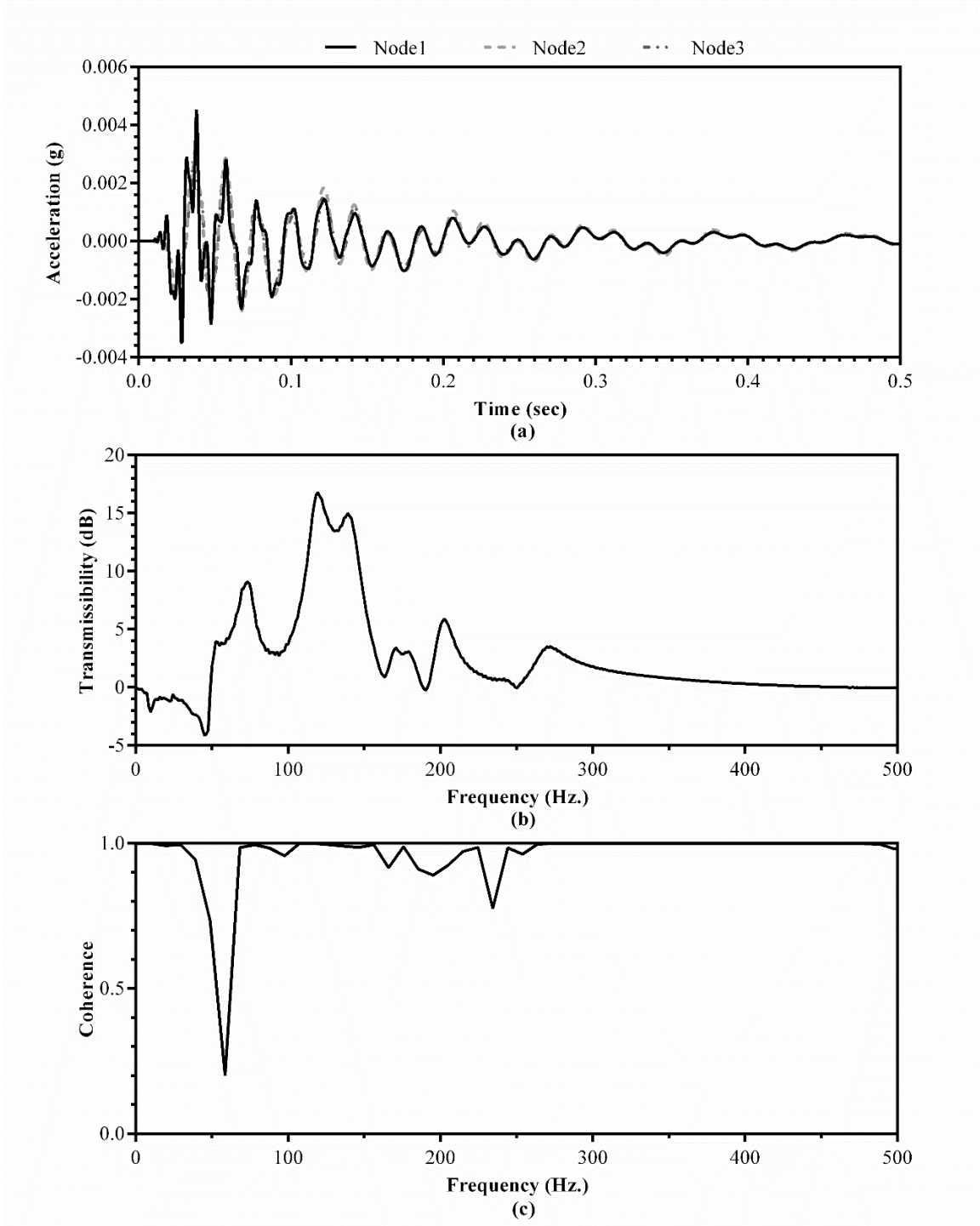

Figure 3 Typical plots of acceleration, transmissibility, and coherence: (a) acceleration response from three nodes of the numerical model (to be described later), (b) transmissibility calculated from the acceleration response in (a), (c) coherence calculated from the acceleration response in (a)

The algorithm starts, as shown in the upper left corner of Figure 2, by implementing sensors around critical damage-prone locations, such as connections, high-stress areas, etc. With such an arrangement, it is expected that the capacity of detecting small deficiencies will be increased, thus directly localizing the damage-detection algorithm.

Acceleration response time-histories from the sensors were collected based on an impact loading scenario. Typical acceleration responses are shown in Figure 3(a). The data files measure the acceleration both during and after the impact, consequently measuring the forced, transitional, and transient responses of the structural system. The time-history of the response data is then transformed to the frequency domain using a fast-Fourier transform (FFT). The transmissibility is then calculated as the ratio between two locations as shown in Equation (2.1). A typical transmissibility is plotted in Figure 3(b).

$$\mathbf{T}_{ij}(\omega) = \frac{\boldsymbol{X}_i(\omega)}{\boldsymbol{X}_j(\omega)} \tag{2.1}$$

where

$\boldsymbol{X}_i$ is the response in the frequency domain at location i

$\boldsymbol{X}_j$ is the response in the frequency domain at location j.

It has been shown [7, 34] that the transmissibility is more efficient when limited to certain frequency bands when detecting damage. Also, one can increase the accuracy of the decision process by limiting these bands [19, 31]. It is proposed in the current work that one can use the coherence between sensors' signals [49] to limit the frequency bands.

In this work, the coherence (Equation (2.2)), a measure commonly used in signal processing, was used to determine the linearity between two signals and to assess measurement quality. A typical plot of coherence is shown in Figure 3(c).

$$\gamma_{ij}(\omega) = \frac{\left|\boldsymbol{S}_{ij}(\omega)\right|^2}{\boldsymbol{S}_{ii}(\omega)\boldsymbol{S}_{jj}(\omega)} \tag{2.2}$$

where

γ_{ij} is the coherence between sensors at location i and j

S_{ij} is the cross-spectral density between sensors at location i and j

S_{ii} is the auto-spectral density of the sensor at location i

S_{jj} is the auto-spectral density of the sensor at location j

When the coherence value reaches one, this indicates an ideal linear relationship between signals; values less than one can indicate the existence of uncertainties and possible nonlinearity in the measurements. Therefore, by limiting the transmissibility to regions of high coherence, i.e., regions with coherence values near unity, it is expected that the damage-detection algorithm will function more efficiently.

The baseline set is generated after the prescribed number of impacts (N) are monitored. If the number of impacts that have been collected is less than the prescribed number, more responses are gathered following the same procedure. After the baseline set has been generated, the mean value of the transmissibility is calculated and stored for use in the calculation of the damage indicator. The comparison structure is then monitored for a prescribed number of impacts (M). For each impact, a damage indicator value is calculated by normalizing the difference between the transmissibility of the comparison impact and the transmissibility of the mean baseline impact for a given frequency range Ω, as shown in Equation (2.3).

$$DI^K = \frac{\left\| \boldsymbol{T}^D(\Omega) - \boldsymbol{T}_\mu^{BL}(\Omega) \right\|}{\left\| \boldsymbol{T}_\mu^{BL}(\Omega) \right\|} \tag{2.3}$$

where

DI^K is the damage indicator value for each impact

K is a counter for each impact

$\boldsymbol{T}^{D}(\Omega)$ is the transmissibility for the comparison impacts over the frequency range Ω

$\boldsymbol{T}_{\mu}^{BL}(\Omega)$ is the mean transmissibility for the baseline impacts over the frequency range Ω

The frequency range Ω was chosen based on the regions of high coherence set during the creation of the baseline set. After M impacts are monitored for the comparison structure, the damage indicator is calculated as the mean of all M damage indicator values for the comparison set, as shown in Equation (2.4).

$$DI = \frac{1}{M}\sum_{K=1}^{M} DI^{K} \tag{2.4}$$

The damage indicator produces a positive scalar value to be used as a comparable measure for detecting damage. For an ideal system, the damage indicator should produce a value of zero when the comparison set is the same damage state as the baseline set. Changes to the structural dynamics of the system, i.e., damage, will then increase the damage indicator.

2.3. Alternative Algorithm

In previous work completed by the author, an alternative approach to the damage detection methodology was simultaneously developed. In this section, the alternative vibration-based damage-detection algorithm is introduced. This algorithm incorporates the underlying mechanisms of the coherence-based methodology, with modifications to the indicator value calculation (in lieu of a damage indicator, the alternative algorithm utilizes a percent-violation, to be detailed in the following section). This alternative algorithm was utilized when analyzing the data collected during the field testing during the collaboration with IDOT and Iowa State University. The majority of the data has since been updated to the damage indicator methodology; however, some aspects of the field testing results do consider assumptions/protocols derived within this alternative algorithm, therefore a review of the percent-violation algorithm is necessary.

2.3.1. Nomenclature for Alternative Algorithm

For purposes of clarification, an account of the data used within this alternative algorithm as well as the terminology used to describe this data will be given. A *data file* refers to a single time-history of acceleration. These data files can be transformed and/or manipulated to obtain frequency responses or normalized signals. Similar to the coherence-based algorithm, two sets of data shall be referred to in the discussion of the alternative algorithm: *baseline set* and *comparison set*. The *baseline set* is comprised of a certain number of data files collected for the undamaged state. After collecting the required data from the baseline structure to build the baseline set, the baseline structure henceforth becomes the comparison structure. The comparison structure can be undamaged or damaged. The *comparison set* is all of the data files collected on the comparison structure and can include undamaged or damage states. A *feature* is defined as the difference in the transmissibility between baseline and damage states over a band of frequencies. A *feature norm* is the Euclidean distance of a set of features and is used when calculating the percent-violation.

2.3.2. Detailed Procedure for Alternative Algorithm

This section provides a detailed outline of the percent-violation algorithm, shown in Figure 4.

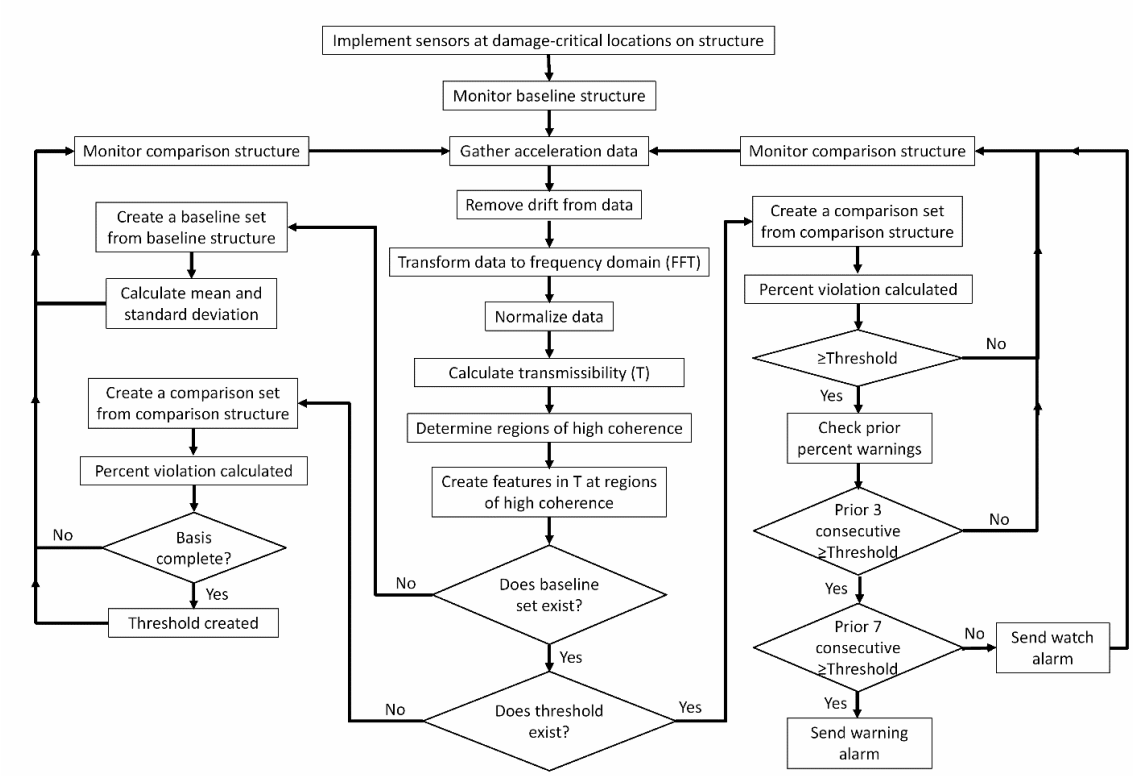

Figure 4 Outlined algorithm for alternative vibration-based damage-detection algorithm

The algorithm begins with the proper installation of sensors. Placing the sensors around damage-critical locations, i.e., connections, high-stress areas, etc., directly localizes the scope of the detection algorithm, thus improving the likelihood of detecting small deficiencies. With the sensors implemented in damage-critical locations, data can be collected for the appropriate loading scenario.

Depending on environmental and loading conditions, sensor type, and other factors, drift may occur during data collection. Drift was removed from the current data using the moving average algorithm (Equation (2.5)),

$$\hat{\boldsymbol{X}}_j[t,t+\delta t] = \boldsymbol{X}_j[t,t+\delta t] - \mu_{\boldsymbol{X}_j[t,t+\delta t]} \tag{2.5}$$

in which $\hat{\boldsymbol{X}}_j[t,t+\delta t]$ is a segment of the signal from time t to $t+\delta t$ with the drift removed, $\boldsymbol{X}_j[t,t+\delta t]$ is a segment of the original signal, and $\mu_{\boldsymbol{X}_j[t,t+\delta t]}$ is the average of the original signal for the segment from time t to $t+\delta t$.

The data is then transformed to the frequency domain using a fast-Fourier transform (FFT). Since the loading is random and will not be exactly the same experimentally, data normalization is used so a reasonable representation of the transmissibility can be determined. This is based on previous studies that showed the transmissibility to be sensitive to variations in the locations and magnitudes of the input force. For example, Johnson, et al. [31] used the mixed transmissibility ratio to avoid the effect of variations of the input force on the resulting damage features in the transmissibility. The signals are normalized at each frequency in the range of high coherence by using Equation (2.6).

$$\bar{\boldsymbol{X}}_j(\omega) = \frac{\hat{\boldsymbol{X}}_j(\omega) - \hat{X}_j^{\min}}{\hat{X}_j^{\max} - \hat{X}_j^{\min}} \tag{2.6}$$

where $\bar{\boldsymbol{X}}_j(\omega)$ is the normalized signal at location j, $\hat{\boldsymbol{X}}_j(\omega)$ is the signal with drift removed, $\hat{X}_j^{\min}$ is the minimum value of the signal, and $\hat{X}_j^{\max}$ is the maximum value of the signal. Without this normalization, the ratio of the response signal to the reference signal could be distorted based on loading conditions alone. Once the signals are normalized, the transmissibility function is calculated in units of decibel (dB).

Features for the damage decision can be calculated by discretizing transmissibility over a range of frequencies [31], as shown in Equation (2.7),

$$x^{\Omega} = \sqrt{\sum_{m}^{m+\Delta m} \left(\bar{Y}_m^{\Omega} - \mu_{\bar{Y}_m^{B}} \right)^2} \tag{2.7}$$

where x^{Ω} is the feature norm for the comparison set Ω, $\bar{Y}_m^{\Omega}$ are portions of transmissibility for the frequency range $[m, m+\Delta m]$ belonging to the comparison set Ω, and $\mu_{\bar{Y}_m^{B}}$ is the mean value of transmissibility for the baseline feature of the same range. The parameter m denotes that any value of frequency can be given for the feature range, and frequency bands of length Δm are used for the analysis. To limit these features and increase the accuracy of the algorithm, the magnitude of the coherence (Equation (2.2)) between sensor signals was used in selecting the feature range. The range of frequencies to be used is determined by the frequencies in which the coherence is high.

After limiting the features to the regions of high coherence, the baseline set and comparison sets are created. In order to compare the baseline set and a comparison set, a percent-violation is calculated. The percent-violation is an indication of the percent of feature norms in a given set that are statistically different from the baseline set of feature norms, and difference from the baseline set is classified as a violation. The decision for damage detection is calculated as $x^{\Omega} > 2\sigma$, where σ is the standard deviation of the baseline set, and determines how close the comparison signal must be to the baseline signal before damage should be detected. The standard deviation accounts for the variations in transmissibility due to noise, environmental and loading conditions, etc. This means that if a feature norm is greater than two standard deviations, this feature norm will be in violation (x^{η}). By compiling all of the feature norms for a comparison set, an overall assessment of damage detection can take place; it is shown as a percentage of all feature norms within the set that are violated. The equation used for determining the percent-violation is shown in Equation (2.8),

$$\Psi^{\Omega} = \frac{\chi}{\beta} * 100\% \tag{2.8}$$

where Ψ^{Ω} is the percent-violation for comparison set Ω, β is the number of feature norms (x^{Ω}) in comparison set Ω, and χ is the number of feature norms (x^{η}) in comparison set Ω that violate the given conditions.

To account for variations in the data due to uncertainties, such as environmental and loading effects, noise, etc., a threshold has been implemented in the algorithm. The undamaged structure is monitored for a specified period of time, using the first day as the baseline, and the percent-violation for each day is calculated. The number of percent-violations for this specified period of time is defined as the basis. The threshold is created by placing an upper bound on the percent-violations for the entirety of the basis, and this threshold is used for future percent-violations to be compared with.

Since extreme weather, traffic variations, or other uncertainties may arise causing the percent-violation to exceed the threshold, even for the healthy structure, the detection algorithm implements a check on the previous percent-violations to determine the

severity of the alarm to be sent. If the calculated percent-violation does not exceed the threshold, then no alarm is sent; thus, damage is not detected, and the algorithm can continue monitoring. If the percent-violation exceeds the threshold for three successive violations, then a watch alarm is sent, suggesting that damage is likely present but may not require immediate attention. If the percent-violation exceeds the threshold for seven successive violations, then a warning alarm is delivered because a significant change in the structure has occurred.

Chapter 3. Testing and Validation of Algorithm

In order to validate the coherence-based damage detection algorithm, numerous experiments were conducted utilizing specimens that exhibit realistic damage states. The first analysis was conducted numerically on a connection specimen that was designed to simulate the connection between a floor beam and the girder web of a bridge. This same specimen was then fabricated and tested experimentally in the lab. The final validation of the methodology was conducted using a sacrificial specimen in the field of similar proportions to the connection specimen under ambient traffic loading. The testing procedure and results from the analyses are described in detail throughout the remainder of this chapter.

It should be noted at this time that both the numerical and experimental testing of this algorithm were completed while conducting research for a project funded by the Mid-American Transportation Center (MATC). The goal of the research project was to identify whether or not cracks could propagate through a stop-hole retrofit, therefore the models and analysis account for detection of damage as well as investigation of crack propagation through retrofitting. The field testing portion was completed through a collaborative project with the Iowa Department of Transportation (IDOT), Iowa State University (ISU), and the University of Northern Iowa (UNI). The field testing was initially completed using the alternative percent-violation damage detection methodology, but has since been updated to the coherence-based algorithm. However a few assumptions/protocols from the alternative algorithm remain, e.g. creation of a threshold for use in watch and warning alarms.

3.1. Numerical Testing

A schematic depicting the layout and dimensions of the connection specimen used throughout this portion of the presented work is shown in Figure 5.

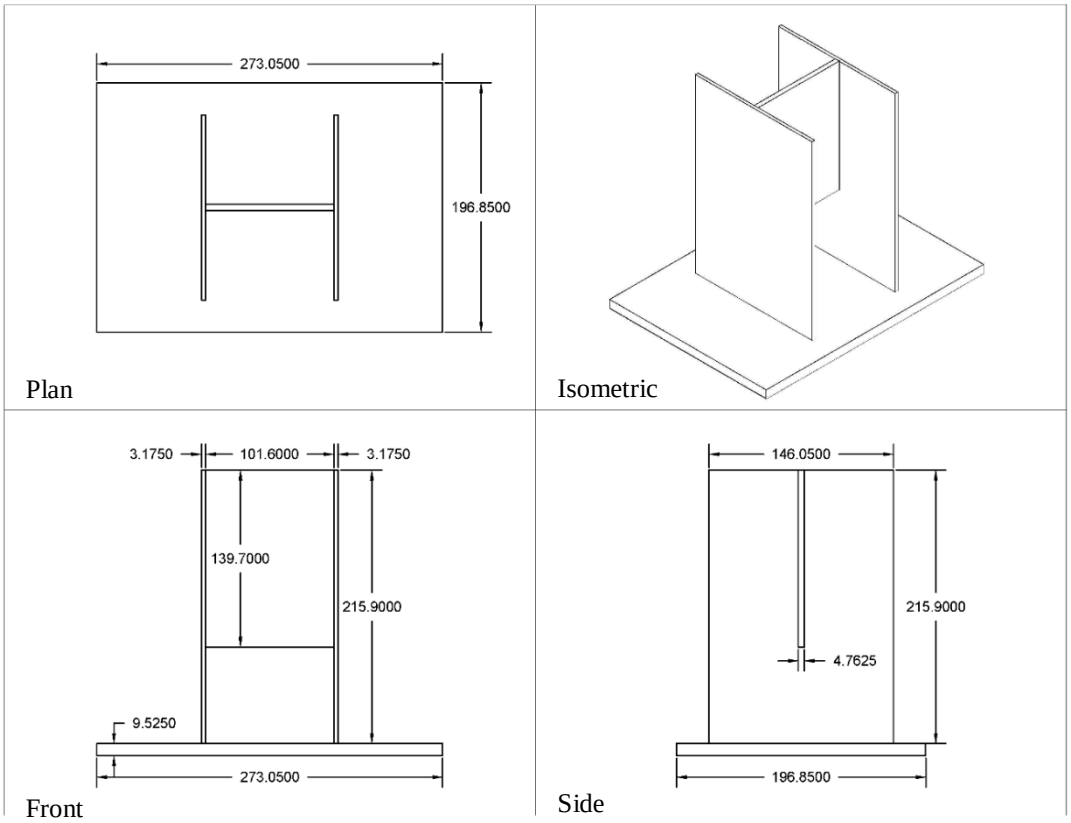

Figure 5 Layout and dimensions of specimen used for all analyses (all units are *mm*)

This model is 1/10 scale of the sacrificial specimen used by Iowa State University [50, 51] to represent a girder-floor beam connection that is common in steel girder highway bridges. The comparative representation between the connection and the numerical model can be seen in Figure 6.

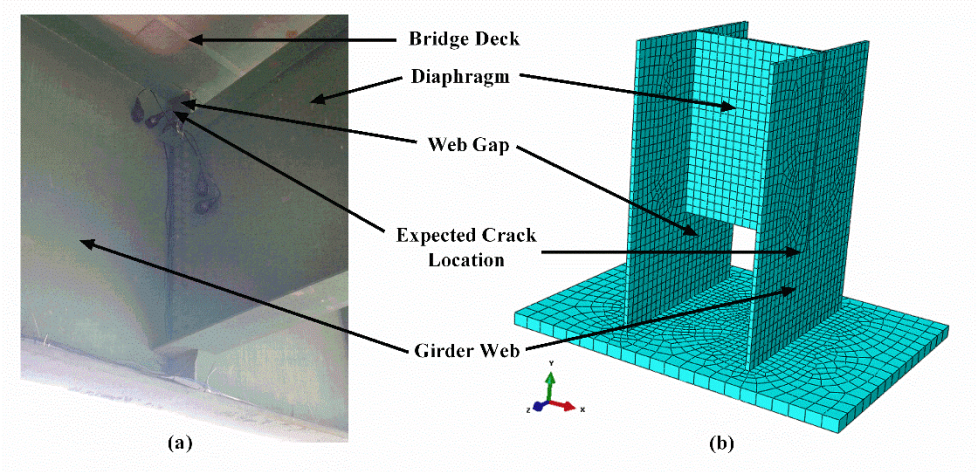

Figure 6 Finite element simulation of the connection between the web of the girder and the floor beam: (a) real highway bridge, (b) finite element model

3.1.1. Numerical Setup and Testing Procedure

A numerical analysis was completed to investigate the capabilities of the proposed algorithm in detecting damage on a complex structure. This analysis was conducted using a commercially available finite element program (ABAQUS 6.12, Dassault Systemes Simulia Corp.) in which the output acceleration data was exported into Matlab (MATLAB R2013a, The MathWorks Inc.) for use in the damage-detection algorithm.

The model of the specimen was created in ABAQUS (ABAQUS 6.12, Dassault Systemes Simulia Corp.) using general modeling techniques. The mesh consisted of approximately 3500 20-noded quadratic brick elements. Figure 7(a) depicts the setup for the numerical model, including the locations of the crack, the force, and the nodes used for monitoring the response of the system. Responses of all nodes were measured in a direction parallel to the direction of loading. Figure 7(b) depicts the meshing of the pseudo-girder web for the healthy state (D0). Figure 7(c)-7(g) depict the meshing of the same pseudo-girder web but for different damage states. Damage was introduced manually by modeling a seam crack through the thickness of the pseudo-girder web at the specified locations. The crack was modeled jagged to simulate a more realistic cracking scenario. The first damaged state (D1) has a 25 mm jagged crack originating at the bottom of the connection and extending toward one side of the specimen, as shown in Figure 7(c). The second

damage state (D2) was modeled by mirroring the first crack, as shown in Figure 7(d), thus giving a total crack length of 50 mm.

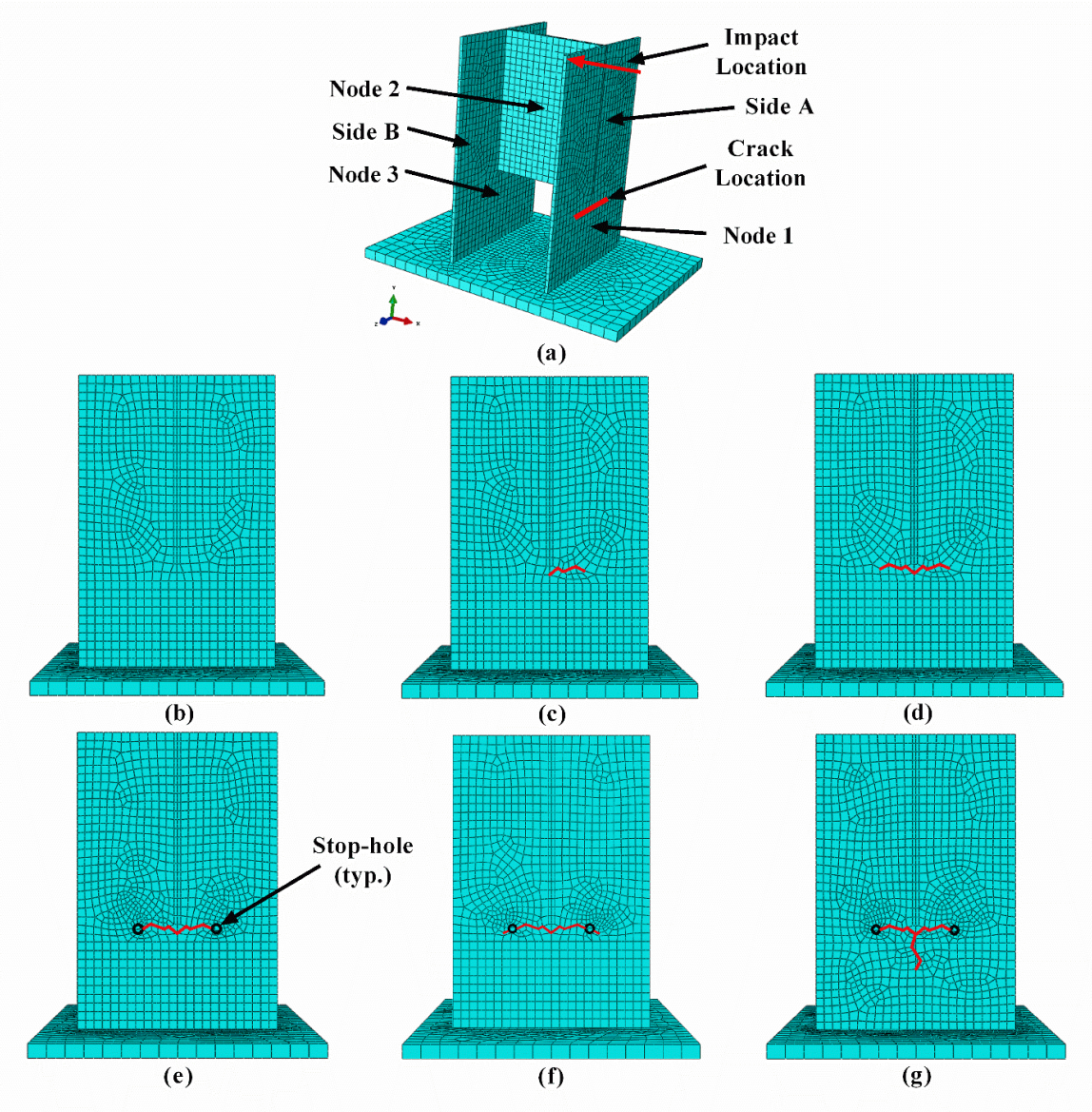

Figure 7 Numerical setup, crack location, and crack meshing: (a) isometric view depicting crack, force, and node locations, (b) mesh of Side A for D0, (c) mesh of Side A for D1, (d) mesh of Side A for D2, (e) mesh of Side A for D2H, (f) mesh of Side A for D3HA, (g) mesh of Side A for D3HB

While the purpose of this work was to determine whether or not any crack forming after a retrofit could be detected, 6 mm diameter holes were created at the crack tips of damage state D2, creating the retrofitted damage state D2H as shown in Figure 7(e) (where H

specifies that there are stop-holes in the model). The size of these holes are the scaled dimension of the common 25 – 50 mm hole size used for retrofitting steel-girder highway bridges [30]. Figure 7(f) and 7(g) depict the meshing of the pseudo-girder web in which the crack was propagated for the retrofitted damage states (D3HA and D3HB, respectively). Damage state D3HA (Figure 7(f)) was modeled by adding 6 mm seam cracks extending from the stop-holes of Figure 7(e) and represents cracks re-initiating through the retrofits. Damage state D3HB (Figure 7(g)) was modeled by a 25 mm jagged crack branching downward from the sharp notch in the middle of the existing crack of Figure 7(e), representing a crack branching from the initial retrofitted crack.

An impact analysis was completed within ABAQUS for each damage state. A unit impact force was applied in the location shown in Figure 7, and the acceleration responses at nodes 1, 2, and 3 in the direction parallel to the loading were measured before and after the impact, creating a 0.5 second time-history as shown in Figure 3(a). The acceleration time-histories were transformed into the frequency domain through a FFT (Matlab), and transmissibility (T) was calculated for symmetric pairs of nodes (2-1 and 2-3). The symmetric pairs of nodes are used because T should be identical for both pairs when measuring the undamaged state due to geometrical symmetry, and changes seen in one pair but not the other could possibly indicate damage location.

A static analysis was also conducted for each damage state to determine the stress concentrations within the model. In this case, a 45 N static force was applied at mid-span of the top of the pseudo-girder web as shown in Figure 8(a). The change in force location from the impulse force location allowed for a symmetrical distribution of loading, thus eliminating any skewed stress contours caused by offsetting the load. Figure 8(b)-8(d) show the stress contour plots for the healthy state (D0) and each of the non-retrofitted damage states (D1 and D2), while Figure 8(e)-8(g) show the stress contour plots for each of the retrofitted damage states (D2H, D3HA, and D3HB). A red-to-blue color map was used to depict high stress contours in red and low stress contours in blue.

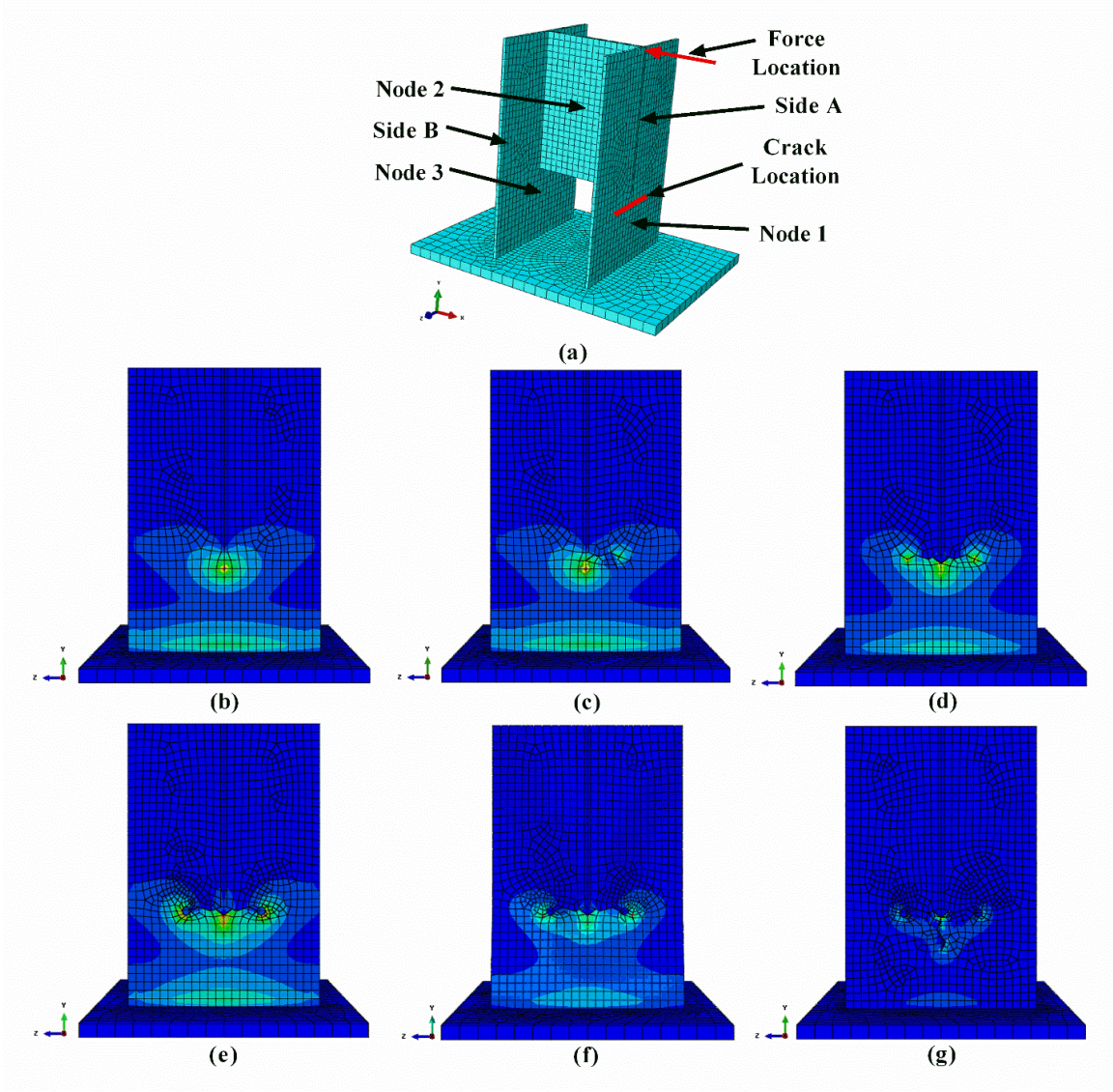

Figure 8 Numerical static analysis setup and stress contour plots: (a) isometric view depicting crack, force, and node locations, (b) stress contour plot on Side A for D0, (c) stress contour plot on Side A for D1, (d) stress contour plot on Side A for D2, (e) stress contour plot on Side A for D2H, (f) stress contour plot on Side A for D3HA, (g) stress contour plot on Side A for D3HB

As shown in Figure 8(b), a high stress concentration can be seen at the connection between the pseudo-girder web and diaphragm, thus justifying the expected location of a crack to initiate [51]. This stress concentration remains for the first damage state (D1) (Figure 8(c)) as well as the second damage state (D2) (Figure 8(d)), justifying the crack propagation.

Additional static analyses using the same procedures were conducted for each retrofitted damage state to determine how the stress concentrations would change after retrofits were applied to a cracked specimen.

3.1.2. Numerical Results

The damage indicator (Equation (2.4)) was calculated for each damage state to determine changes in the dynamic characteristics of the system from the baseline state. The purpose of this portion of the completed work was to detect crack re-initiation after retrofits. Therefore, two baseline sets were created: D0 was used as the baseline set for the non-retrofitted model, and D2H was used for the retrofitted model. By observing the damage indicator for the non-retrofitted model, crack initiation and growth was investigated. The frequency range (75-250 Hz) used in calculating the damage indicator was selected based on the coherence (Figure 2(c)) between pairs of nodes, per the damage-detection algorithm. The damage indicator results for the non-retrofitted specimen (compared to the baseline set D0) are shown in Figure 9(a), and the results for the retrofitted specimen (compared to the baseline set D2H) are shown in Figure 9(b).

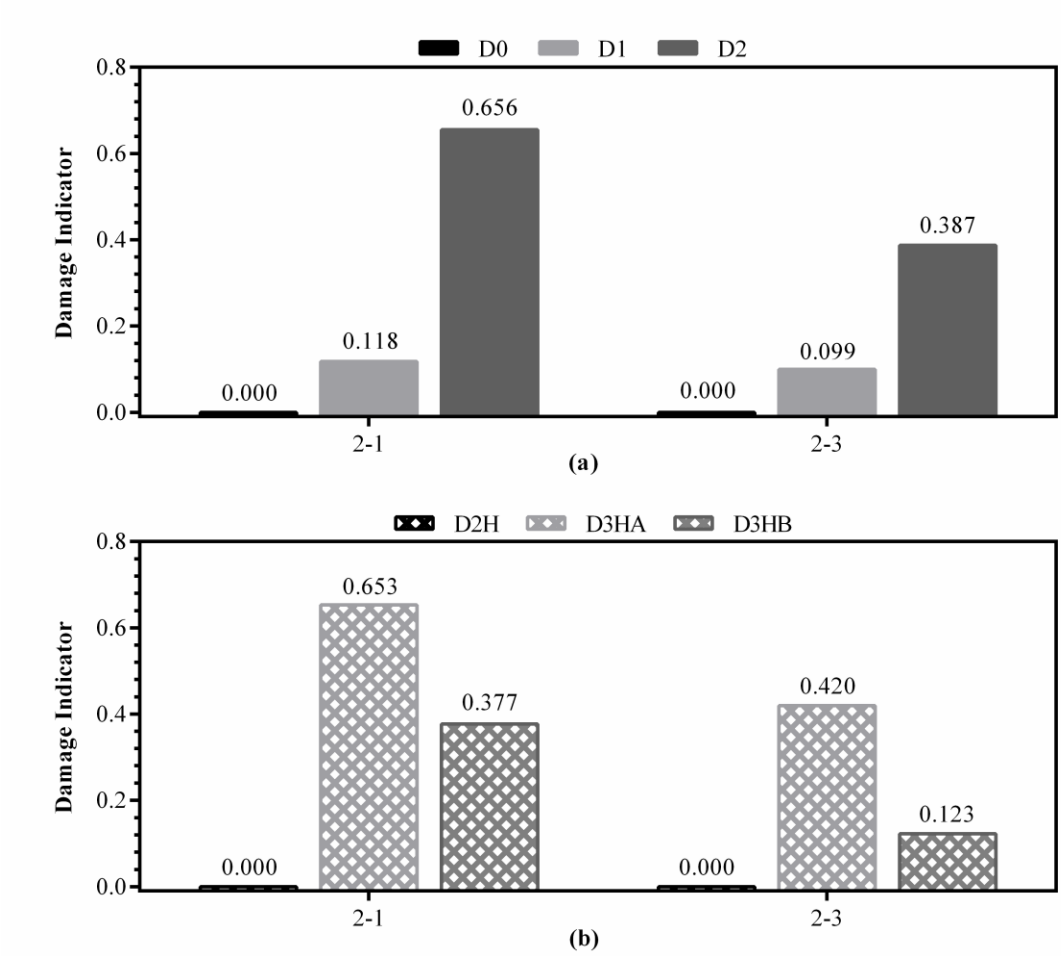

Figure 9 Damage indicator values of numerical analysis showing damage detection of multiple damage states for both sides (Side A: 2-1; Side B: 2-3) of the numerical models: (a) without stop-holes for baseline set D0 and comparison damage states D0, D1, and D2, (b) with stop-holes for baseline set D2H and comparison damage states D2H, D3HA, and D3HB

It can be seen that no damage is detected for the baseline state when compared to the respective baseline set of impacts (as seen by the damage indicator value of zero for D0 in Figure 9(a) and D2H in Figure 9(b)). Also, damage is clearly detected for all remaining damage states (as seen by the damage indicator values much greater than zero). It is observed for the non-retrofitted model (Figure 9(a)) that the damage indicator increases monotonically with damage, thus giving a relative quantification of the damage severity. It should be noted that Figure 9(b) depicts two non-sequential damage states

(D3HA and D3HB), and the damage indicator may not increase monotonically between these two states. Another observation shows that even though the damage indicator detects damage for both pairs of sensors, the magnitude of the damage indicator is greater for pair 2-1 than for pair 2-3, suggesting that damage can be comparatively located between nodes 2 and 1.

3.2. Experimental Testing

3.2.1. Experimental Setup and Testing Procedure

An experimental investigation of the same connection specimen was also conducted. The specimen was constructed with the same geometry shown previously in Figure 5 and was fabricated from structural steel (AISI 1080). All connections were professionally welded to increase the probability of having the damage occur in the pseudo-girder web plates of the specimen rather than in the welds.

Similar to the numerical analysis, impact testing was conducted to monitor the response of the specimen. The layout of the experiment, including impact location and accelerometer placement, is shown in Figure 10. A force hammer with a rubber tip was used as the excitation source. To minimize any uncertainties with the measurement quality, twenty impacts were monitored for each damage state.

Figure 10 Experimental setup of specimen showing sensor and impact locations

In order to test the damage-detection algorithm in dealing with a variety of damage scenarios, multiple damage states were investigated, including crack growth as well as crack re-initiation after a stop-hole retrofit. Damage was created by rigidly attaching a variable-speed vibrating motor (shaker) (model SCR-200, VIBCO Inc.) and vibrating the specimen at a specified frequency [51]. In order to rigidly attach the shaker to the specimen, two 13 mm diameter holes were drilled in one of the pseudo-girder webs (Side A in Figure 11) to fit the shaker's bolts. Additional masses (four 2.25 kg masses) were clamped on the specimen (Side B in Figure 11) in order to reduce the natural frequency of the specimen. An accelerated fatigue crack was generated by running the shaker near an adjusted natural frequency of the specimen.

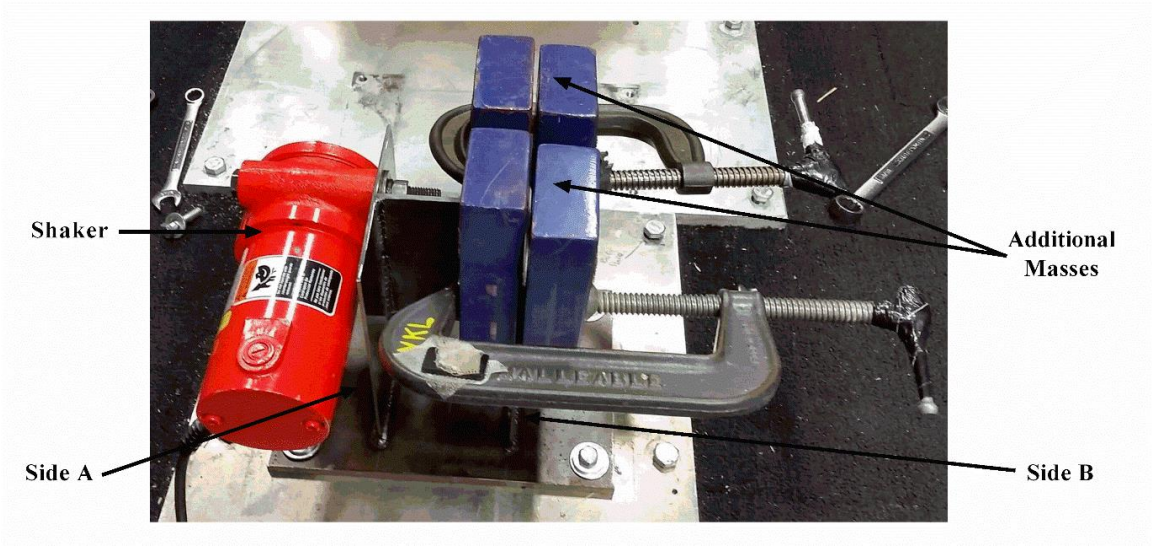

Figure 11 Experimental setup of specimen showing how damage was created

It is important to note that side A was considered as the pseudo-girder web on which the shaker was attached (requiring bolt holes), and side B was considered as the pseudo-girder web in which the additional masses were clamped. The crack was expected to form on side B in a similar location as depicted for the numerical analysis (Figure 7). Even though this expectation was observed by the crack in side B, it should be noted that a crack also initiated on side A. The crack on side A was likely caused by localized fatigue due to the shaker attachment.

The laboratory testing began by collecting twenty impact responses for the undamaged specimen. The shaker and additional masses were then attached (Figure 11). By shaking

the specimen near a natural frequency (approximately 53 Hz), large displacements were observed near the expected crack region. All of the damages created on side A of the second specimen are shown in Figure 12, and those created on side B are shown in Figure 13, along with an overall view of the respective side on which damage was observed.

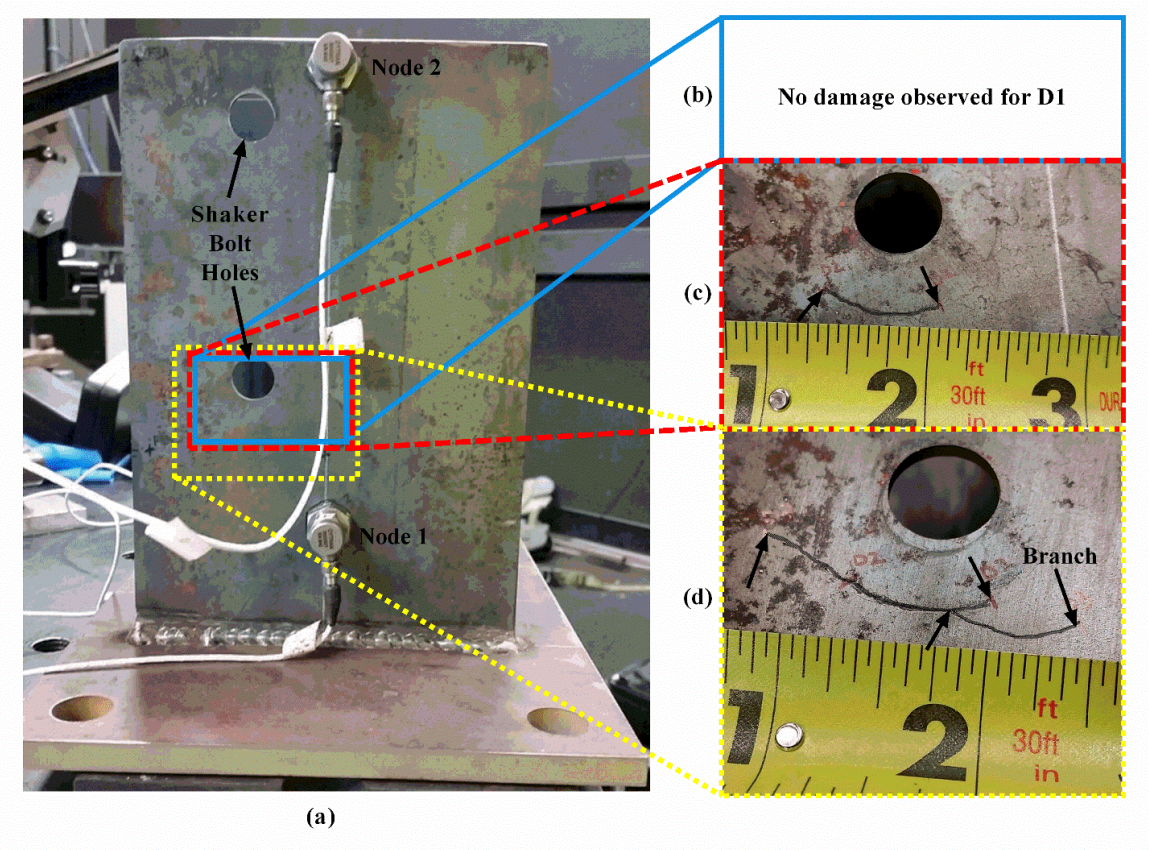

Figure 12 Damage caused on Side A: (a) overall side view indicating locations of damage, (b) no crack was observed (D1), (c) 19 mm crack (D2), (d) 32 mm crack with an approximately 19 mm crack branching from 6 mm in from the right crack tip (D3H)

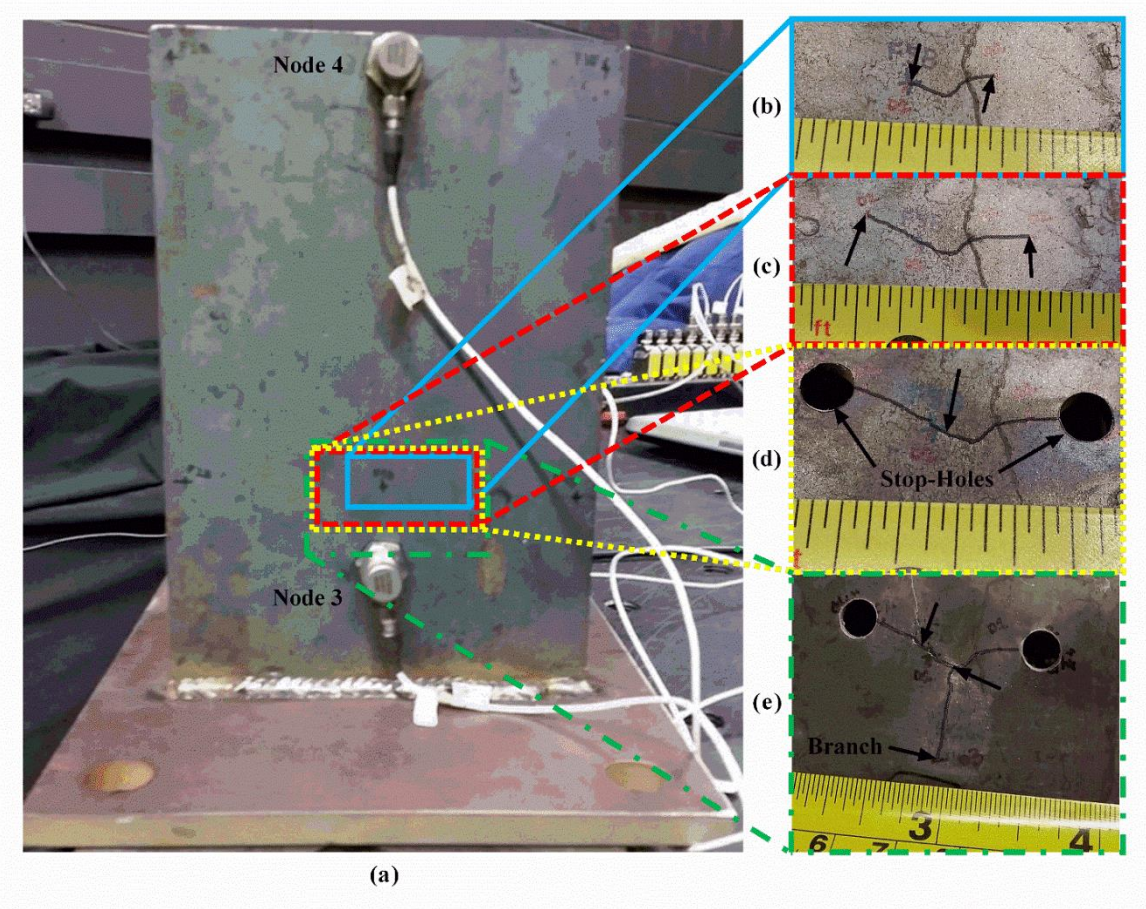

Figure 13 Damage caused on Side B: (a) overall side view indicating locations of damage, (b) 13 mm crack (D1), (c) 25 mm crack (D2), (d) 25 mm crack with 6 mm diameter holes drilled at crack tips (D2H), (e) 25 mm crack with 6 mm diameter holes drilled at crack tips and an approximately 13 mm crack branching from the middle of the 25 mm crack (D3H)

After approximately 5 minutes of shaking at this resonance, a 13 mm crack was observed on side B of the specimen (Figure 13(b)), with no damage observed on side A. The shaker and masses were removed, and the response of this damage state (D1) was monitored for twenty more impacts. The damage procedure of attaching the shaker and vibrating the specimen was continued for approximately another 5 minutes to propagate the damage. In this new damage state (D2), the crack on side B extended to a total of 25 mm long (Figure 13(c)), and a 19 mm crack was observed on side A (Figure 12(b)). The crack on side A was likely caused by localized fatigue due to the shaker attachment. The specimen was then retrofitted with 6 mm diameter stop-holes to alleviate the stress

concentration at the crack tips on side B. The position of the stop-holes with respect to the crack is shown in Figure 13(d). Twenty impacts were used to create a new baseline set of data for the retrofitted specimen (D2H). Damage was generated once more to propagate the crack after implementing stop-holes, creating damage state D3H (Figure 13(e)). The crack on side A propagated to a total length of 32 mm for D3H, with a 19 mm crack branching from it, approximately 6 mm from the right crack tip (Figure 12(d)). Throughout the experimentation, no crack was observed in which the crack re-initiated through the stop-hole.

3.2.2. Experimental Results

The damage indicator for symmetric pairs of sensors were calculated; however, since an accelerometer could not be placed at a location similar to node 2 of the numerical study (Figure 7), the pairs of sensors analyzed were nodes 1-2 and 3-4, based on the sensor numbering shown in Figure 10.

Figure 14(a) depicts the damage indicator for the damage states before the retrofit (D0, D1, and D2), with the healthy state (D0) taken as the baseline set. The range of frequency with high coherence was found to be 40 – 275 Hz. Similar to the numerical results, damage is not detected when comparing with additional impacts from the baseline state. The magnitude of the damage indicator for D0 (0.001 for both pairs of sensors) was not exactly zero due to uncertainties such as noise with the measurement quality. Also, damage is clearly detected for damage states D1 and D2 due to the damage indicator magnitudes being greater than zero. Due to the complexity of the cracking, a specific quantification cannot be calculated; however, a relative quantification can be determined by observing the trend, also seen numerically, in which the magnitude of the damage indicator increases monotonically with damage. This relative quantification allows one to distinguish the general severity of the damage. By applying the comparative damage location observation seen in the numerical analysis and by discerning that the magnitudes of the damage indicators for both D1 and D2 are larger between the sensors in pair 3-4 than between those in pair 1-2, it can be deduced that a greater damage occurred between the sensors in pair 3-4. This is consistent with the physical condition of the specimen, as seen by the magnitudes of the cracks in Figure 12

and Figure 13; therefore, this observation gives rise to comparative damage location within the algorithm.

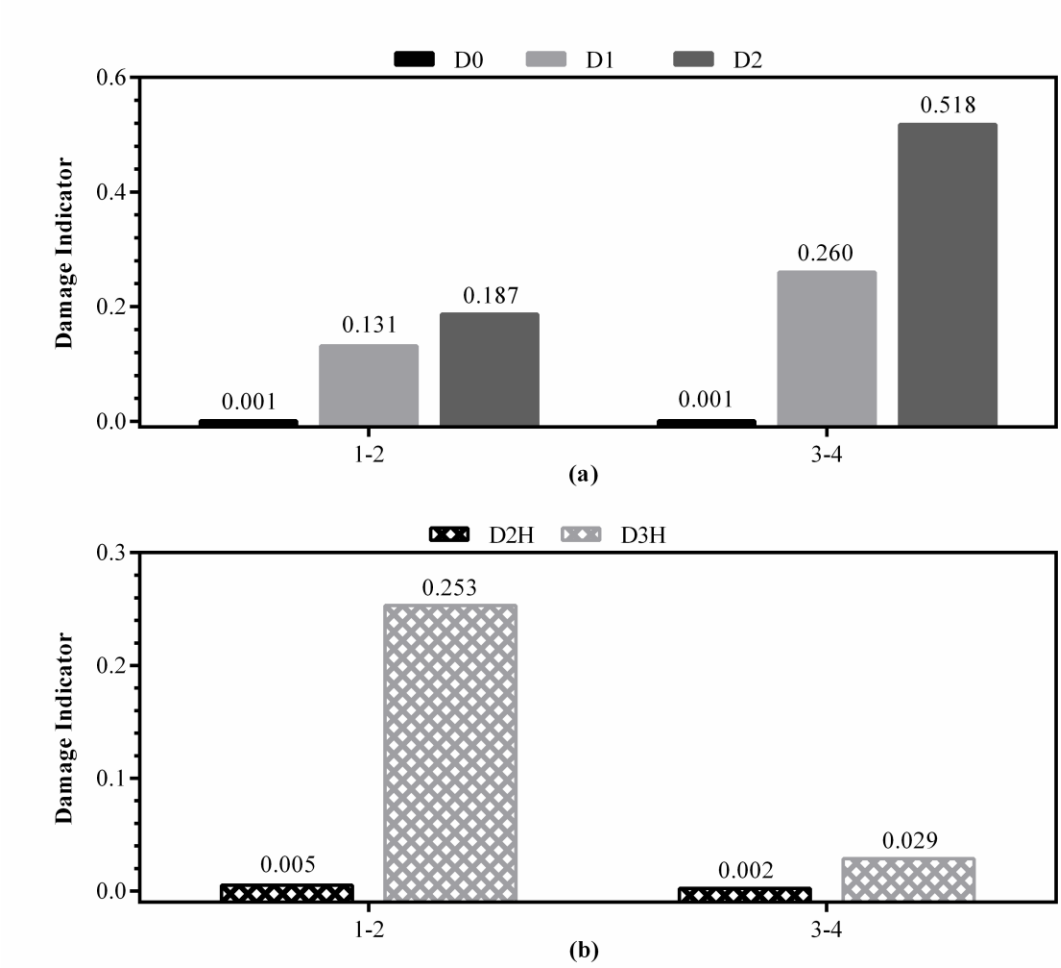

Figure 14 Damage indicator values of experimental analysis showing damage detection of multiple damage states for both sides (Side A: 1-2; Side B:3-4) of the experimental models: (a) without stop-holes with baseline D0 and comparison damage states D0, D1, and D2, (b) with stop-holes with baseline D2H and comparison damage states D2H and D3H

Figure 14(b) also shows accurate detection and comparative location for the retrofitted specimen (D2H and D3H), excluding relative quantification due to the lack of additional damage states. For these retrofitted analyses, the baseline set was taken as D2H. From

Figure 12(d) and Figure 13(e), it is seen that the damage on side A propagated further than the crack on side B during D3H. This observation confirms the results seen in Figure 14(b) in which the magnitude of the damage indicator for D3H is greater between the sensors in pair 1-2 than between those in pair 3-4.

3.3. Field Testing

3.3.1. Field Setup and Testing Procedure

In this section, a depiction of the locations and structural members used throughout this portion of the work completed will be given. All of the field experiments for this project were conducted under the south span of US 30 near Ames, Iowa. A schematic of this bridge and the experiment locations are shown in Figure 15. This overpass is a two-lane steel girder highway bridge with both lanes of traffic traveling in the same direction.

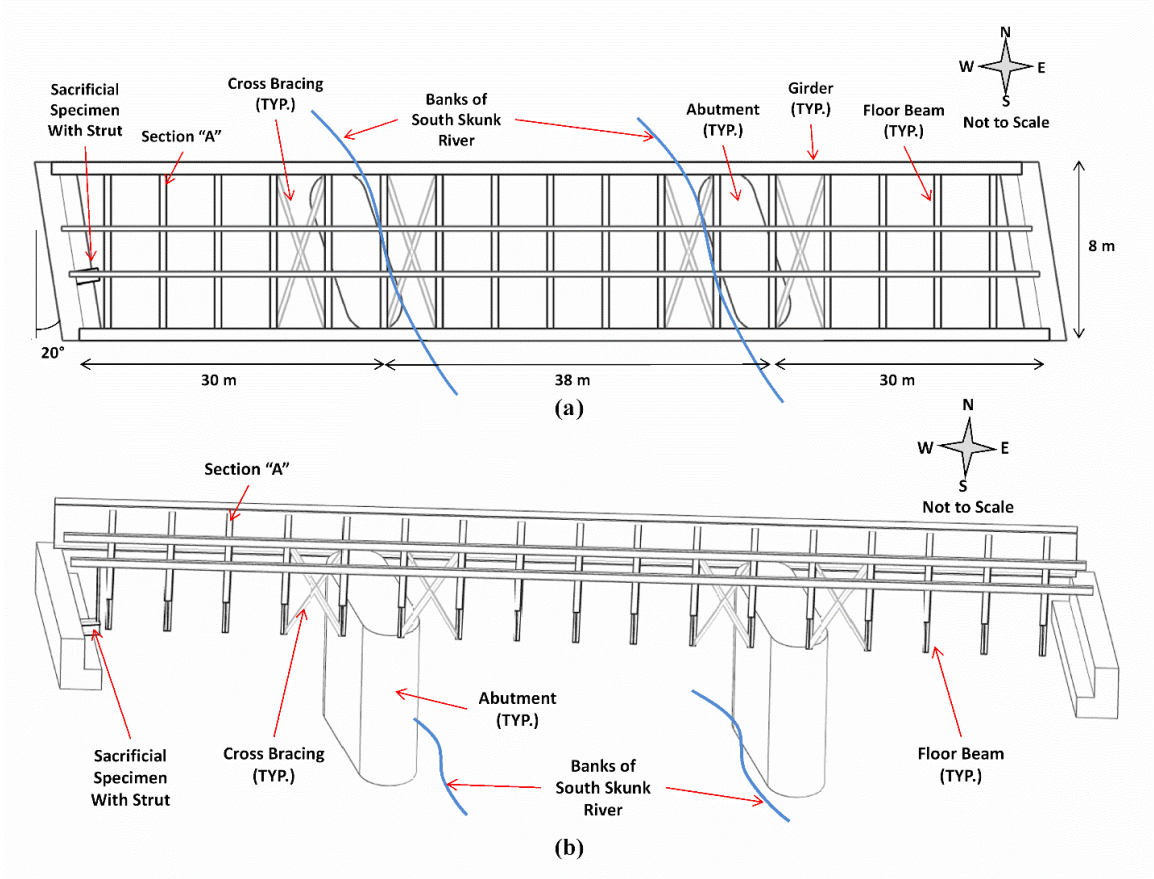

Figure 15 Schematic layout of south span of US 30 bridge depicting locations of field experiments (a) plan view with overall dimensions (b) isometric view depicting

location of sacrificial specimen with strut (Note: decking and south girder are not shown in (b) for clarity)

3.3.1.1. Sacrificial Specimen Setup and Operational Load Testing

The first analysis was completed on a sacrificial specimen shown in Figure 16. Also shown in this figure are the labels and locations of the accelerometers (sensors) implemented on the specimen. The sacrificial specimen [50] consisted of three plates of structural steel welded to each other, similar to the fabrication of a custom built-up I-beam. The location of the specimen was selected for practicality and convenience so it could be rigidly secured to the south abutment of the bridge using eight bolts. A strut was installed between the upper plate of the specimen and the floor-beam above the specimen. With this configuration, it is expected that the operational traffic load will transfer from the bridge deck via the floor beam directly to the specimen.

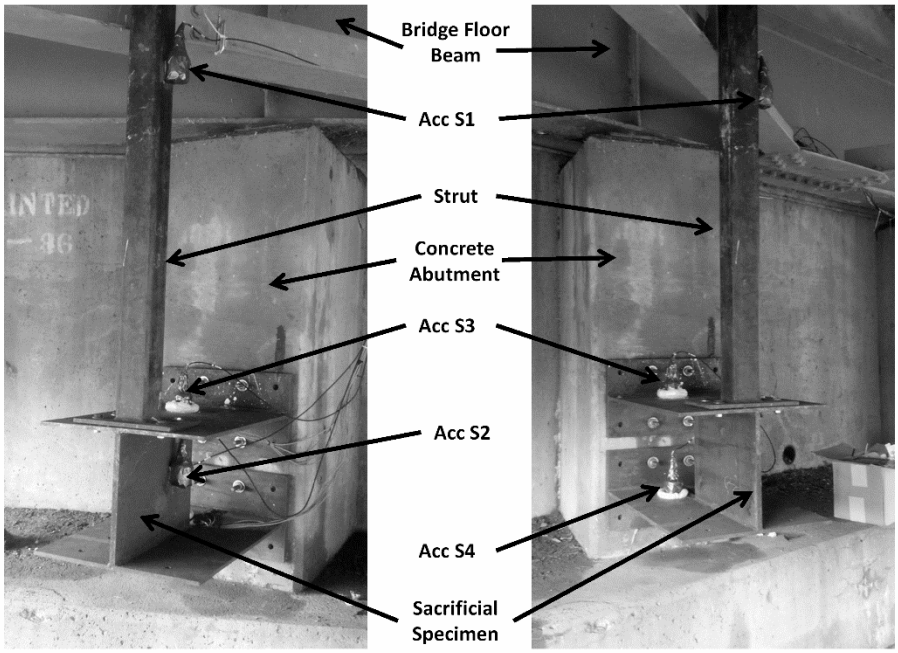

Figure 16 Sensor locations and orientations on the sacrificial specimen

The sacrificial specimen was designed to simulate a typical floor beam-girder connection found on highway bridges [50], as shown in Figure 17. Fisher [42] and Phares et al. [50] have shown that the out-of-plane motion seen during operational loading causes bending

of the girder web between the bridge deck and the floor beam, thus creating fatigue cracks in this location. Detailed depictions of a double-curved beam that represents the bending motion of the specimen and furthermore justifies the location of crack initiation are provided by Pohlkamp [51]. The purpose of this specimen was to monitor operational loading from a bridge to determine if cracks can be detected, while also allowing for different levels of damage to be created within the specimen in a controlled manner and without affecting the structural integrity of the bridge. Sensors were located around the areas of potential damage based on prior knowledge and previously published work; however, the proposed locations of the sensors may not be optimal. Three sensors (Acc S2, Acc S3, and Acc S4) were rigidly attached to the specimen, while a fourth sensor (Acc S1) was attached to the strut. All sensors were installed to measure the vertical acceleration of the specimen due to the loading being vertical. Acc S3 and Acc S4 were installed 20 to 30 cm from the abutment (representative of the bridge deck) and 5 to 7.5 cm from the center of the width of the specimen on the top of the plates representing girder webs. Acc S2 was implemented on the mid-span and mid-height of the pseudo-floor beam, and Acc S1 was installed at mid-height of the strut. The sensors used for the entirety of the completed work were 0.5 g range DeltaTron uniaxial seismic accelerometers (Bruel and Kjaer).

In addition to the accelerometers used for this testing, a thermocouple was implemented on a floor beam near the sacrificial specimen in order to collect the temperature of the steel floor beam under the bridge.

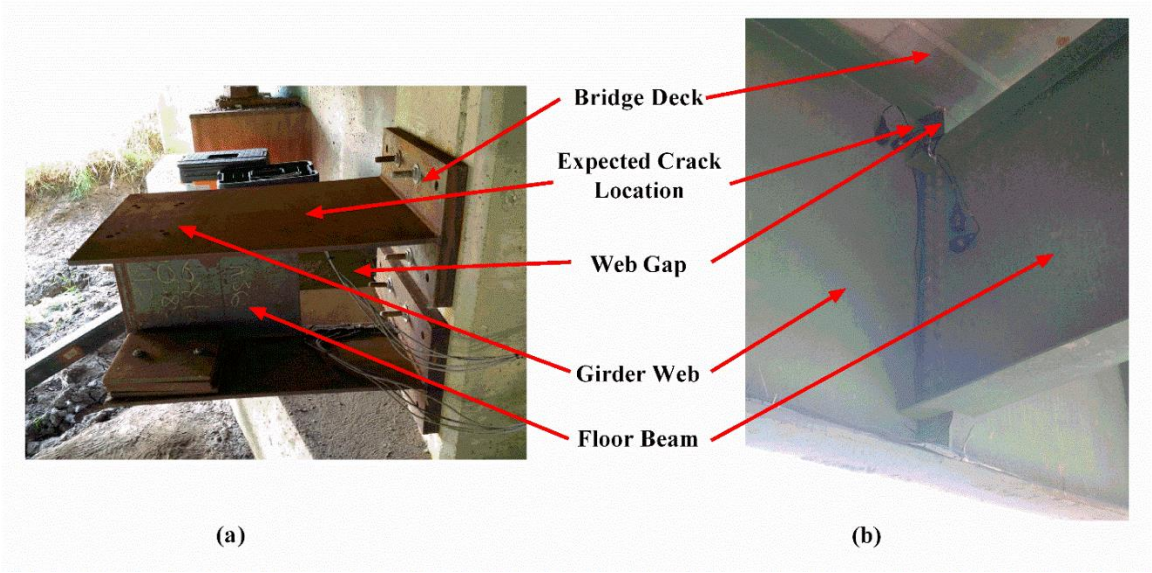

Figure 17 Representation of sacrificial specimen in terms of girder-floor beam connection

The sensors described in the previous section were used to continuously monitor the response of the bridge, and the data was stored locally in the data acquisition hardware. Data files consisting of one-minute intervals of traffic data for all sensors were transmitted automatically from the local hardware to a secured network location, allowing for remote access to and usage of the data [58, 59]. A typical data file for acceleration is shown in Figure 18, depicting the response of the bridge due to vehicles travelling over it. Figure 18a shows the vertical acceleration of sensor S2 on the specimen, while Figure 18b shows the vertical acceleration of sensor A5 on Section A.

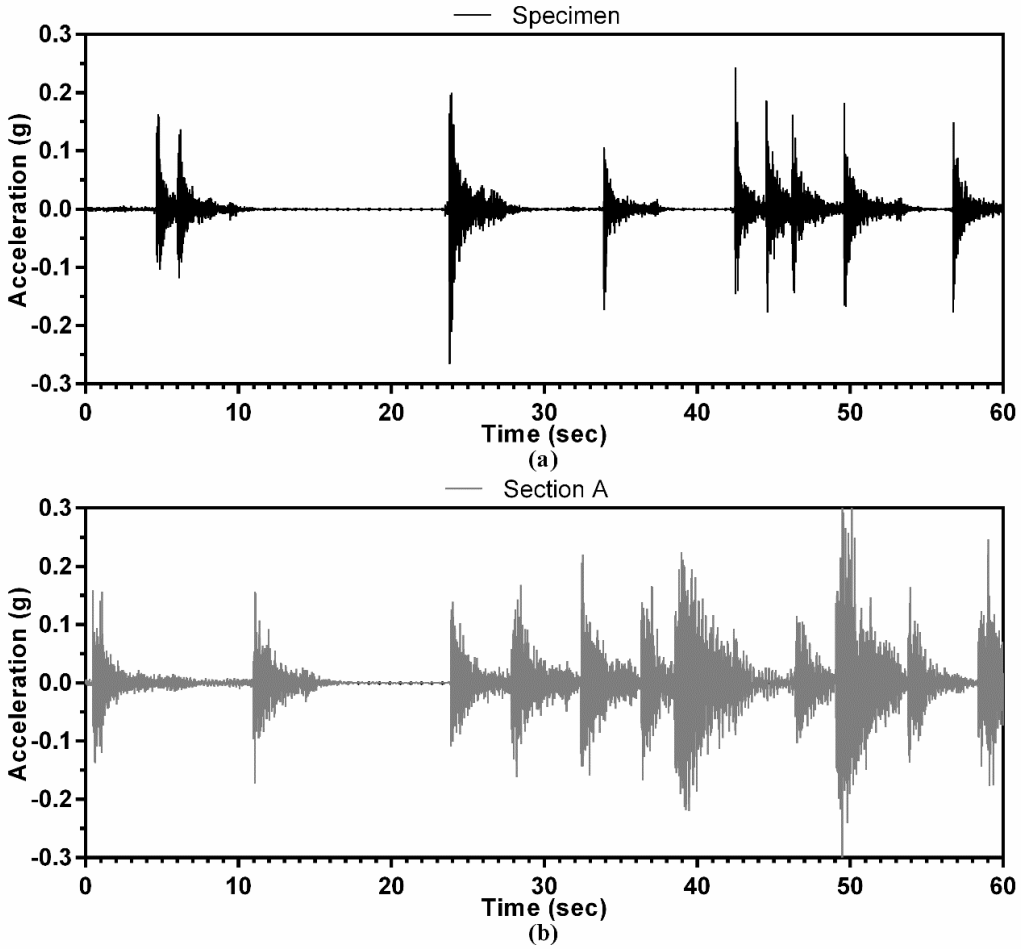

Figure 18 Typical time-history of vertical acceleration from one-minute data file for traffic loading on bridge (a) acceleration from S2 on specimen (b) acceleration from A5 on Section A

Each of these data files was then compiled (by day or 1440 files) in a commercially available software package (MATLAB R2013a, The MathWorks Inc.) to be used in the presented algorithm. One of the steps of the algorithm is to calculate the transmissibility from the acceleration time-histories. An example of the transmissibility calculated from the same data used in Figure 18 is shown in Figure 19. Figure 19(a) depicts the transmissibility between sensors S1-S2 for the sacrificial specimen, and Figure 19(b) depicts the transmissibility between sensors A5-A1 for Section A.

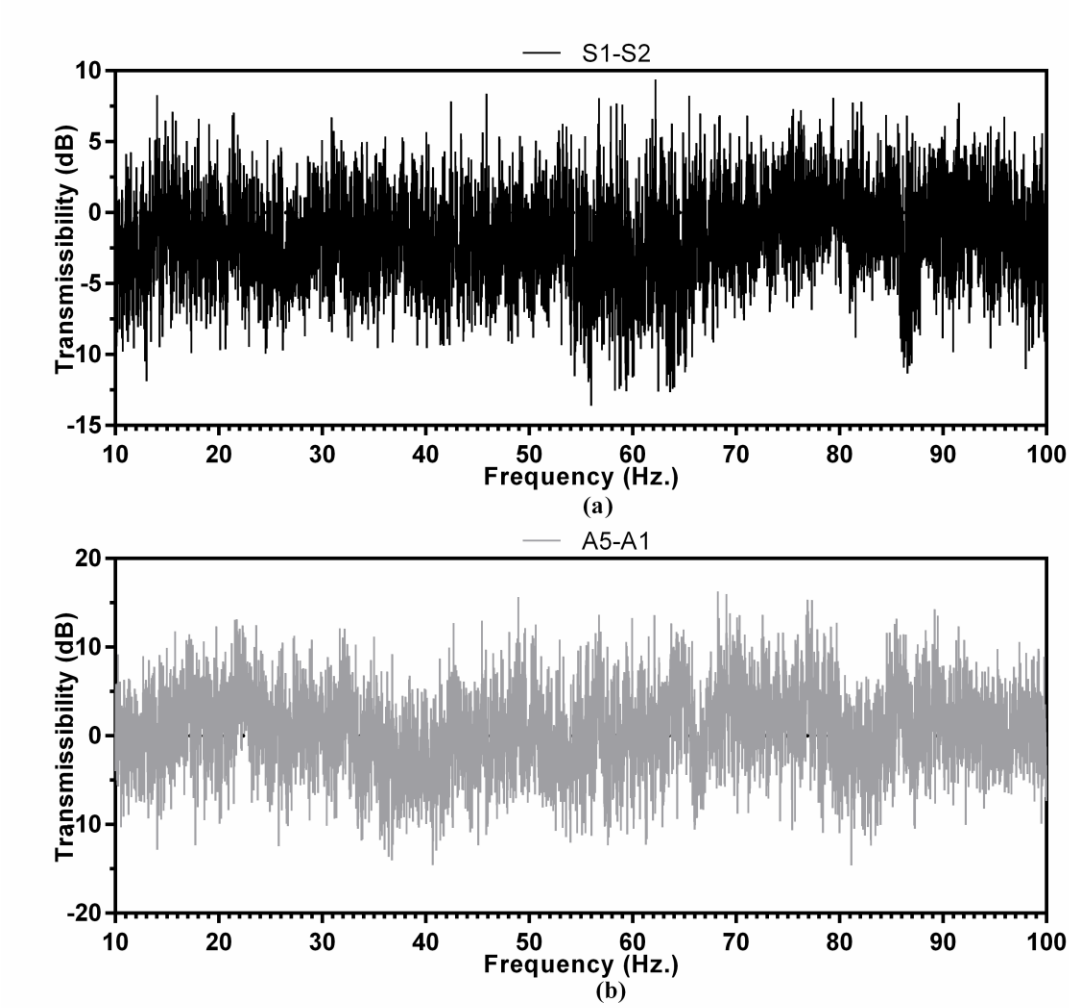

Figure 19 Typical transmissibility from pairs of vertical acceleration from one-minute data file for traffic loading on bridge: (a) transmissibility from S1-S2 on specimen (b) transmissibility from A5-A1 on Section A

The data for the sacrificial specimen started on 13 September 2012 and ended on 6 November 2012 and consists of 38 non-consecutive days of data. A total of 38 days of data, non-consecutive, were used for the analysis of Section A, beginning on 27 November 2012 and ending on 11 March 2013.

Data was collected for two weeks for the undamaged sacrificial specimen in order to create a baseline set. Of these two weeks of data, one day (24-hour period from midnight to midnight, a collection of 1440 one-minute files) was designated as the baseline set (14 September 2012), to which all other days of data were compared. After the initial two

weeks of data collection, damage was introduced into the sacrificial specimen by an accelerated cracking procedure. This process included removing the strut (so as to not cause damage to the bridge), placing a vibrating variable-speed motor on the specimen, vibrating the specimen close to its natural frequency until a crack initiated a certain amount, then replacing the strut [50]. With these arrangements, the crack was initiated at the expected location on the specimen. An additional two weeks of data was collected for this damage state, and then damage was propagated using the same procedure as the crack initiation. This two-week cycle continued until a total of three damages were completed and eight weeks of data was collected. Figure 20 shows the propagation of the crack at the expected location on the top plate of the sacrificial specimen near sensor S3 (Acc S3 in Figure 16) for each damage state; the crack tip locations are marked and labeled for the purpose of monitoring the crack growth. The crack was easily identifiable in Figure 20(a) and Figure 20(b); however, a mag-particle test [50] was conducted for the final damage state (D3) in order to more accurately depict the crack location. The residual magnetic powder outlining the crack is shown in Figure 20(c). For the purposes of understanding the effective size of the crack generated, Figure 20(d) is shown to depict the overall width of the sacrificial specimen with respect to the final damage state; the arrows point to the crack tip locations.

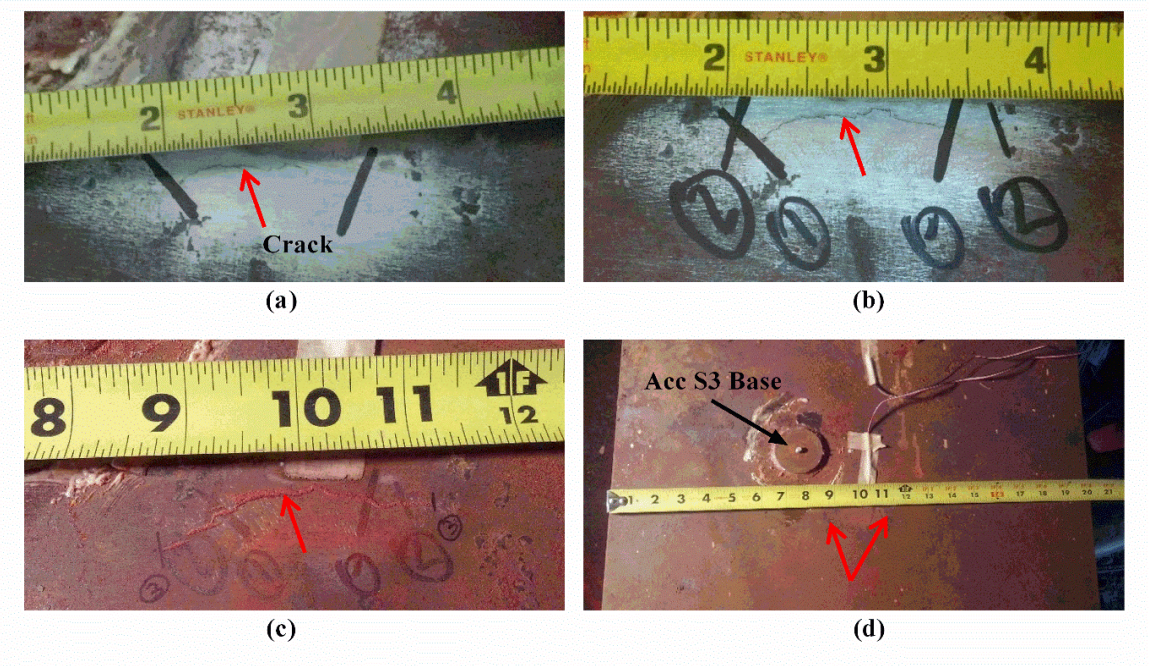

Figure 20 Crack created in sacrificial specimen: (a) D1 – 30 mm crack length, (b) D2 – 40 mm crack length, (c) D3 – 60 mm crack length, (d) overall view of specimen with respect to D3

3.3.1.2. Sacrificial Specimen Setup and Impact Load Testing

On the days when damage was created or propagated, an impact analysis was conducted on the sacrificial specimen without the strut attached in order to measure response data in a more controlled manner. These impact analyses were conducted by hitting the specimen with a rubber-tipped hammer. It should be noted that the impacts were to be used as the source of excitation for the testing, and not in FRF calculations, so the force was not recorded. Each test consisted of approximately fifty impacts in order to obtain statistical significance [60, 61]. Two tests were conducted on the same day that damage was created: one before the damage and one after the damage.

More details on the data collection can be found in Volume II of Iowa Highway Research Board (IHRB) Project TR-636 [59].

3.3.1.3. Section A Setup and Operational Load Testing

The second arrangement for testing was for data to be collected for a beam-girder connection at Section A of the bridge (Figure 15) under operational loading conditions.

The layout and labels of each of the sensors used for this analysis are shown in Figure 21, which depicts the northern half of Section A. The girder is 1.9 m deep, and the floor beam is 1.3 m deep. Sensors Acc A1 and Acc A2 were placed about 15 cm west of the connection, at the same height as the top of the floor beam. The remaining sensors were placed at mid-height of the floor beam, with sensors Acc A3 and Acc A4 about 30 cm south of the connection and sensors Acc A5 and Acc A6 at midspan of the floor beam (4 m south of connection). The odd-numbered sensors were oriented vertically (in the direction of loading), and the even-numbered sensors were oriented laterally (perpendicular to the direction of loading) and normal to the web of the north girder.

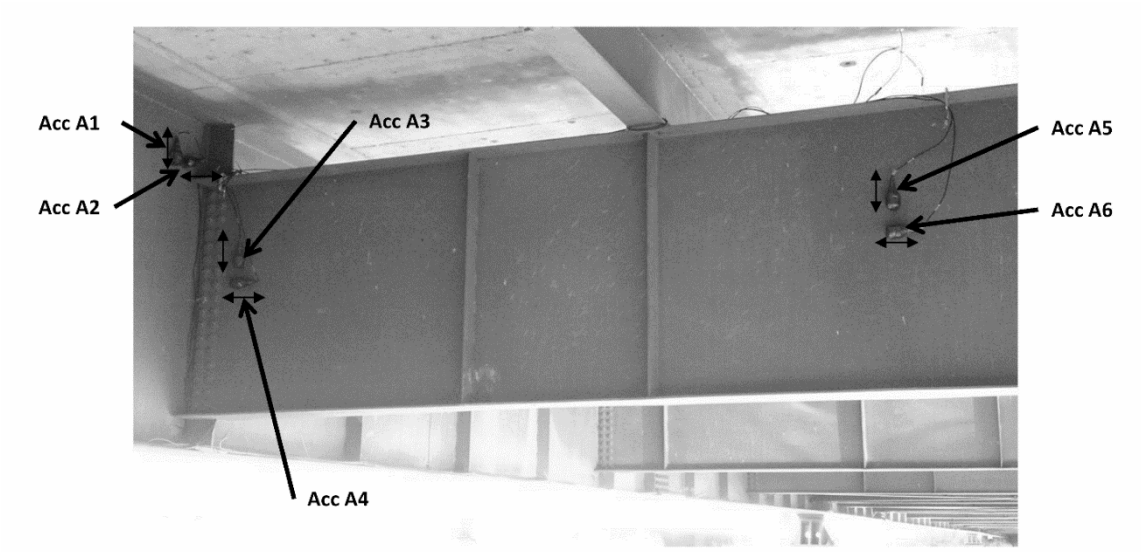

Figure 21 Sensor orientation for Section A. Double-sided arrows depict orientation of sensors

Data collection for Section A was completed by continuously monitoring the operational loading of the bridge for the dates ranging from late November to mid-March. Of these days, the first was chosen as the baseline set (27 November 2012) to which all other days were compared. No damage was expected to occur at this location, so the entire analysis would be considered as a healthy state. The purpose of comparing the days of data within this healthy state was to observe any abnormalities during the period of testing.

3.3.2. Field Results

3.3.2.1. Sacrificial Specimen Operational Load Results

As the decision process dictates, the damage indicator for each day was determined in order to ascertain how different the compared signals were from the baseline. The region of high coherence to be used to improve the accuracy of the damage detection was determined by observing the coherence for the healthy state. Figure 22 shows the coherence between Acc S1 and Acc S2, and the regions of high coherence used for the analysis were decided as the ranges from 15-50 Hz. The coherence for the other pairs of sensors investigated showed very similar values; therefore these plots are not shown. With the selected frequency range, the damage indicator of each comparison set was calculated for all loading scenarios.

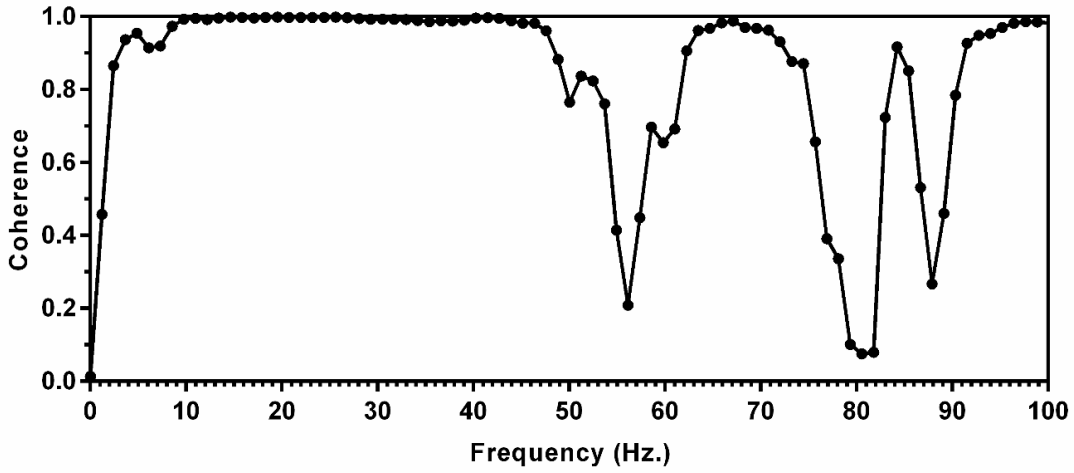

Figure 22 Coherence for pair of sensors S1-S2

The algorithm was first used to determine whether or not damage could be detected by using operational loading of the specimen. This traffic data was gathered in parallel with the impact analyses, thus giving two weeks of healthy data and two weeks of data for each successive damage state, as mentioned previously in Section 3.3. Due to some unforeseen errors in transmission, days in which the majority of the data files were missing, i.e., days that had less than 720 data files, were not included in the analysis, which explains why there are not 14 days for each damage state shown in the results. Figure 23 shows the damage indicators for each day compared to the baseline. As

shown, the healthy days (13-Sep through 25-Sep) were used as the basis; thus all the damage indicators are within the threshold, and all other days clearly detect damage within the sacrificial specimen for the consecutive crack levels (D1 – 30 mm), (D2 – 40 mm), and (D3 – 60 mm), shown respectively in Figure 20(b-c), for the days in the period 13-Sept through 6-Nov. While with damage all damage indicators cross the threshold, there are some variations between the damage indicator at different days, and that may be related to the effect of the changes in the environmental and loading parameters during the testing period, with temperature probably playing a major part [62-64] in masking damage features. The investigation of the effect of temperature will be discussed in Chapter 5.

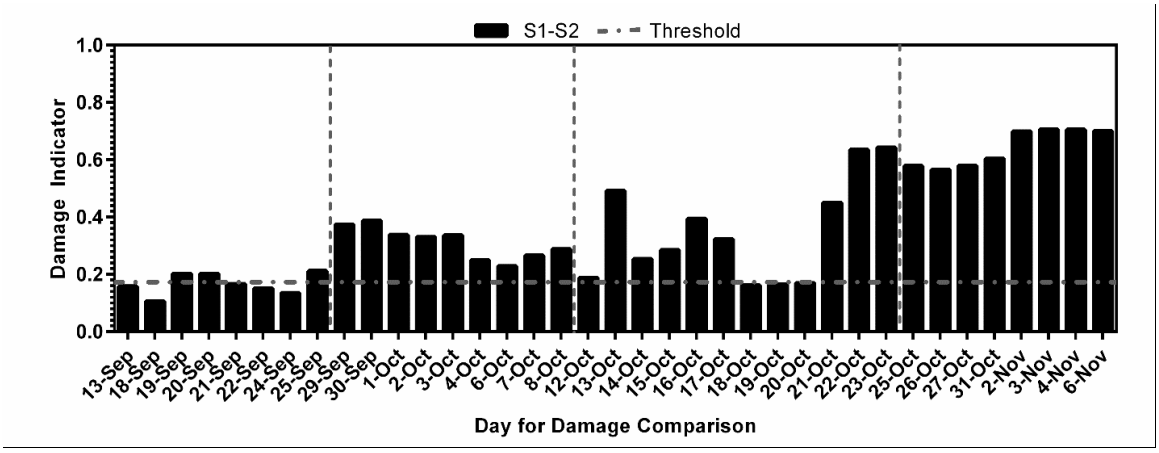

Figure 23 Damage indicator of traffic data for multiple days compared to baseline set for sacrificial specimen: baseline set comprised from 14-Sep (19 °C). Refer to Figure 16 for sensor locations. Vertical dashed lines refer to creation/propagation of damage

3.3.2.2. Sacrificial Specimen Impact Load Results

In this test, the specimen was tested under a more controlled loading condition, with the strut being taken away from the specimen. The goal of the impact test was to rule out any effects and uncertainties that could have occurred as a result of removing and reinstalling the strut during the operational loading tests of the specimen. Also, this test will present more insight about the validity of the operational loading of the specimen. Figure 24 shows the results of the impact testing as compared to the 50 impacts taken for the healthy state (D0). The notation used in this figure is as follows: D1 represents the first

damage level (Figure 20(a)), D2 represents the second damage level (Figure 20(b)), D3 represents the third damage level (Figure 20(c)), "a" represents the 50 impacts directly after the damage for that damage state, and "b" represents the 50 impacts directly before the next damage state (two weeks after "D#a"). The expectation from these results was that the damage indicator would monotonically increase with damage (i.e., D1b should be smaller than D2a, and D2b should be smaller than D3). As expected, damage is clearly detected (all damage states are above the threshold set by the healthy state). It is also noted that the damage indicator increased during the same damage state (i.e., increased between D1a and D1b).

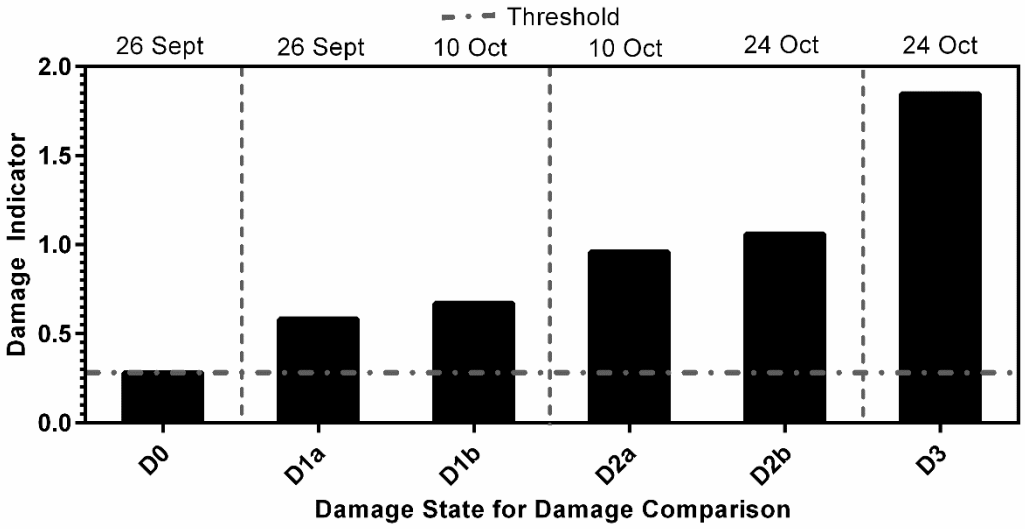

Figure 24 Damage indicators of manual impacts for multiple damage states compared to baseline damage state for sacrificial specimen. Vertical dashed lines refer to creation/propagation of damage

3.3.2.3. Section A Operational Load Results

Following the same procedure as that used for the sacrificial specimen, the acceleration data from the traffic vibrations were used to determine the transmissibility between the pair of sensors A5-A1 (Figure 21). The coherence for sensors A5-A1 is shown in Figure 25. It can be seen that the coherence between signals on the actual bridge was not expected to be as high as with the sacrificial specimen; however, the same frequency

ranges used in the testing of the sacrificial specimen were the highest found for Section A and were used for the analysis of Section A.

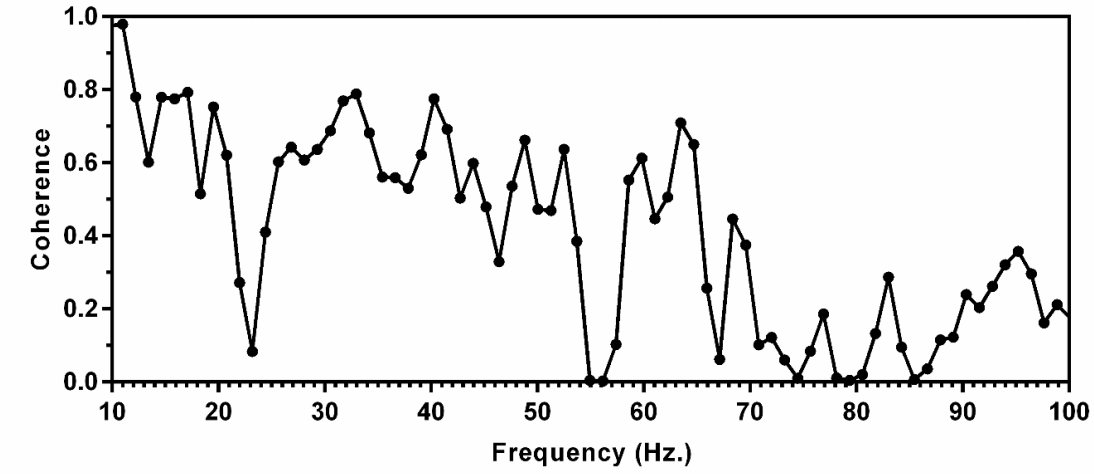

Figure 25 Coherence for pair of sensors A5-A1

Each day of data (set of 1440 data files) was used for comparison, and the damage indicator was calculated based on these evaluations. The damage indicators, as compared to the baseline set (27 November 2012), are shown in Figure 26(a). The threshold was constructed for a basis containing the first two weeks of data. The results did not show any damage indicator crossing the threshold, except for two days (10-Mar and 11-Mar). As per the algorithm, this day would not send a warning alarm (as the prior seven days did not exceed the threshold), nor would a watch alarm be given (as the prior three days did not exceed the threshold). From these observations, it can be concluded that damage is not detected on Section A for the entirety of the field work completed, which is consistent with the physical health condition of that portion of the bridge.

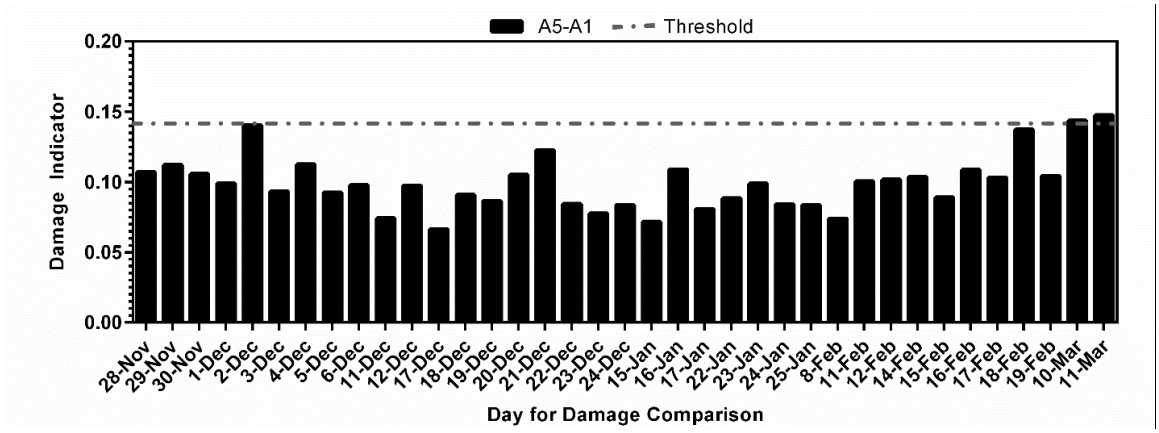

Figure 26 Damage indicators of traffic data for multiple days compared to baseline set for sensors at Section A: baseline set comprised from 27-Nov (3 °C). Refer to Figure 21 for sensor locations

3.4. Overall Results and Discussion for Coherence-based Algorithm

This work presented a methodology to monitor the health condition of highway steel-girder bridges. The methodology combines the transmissibility function, coherence function, and probabilistic schemes and calculates a damage indicator that gives critical information about the health condition of the bridge. This damage indicator has been shown, through this work, to be a useful tool for damage detection. The coherence function is calculated to objectively determine regions of transmissibility that could be trusted for repeatability, in that the signals within the selected regions maintain a near-linear relationship. The probabilistic schemes used within the field testing portion of this algorithm allow for the threshold to be determined equitably by placing an upper limit on a large set of healthy data, thus encompassing many of the uncertainties that can arise.

Based on the numerical and experimental analyses, it is concluded that the presented coherence-based damage-detection algorithm can accurately detect, comparatively locate, and relatively quantify damage for complex structures and damage severities. Damage is correctly not detected when comparing with additional impacts from the baseline state, and damage is clearly detected for any damage state by observing the significant increase in the magnitude of the damage indicator. A relative quantification can be perceived, in that the greater the magnitude of the damage indicator, the greater the change in the dynamic characteristics from the baseline set. Damage can also be comparatively located

by assessing the difference in magnitudes of the damage indicator between symmetric pairs of sensors. A greater magnitude is caused by more significant changes in the dynamic characteristics of the structure.

It should be noted that a limitation of the laboratory experiments was that the specimen was not able to reproduce crack re-initiation through a stop-hole. In general, the presented algorithm proved successful in detecting fatigue crack initiation and propagation before retrofitting, as well as crack branching after retrofitting. Another important feature of this algorithm is the ability to set the baseline as any state, healthy or damaged, and still maintain accurate damage detection. That gives the proposed method the potential to be used as a prognostic tool for monitoring structures with different initial damage conditions.

Field results using stochastic operational traffic loading during the period of mid-September 2012 to mid-March 2013 have indicated the capability of the proposed methodology in evaluating the changes in the health condition of a section of the bridge, and in consistently detecting cracks of various sizes on a sacrificial specimen integrated with the bridge abutment and a floor beam.

In states with extreme fluctuation in environmental and loading conditions, large variation in the response data is expected, including when monitoring healthy data, which may generate different forms of uncertainty in the decision-making process on bridge maintenance. Therefore, the implementation of an objective threshold that generates watch and warning alarms becomes a very important measure in reducing the uncertainties in detecting damage. Some concerns may arise about the waiting time period of the watch (three consecutive daily violations) and warning (seven consecutive daily violations) alarms before a decision can be made. Albeit the choice of three and seven days for the watch and warning alarms, respectively, remains partly subjective, the decisions were based on observations made on both the specimen and Section A testing. The selection of three consecutive daily violations for the watch alarm was based on the results of Section A, where the damage indicator approached the threshold several times but not three times consecutively. Also, based on the results of the sacrificial specimen, when damage had occurred, the damage indicator consistently breached the threshold.

While this is a real concern, redundancy in the bridge design allows for operative structural integrity, even after damage can be detected, albeit for a short duration. Also, three to seven consecutive days of violations are not unreasonable durations considering the traditional bi-annual bridge inspection.

Also, it may be recommended to extend the number of days required for the basis to one year of healthy data in lieu of two weeks of data. The results of this work showed that, even when limited to two weeks of data (20000+ one-minute files), the threshold was able to encompass most of the uncertainties that occurred in the period of 27-Nov through 11-Dec, with the variation in temperature ranging from -3 ℃ to 15 ℃, and that extending the amount of data used in the basis may benefit the algorithm.

The results of the field impact test have shown a noticeable increase in the damage indicator of the crack on the sacrificial specimen when the specimen remained under the operational traffic load and was tested after two weeks (D1a to D1b and D2a to D2b). The justification for this increase is that the crack may have propagated under operational loading during the two weeks of remote monitoring of the specimen. This may imply that the algorithm is sensitive enough to detect crack growth from accelerated crack testing as well as gradual growth from operational loading; however, the variation in temperature and other environmental parameters during the testing days may play a role in this change as well.

It should be noted that during the investigation of the field specimen and bridge, construction of a trail occurred directly underneath the bridge, with vibrations and noises significant enough to warrant discussion. Although the exact start date of construction is unknown, it is reasonably estimated that construction equipment was being used from around 23 October through the middle of November. This construction equipment added noise and ambient vibrations to the entire system (bridge, sacrificial specimen, and surrounding area) that may have affected the magnitude of the percent-violation. The results of testing the sacrificial specimen under operational loading during this period have shown that the construction effects were outweighed by the effect of damage on the sacrificial specimen, a result that was reinforced by the findings of the impact testing on the specimen.

Overall, the presented damage-detection algorithm has shown success in detecting small abnormalities in all facets of analysis, i.e. numerically, experimentally and in the field under both controlled loading and operational loading scenarios. Also, the use of an objective threshold for the field analyses in combination with the detection decision process allocates alarm severities, i.e., watch and warning alarms, thus allowing for variations in environmental and loading characteristics without causing false warnings. The significance of the threshold is observed through the analysis of Section A in which damage was correctly not identified, even though environmental and loading conditions were fluctuating. It should be noted that the false damage-detection testing on Section A was limited to false positive detection (damage detected when no damage on bridge) and that false negative detection (damage not detected when damage on bridge) could not be investigated.

Chapter 4. Effect of Force Location, Boundary Condition, and Sensor Location/Orientation

Previous studies have indicated that the variability in the dynamic response of structures can be attributed to environmental and operational parameters, among other uncertainties [36, 37]. Sohn [36] classifies a few of these effects as variations due to temperature, boundary conditions, mass loading, and wind, and details methods and procedures to accommodate for these inconsistencies. The article by Kim et al. [64] focused on the mass loading variations and showed that the natural frequency of a bridge had decreased by 5.4% due to heavy traffic. Work done by Cawley [74] investigated the effect of boundary conditions and change in geometry on a cantilever beam and found that the natural frequency with a 2% crack was 40 times smaller than that of a 2% increase in length. Quek et al. [75] also investigated boundary conditions and crack orientation as sources of variation and were able to use wavelet algorithms to accurately detect cracks in numerical models for multiple layouts including edge cracks and embedded cracks. Due to the importance of dynamic responses in vibration-based damage detection algorithms, the variation of boundary conditions and loading, among other parameters, also affect the detection methodologies. Both Farrar et al. [66] and Peeters et al. [65] conducted sensitivity studies on bridges in which the method for input excitation varied. Farrar et al. [66] tested impact and ambient excitations on the Alamosa Canyon Bridge and found that the mode shapes for each were near identical but that variations occurred when calculating the dampening effects. Peeters et al. [65] used the testing on the Z24 Bridge to examine shaker, impact, and ambient input excitation and found that the natural frequencies calculated from each of these loadings were comparable.

Work has also been conducted to investigate the effect of force location and magnitude on transmissibility and furthermore transmissibility-based damage detection methodologies. The book chapter by Maia et al. [28] discusses the derivation and properties transmissibility, including the characteristic in which the transmissibility can be independent from the applied force. In this article, another attribute is described in that the transmissibility will remain unaffected by changes to the mass or stiffness at locations where the force is applied. The review by Chesne and Deraemaeker [19],

however, utilizes numerical simulations to discuss how the force location affects the damage detection methodology and found that damage localization was only possible when the force was near the damage location in non-dispersive systems, and that no localization could be attained for dispersive systems. It is an aim of this work to investigate the effect of force location and magnitude, if any exists, on transmissibility and contribute to the contradictory knowledge in existence.

The goal of this chapter is to conduct a parametric study about the effect that force location, boundary conditions, and sensor location/orientation has on the damage indicator and presented transmissibility-based methodology. This effect was studied numerically by varying the force location on a specimen both with and without damage. With this data, the localization of the damage by means of the damage indicator was observed for multiple damage locations, which gives indications on how force location affects transmissibility. Section 4.2 details the background information for the effects of force and sensor location on the dynamic response of structures, as well as providing a numerical analysis on a non-dispersive model. Section 4.3 details the setup, testing, and results of a numerical cantilever beam, and Section 4.4 details the setup, testing, and results of a numerical pin-pin beam. A parametric investigation of force location and sensor location on a numerical representation of the sacrificial specimen is provided in Section 4.5. A similar parametric study on sensor location and sensor orientation on a numerical model of a girder-floor beam system is given in Section 4.6. A sensitivity study of sensor orientation for the field testing previously discussed in Chapter 3 is provided in Section 4.7, and Section 4.8 presents the overall conclusions found by the author.

4.1. Parametric Testing on Non-dispersive System

To examine the effect of force location and sensor location on damage detection algorithms, a simple five degree-of-freedom spring-mass system was modeled as shown in Figure 27. For the purposes of simplicity, all of the masses were 0.5 kg, and all of the springs had a stiffness of 3 N/m.

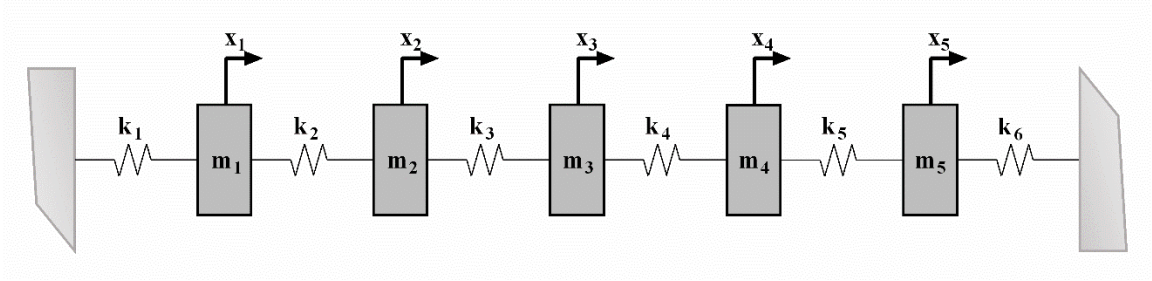

Figure 27 Spring-mass system used for parametric test of force location on common damage detection identifiers

The general equation of motion for a multiple degree-of-freedom (mdof) undamped system like the one depicted is shown in Equation (4.1), where $\mathbf{M}$ is the mass matrix, $\mathbf{K}$ is the stiffness matrix, $\boldsymbol{x}(t)$ and $\ddot{\boldsymbol{x}}(t)$ are the displacement and acceleration vectors, respectively, and $\boldsymbol{f}(t)$ is the applied force vector.

$$\mathbf{M}\ddot{\boldsymbol{x}}(t)+\mathbf{K}\boldsymbol{x}(t)=\boldsymbol{f}(t) \tag{4.1}$$

In order to solve this differential equation, the Laplace transform is used to simplify the expression (Equation (4.2), where $\mathbf{Z}$ is the dynamic stiffness matrix). It is noted that this transform is completed with zero initial conditions.

$$\left[\mathbf{M}s^2+\mathbf{K}\right]\boldsymbol{X}(s)=\mathbf{Z}(s)\boldsymbol{X}(s)=\boldsymbol{F}(s) \tag{4.2}$$

By substituting $s=i\omega$ into Equation (4.2), and rearranging to solve for the displacements, $\mathbf{X}$, the common expression for the transfer function between displacement and force is derived (Equation (4.3), where $\mathbf{H}$ is the frequency response function (FRF) and is equal to the inverse of the dynamic stiffness matrix.

$$X_j(\omega)=\mathrm{H}_{jk}(\omega)F_k(\omega)=\left[\mathbf{K}-\mathbf{M}\omega^2\right]^{-1}_{jk}F_k(\omega)=\frac{\mathbf{adj}\left[\mathbf{K}-\mathbf{M}\omega^2\right]_{jk}}{\det\left[\mathbf{K}-\mathbf{M}\omega^2\right]}F_k(\omega) \tag{4.3}$$

It is known that natural frequencies are not affected by force location because natural frequencies are structural parameters independent of force, therefore damage detection algorithms whose indicator is based on resonance frequencies will be unaffected by this aspect of the parametric study. The impact that sensor location has on said algorithms are

also expected to be negligible due to resonance being a global system property. On the other hand, the natural frequencies of a system are directly related to the frequency response function as shown in Equation (4.3), from the characteristic equation $\det\left[\mathbf{K}-\mathbf{M}\omega^2\right]$. It can be determined that poles of the frequency response function correspond to the natural frequencies of the system. Another important observation is that the frequency response function does depend on force location, as well as sensor location. To investigate the effect that these parameters have on the FRF, $\mathbf{H}$ was calculated for the system described in Figure 27. The analysis also studied the effect of damage by reducing the stiffness of spring 1 by 10%. The parametric plots of frequency versus FRF for varying the location of the applied force are shown in Figure 28 and Figure 29. It is noted that H_{ij} is the frequency response function for the displacement at mass *i* and force at location *j*.

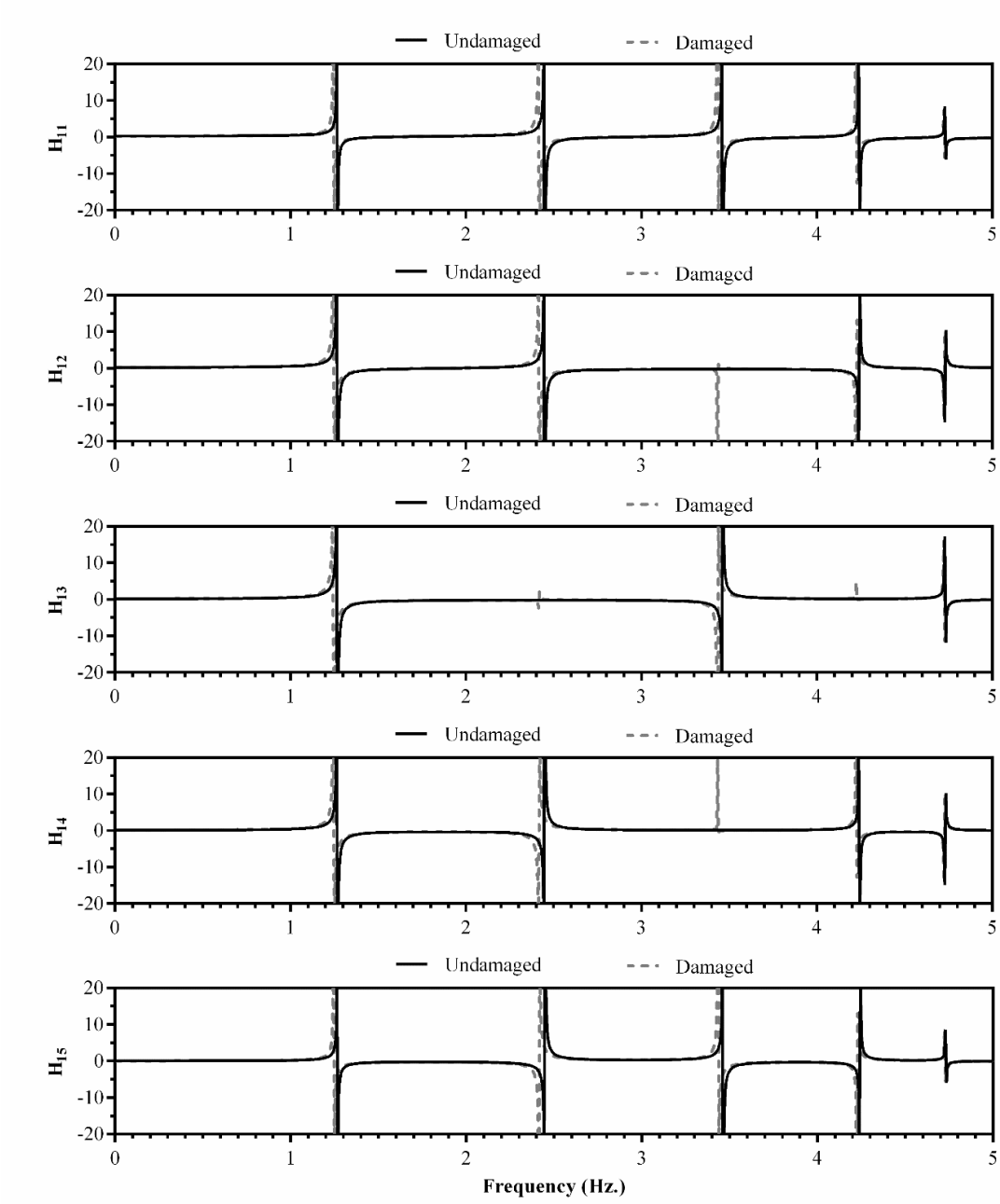

Figure 28 Plots for components of frequency response function of mass 1 showing effects from change in force location as well as change in damage state

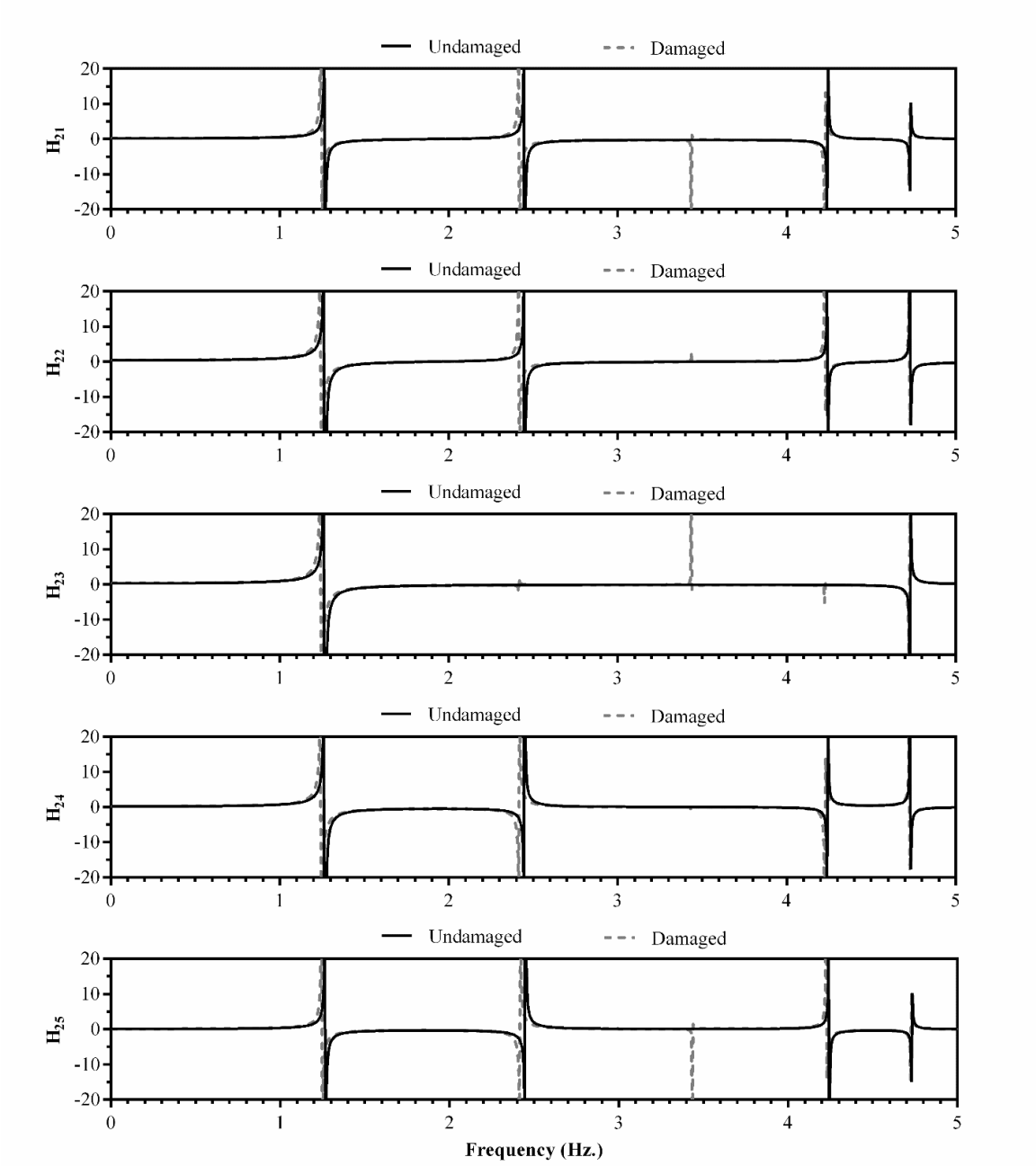

Figure 29 Plots for components of frequency response function of mass 2 showing effects from change in force location as well as change in damage state

By looking at the first poles of the frequency response function (Table 1), it can be concluded that the change in force location as well as sensor location has no effect on **H** ,

while damage has reduced the frequency of the pole by 1.48%. This proves to be equally as beneficial as calculating the natural frequencies of the system for damage detection due to the independence from force and sensor locations; however, this conclusion is only true for certain situations. It is noted that not all of the resonant frequencies can be observed as poles for each component of the frequency response function (see H_{13}, around 2.50 Hz. and around 4.25 Hz. in Figure 28). By taking the displacement at mass 1 with the force also at mass 1, the resulting component of **H** is known as a point-FRF, and will have poles at each of the natural frequencies of the system. By changing either the location of the response displacement or the force location, certain frequencies are not excited, therefore natural frequencies are not shown. It can be concluded that while the force location has no effect on the FRF pole frequencies, the force location and sensor location do affect whether or not a pole exists for a given component of the FRF. In either case, however, damage was clearly identified, thus justifying the possible use of FRF for damage detection.

Table 1 Frequency of first pole for components of frequency response function and percent difference showing effect of change in force location and damage

	Undamaged 1^{st} Pole Location	Percent Difference from H_{11}	Damaged ($0.9*k_1$) 1^{st} Pole Location	Percent Difference from Undamaged
H_{11}, H_{21}	1.2670 Hz	0.00%	1.2483 Hz	1.48%
H_{12}, H_{22}	1.2670 Hz	0.00%	1.2483 Hz	1.48%
H_{13}, H_{23}	1.2670 Hz	0.00%	1.2483 Hz	1.48%
H_{14}, H_{24}	1.2670 Hz	0.00%	1.2483 Hz	1.48%
H_{15}, H_{25}	1.2670 Hz	0.00%	1.2483 Hz	1.48%

The other common methodology that was investigated for damage detection is the use of transmissibility. Transmissibility can be easily calculated as an extension of Equation (4.3) by taking the ratio of any two displacement responses, as shown in Equation (4.4).

$$T_{ij}^{k}(\omega)=\frac{X_i(\omega)}{X_j(\omega)}=\frac{\mathrm{H}_{ik}(\omega)F_k(\omega)}{\mathrm{H}_{jk}(\omega)F_k(\omega)}=\frac{\mathbf{adj}\left[\mathbf{K}-\mathbf{M}\omega^2\right]_{ik}}{\mathbf{adj}\left[\mathbf{K}-\mathbf{M}\omega^2\right]_{jk}} \tag{4.4}$$

Although it may not be seen directly in the final form of this equation, force location does have influence on transmissibility through the response of each displacement. The effect of this influence was studied by calculating the transmissibility between mass 1 and 2 and varying the force over all five locations. The same damage as the FRF analysis was also applied here to investigate the effect of force location on damage detection. The plots of frequency versus transmissibility for varying force location are shown in Figure 30.

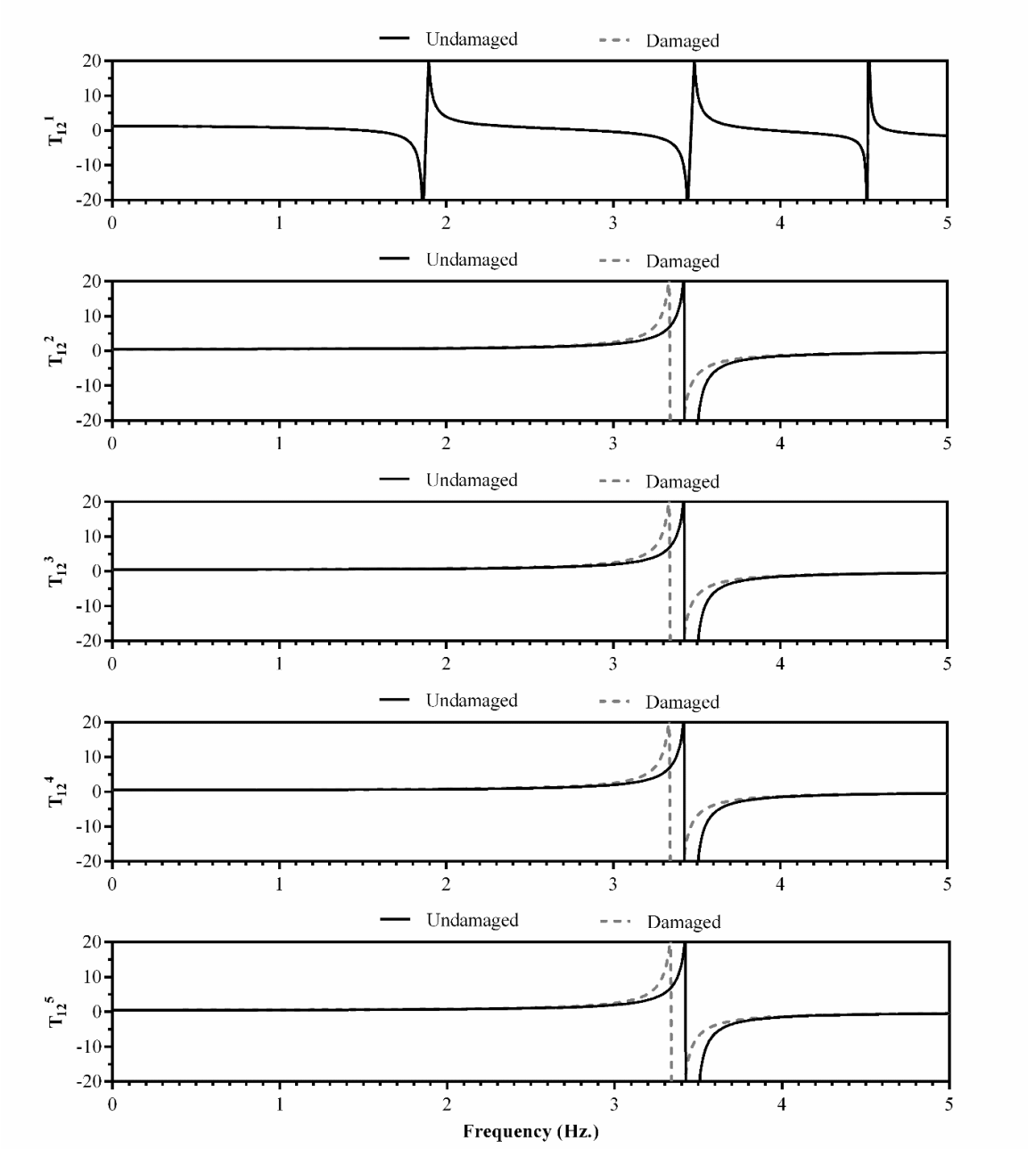

Figure 30 Plots for transmissibility between masses 1 and 2 showing effects from change in force location as well as change in damage state

As shown in Figure 30, the poles of transmissibility do not align with natural frequencies, unlike that of the frequency response function. It is also shown that damage does not affect the transmissibility when the force is applied at mass 1 (0.00% difference in pole location), but significantly affects the transmissibility when the force is applied elsewhere

(2.60% difference in pole location). Force location only affects transmissibility when the force is applied at the same location of the output displacement (*i* location), while the transmissibility remains identical for the other force locations. To expand on the parametric study to investigate the effect of sensor location, the transmissibility between two additional pairs of masses (between masses 1 and 3 and between masses 2 and 3) were calculated for varying force locations. The results are shown in Figure 31 and Figure 32. It can be seen from these figures that similar trends arise in that the transmissibility is affected when the force is applied near the output displacement, and that damage is identifiable when the force is applied away from the damage location. Sensor location does affect the location of anti-resonances in the transmissibility and should be accounted for when cross-referencing between different pairs of sensors.

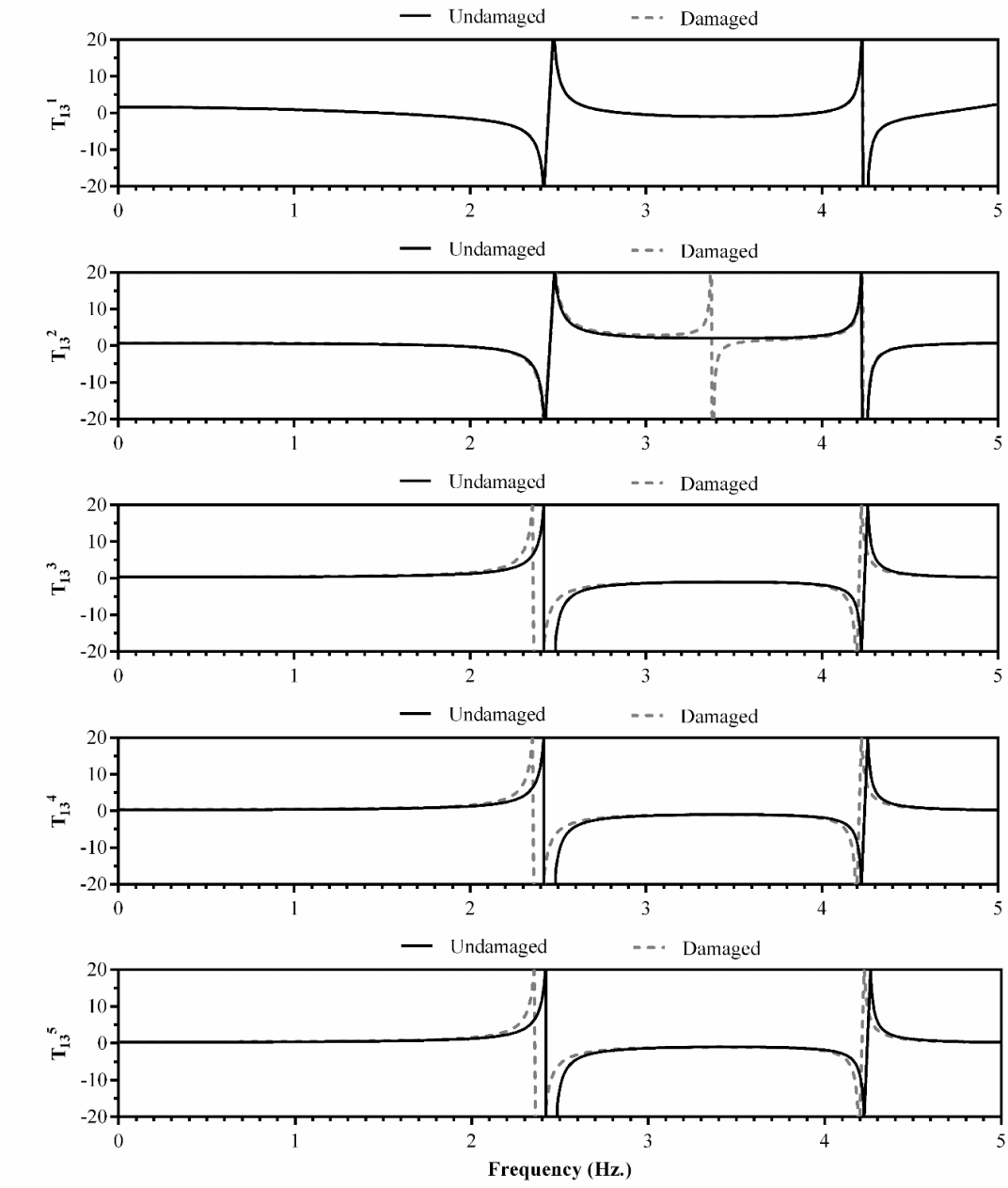

Figure 31 Plots for transmissibility between masses 1 and 3 showing effects from change in force location as well as change in damage state

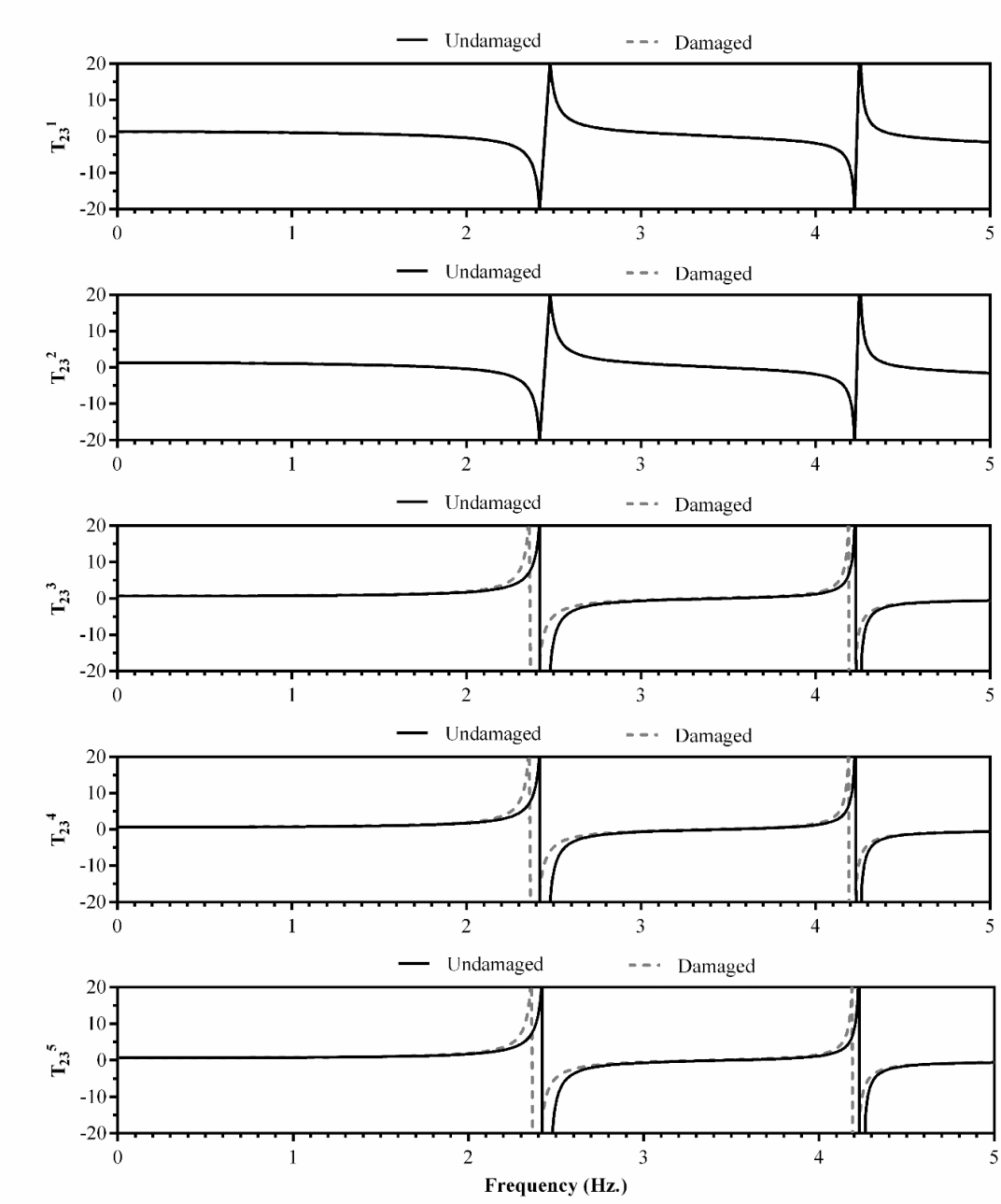

Figure 32 Plots for transmissibility between masses 2 and 3 showing effects from change in force location as well as change in damage state

It can be concluded that when detecting damage, damage-sensitive features only arise when the force is applied away from the damage location as well as away from the *i*th

displacement location. Since the force location does not affect the majority of the scenarios for the transmissibility calculation, and the damage sensitivity is greater for transmissibility than for FRF, transmissibility will be used for further investigation on dispersive models (using finite element models).

4.2. Numerical Parametric Testing on Cantilever

The first specimen used to conduct the parametric study on the damage indicator with varying force locations was a simple cantilever. A numerical model was created in ABAQUS (ABAQUS 6.12, Dassault Systemes Simulia Corp.), and the responses were manipulated in MATLAB (MATLAB R2013a, The MathWorks Inc.) in order to calculate the damage indicator. The damage indicator used in these analyses is the same as outlined in the previous chapters. The following section details the setup used, results found, and discussion for the parametric testing on the cantilever beam.

4.2.1. Parametric Cantilever Setup and Testing Procedure

The cantilever used for this analysis, measuring 609.6 mm long by 6.35 mm tall by 25.4 mm deep, consisted of 24 quadratic beam elements, as shown in Figure 33. Seven equally spaced nodes were chosen to measure the response due to impulse loading. The impulse loading was applied parametrically at each of these seven nodes such that only one force was applied per loading scenario. Damage was introduced into the model by reducing the stiffness of one (or two) elements, shown as the damage locations in Figure 33. Three damage severities (5%, 10%, and 20% reduction in stiffness) were created in order to also monitor the effect of damage magnitude on the parametric study.

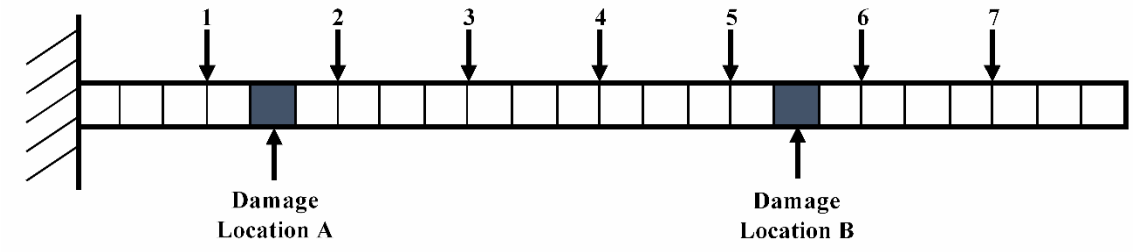

Figure 33 Layout for cantilever testing depicting node locations for forces and responses, boundary conditions, and damage locations

4.2.2. Parametric Cantilever Results

As per the damage detection algorithm, the time-history responses were used to calculate the transmissibility between pairs of nodes. For this parametric study, six pairs of nodes were investigated: pairs 1-2, 2-3, 3-4, 4-5, 5-6, and 6-7. The damage indicator was calculated by setting the transmissibility between one pair of nodes on the undamaged model as the baseline set and setting the transmissibility between the same pair of nodes on each of the damage severities as a comparison set. This calculation was repeated for each pair of nodes under the same loading scenario, and thus the entire process was repeated for each loading scenario, i.e. each change in force location. By choosing adjacent pairs of nodes, the damage could investigate sensor location as well as damage detection by observing the magnitude of the damage indicator and comparing with the other pairs of nodes. Figure 34, Figure 35, and Figure 36 show the plots for damage indicator for the cantilever with varying damage severities at damage location A, damage location B, and both damage locations A and B, respectively.

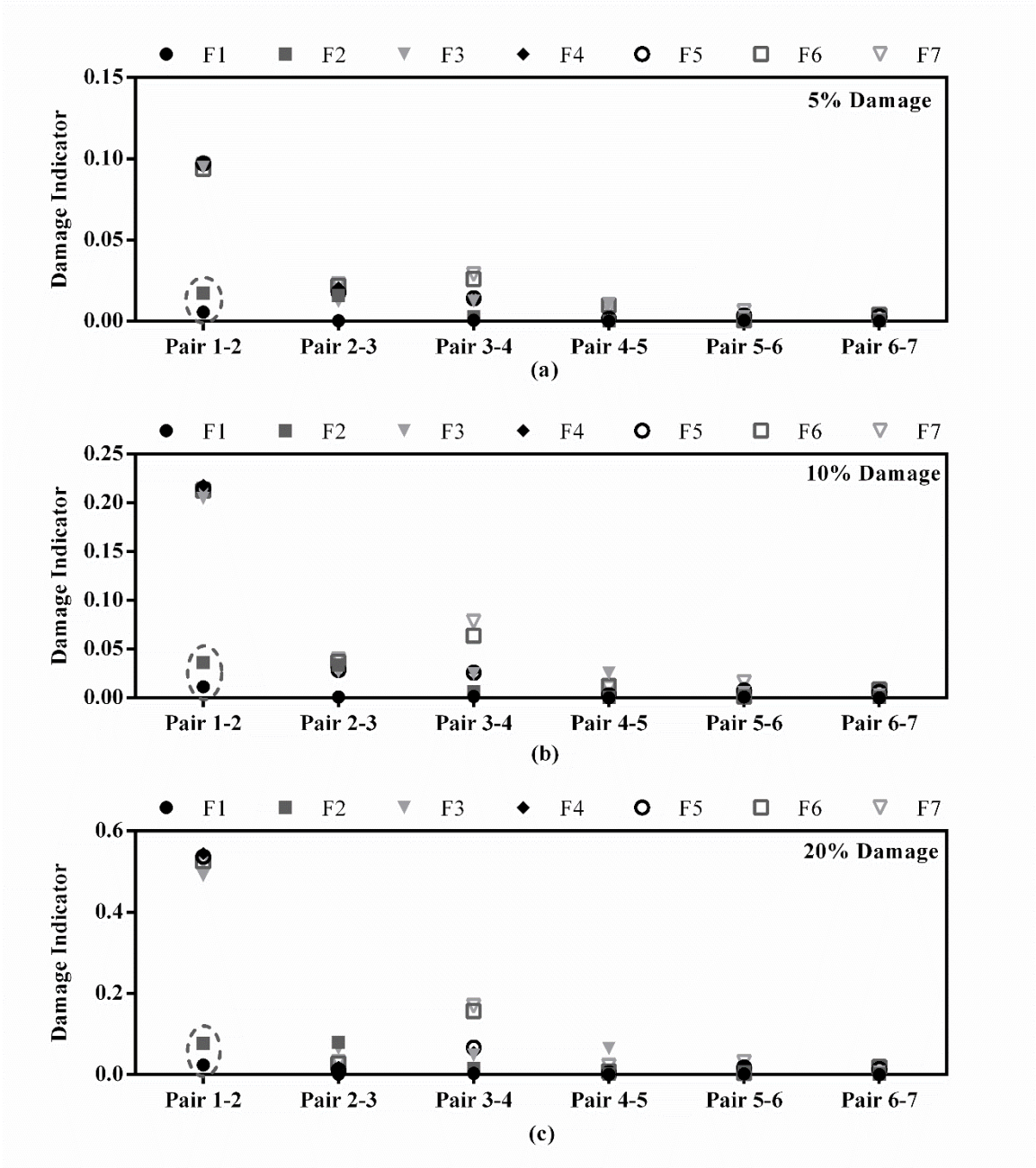

Figure 34 Damage indicator calculated from transmissibility from adjacent pairs of nodes on cantilever for forces applied at each node: (a) 5 percent reduction in stiffness at damage location A, (b) 10 percent reduction in stiffness at damage location A, (c) 20 percent reduction in stiffness at damage location A

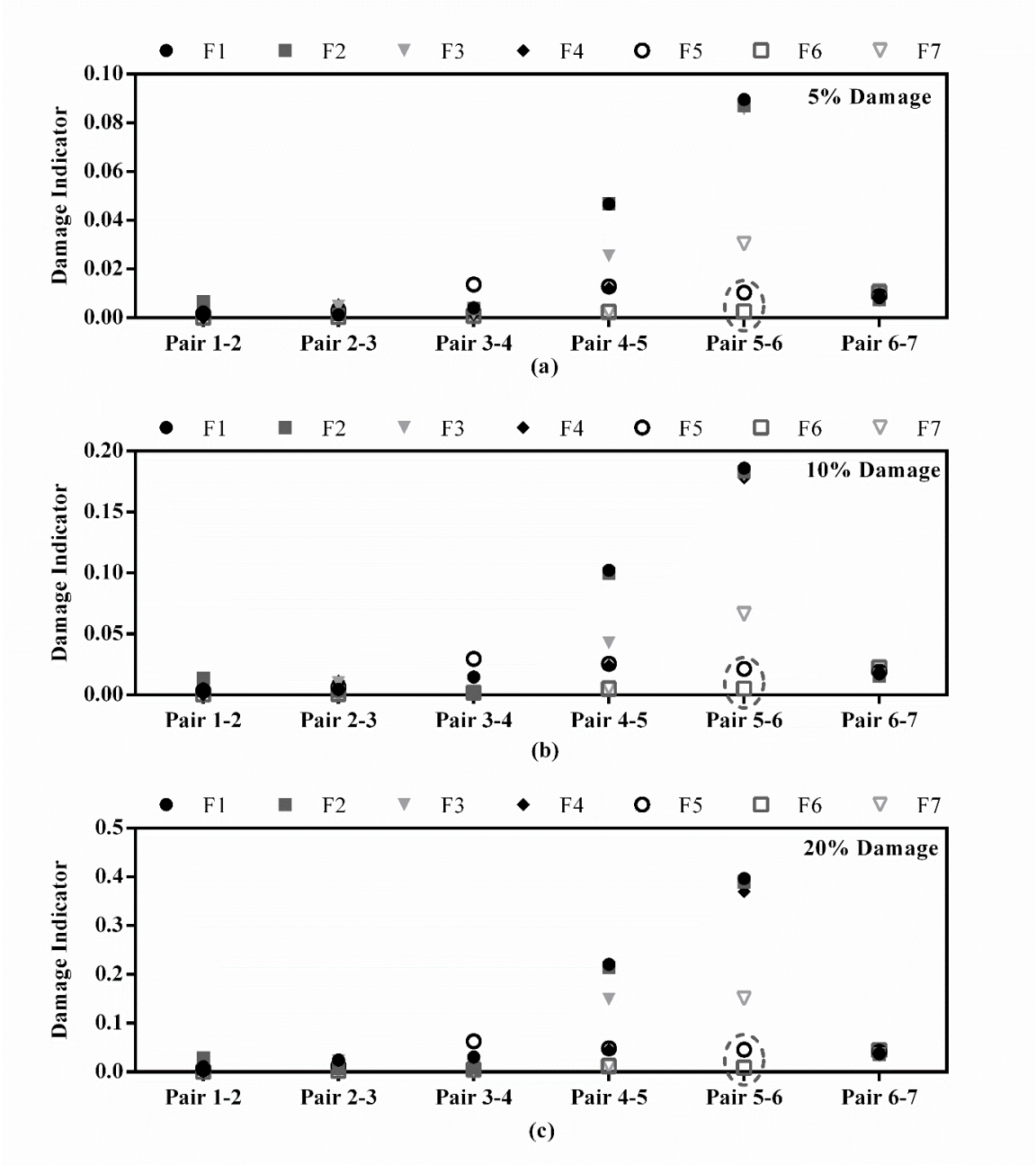

Figure 35 Damage indicator calculated from transmissibility from adjacent pairs of nodes on cantilever for forces applied at each node: (a) 5 percent reduction in stiffness at damage location B, (b) 10 percent reduction in stiffness at damage location B, (c) 20 percent reduction in stiffness at damage location B

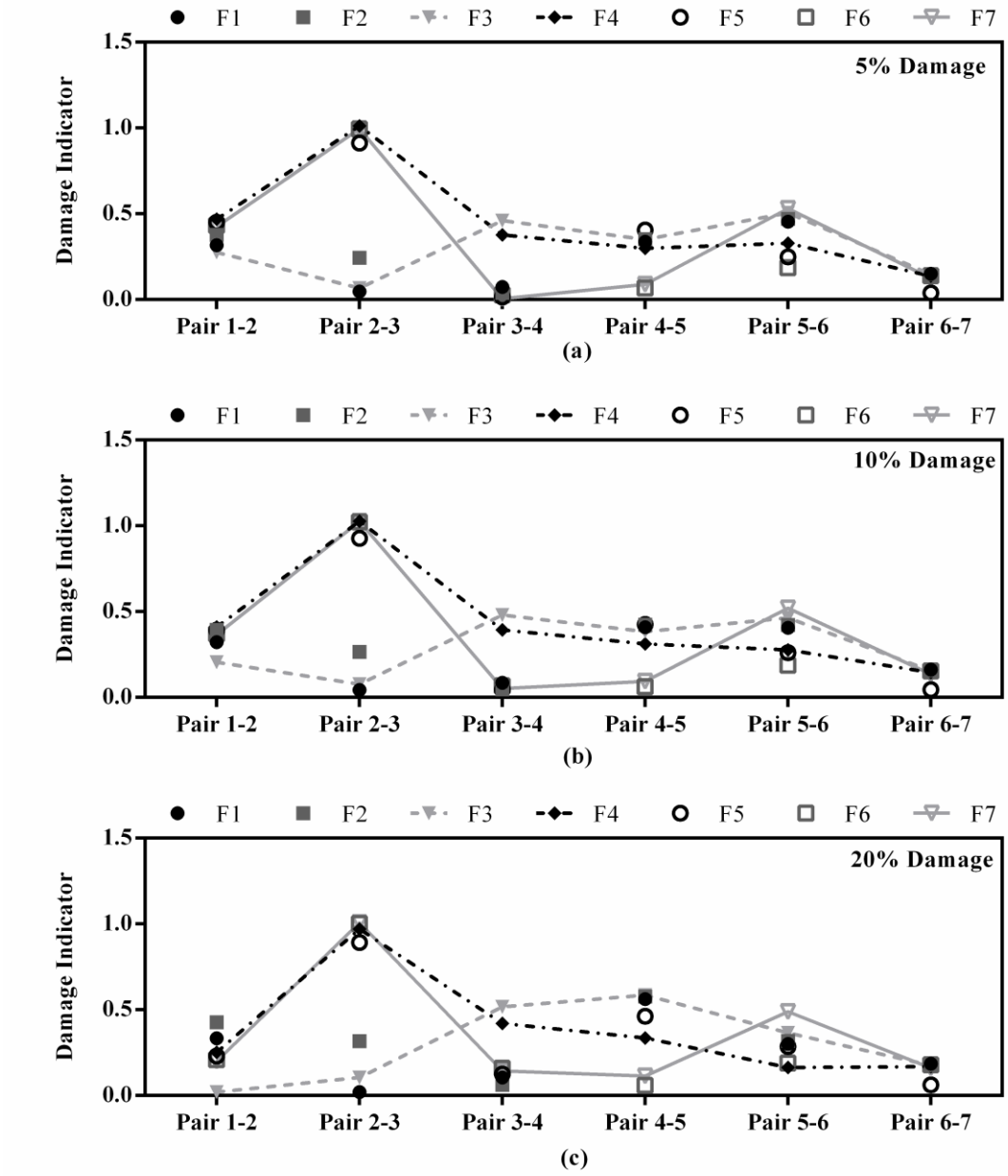

Figure 36 Damage indicator calculated from transmissibility from adjacent pairs of nodes on cantilever for forces applied at each node. NOTE: Data groups with connecting lines emphasize the data groups in which the force is not applied to either damage location: (a) 5 percent reduction in stiffness at damage locations A and B, (b) 10 percent reduction in stiffness at damage locations A and B, (c) 20 percent reduction in stiffness at damage locations A and B

4.2.3. Parametric Cantilever Discussion

It can be seen from Figure 34 that the magnitude of the damage indicator is greatest for pair 1-2, with the exception of when the force is at locations 1 or 2 (emphasized by the gray dashed circle). This observation correctly locates the damage at damage location A. This observation also infers that by applying the force near the damage location, the signal becomes less sensitive to damage. One possibility for this could be that the force is introducing a localized randomness into the response of the system, whereas away from the applied force is a more steady-state response. The purpose of an impulse loading is to excite a large range of frequencies in the structure. Due to damping within the structure, many frequencies fade out, and simultaneously resonance frequencies are amplified; therefore it is easier and more accurate to observe a structure's natural frequencies at a steady-state. Applying this justification, the force being applied to nodes 1 or 2 likely excite more frequencies that are not damage sensitive, thus making it difficult to distinguish changes in the response of the structure.

Figure 35 shows this same trend, however for the damage at damage location B. Damage can be correctly located on the cantilever, as shown by the greatest damage indicator magnitudes are with pair 5-6, with the exception of when the force is at locations 5 and 6 (emphasized by the gray dashed circle). The same justification follows for this scenario as from the damage at damage location A.

The plots shown in Figure 36 are the results from identical damage applied simultaneously at damage locations A and B. It is noted that to highlight the data sets in which the impulse is not applied to either damage location, e.g. the force is applied away from the damage, connecting lines between data points were utilized. It can be seen that for all damage severities, the loading scenario with the force applied at node seven most accurately depicts the correct damage arrangement, although damage is falsely detected between nodes 2-3 instead of between nodes 1-2. Furthermore, it is observed (by the solid line connecting data points) that the damage indicator increases only around the two damage locations, whereas the other two scenarios (F3 with the dashed line and F4 with the dash-dot line) do not decrease between the damage locations. This can be justified by

the force being applied to these locations, thus resulting in skewed results around these locations.

4.3. Numerical Parametric Testing on Pin-Pin Beam

A second specimen was used in the parametric study to investigate if boundary conditions affect the results shown previously. A pin-pin beam model was created in ABAQUS and the responses were used to calculate the damage indicator, much like the cantilever. The following section details the setup used, results found, and discussion for the parametric testing on the pin-pin beam.

4.3.1. Parametric Pin-Pin Beam Setup and Testing Procedure

The beam used for this analysis was the same dimensions and layout as the cantilever (609.6 mm long by 6.35 mm tall by 25.4 mm deep), with the only difference between the pin-pin beam and the cantilever were the boundary conditions, as shown in Figure 37. The same seven equally spaced nodes were chosen to measure the response due to the same parametric impulse loading scenarios. Damage was introduced into the model by reducing the stiffness of one (or two) elements, shown as the damage locations in Figure 54. Three damage severities (5%, 10%, and 20% reduction in stiffness) were created in order to also monitor the effect of damage magnitude on the parametric study.

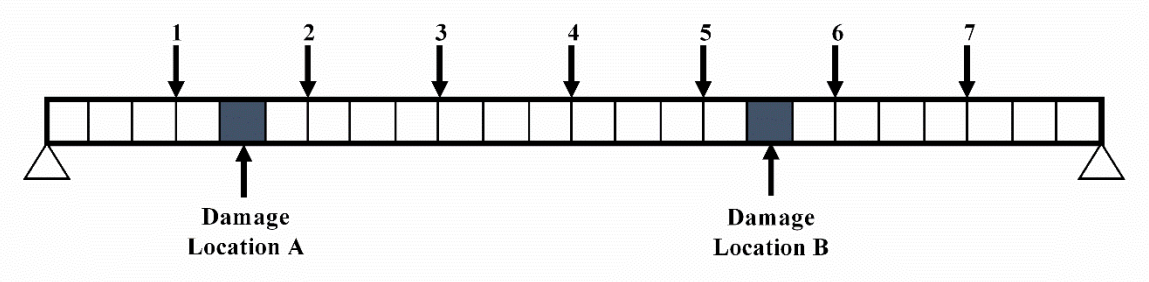

Figure 37 Layout for beam testing depicting node locations for forces and responses, boundary conditions, and damage locations

4.3.2. Parametric Pin-Pin Beam Results

Following the same process as the cantilever, the time-history responses were used to calculate the transmissibility and damage indicator between adjacent pairs of nodes. Figure 38 and Figure 39 show the plots for damage indicator for the pin-pin beam with

varying damage severities at damage location A and both damage locations A and B, respectively.

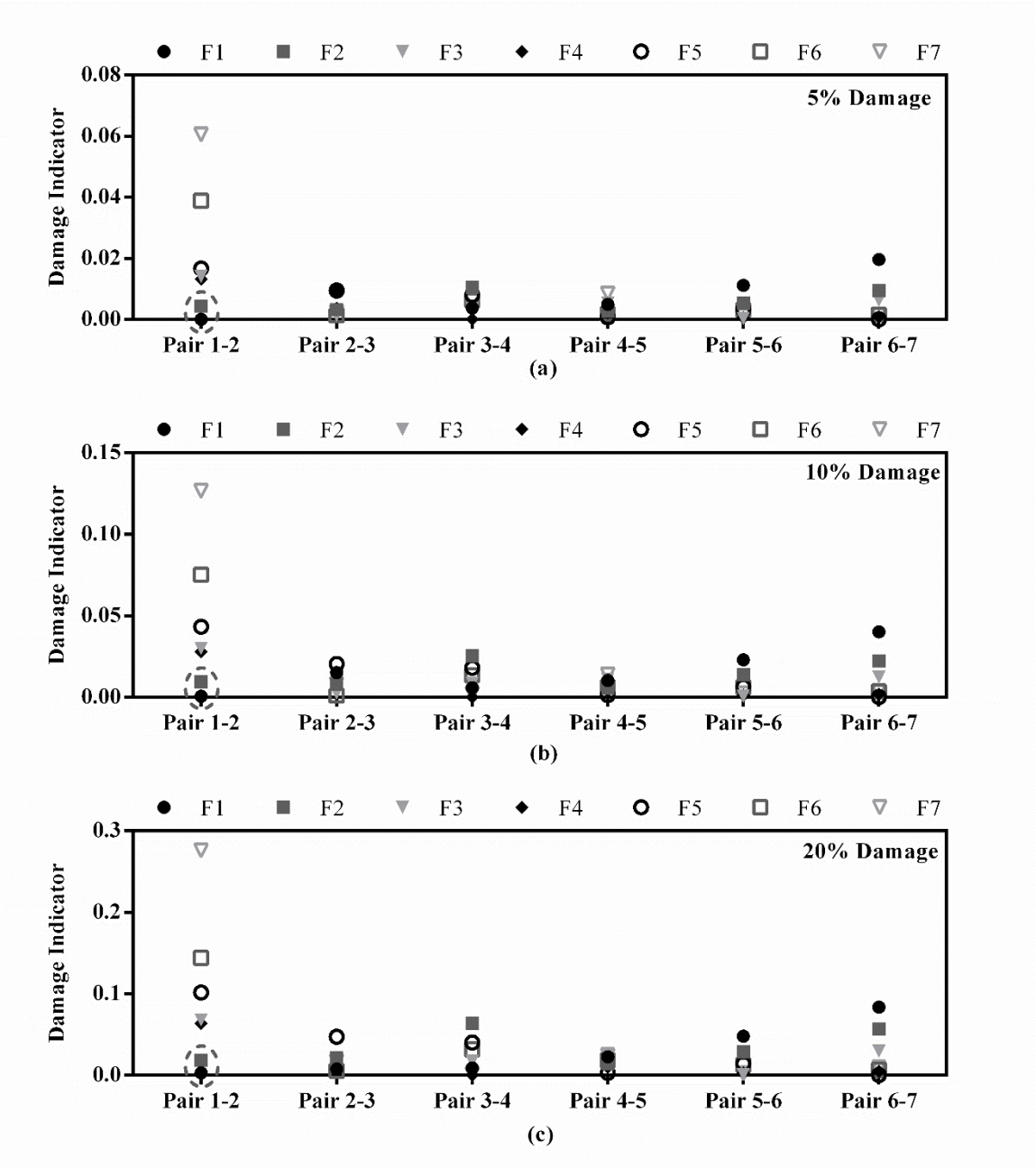

Figure 38 Damage indicator calculated from transmissibility from adjacent pairs of nodes on cantilever for forces applied at each node: (a) 5 percent reduction in stiffness at damage location A, (b) 10 percent reduction in stiffness at damage location A, (c) 20 percent reduction in stiffness at damage location A

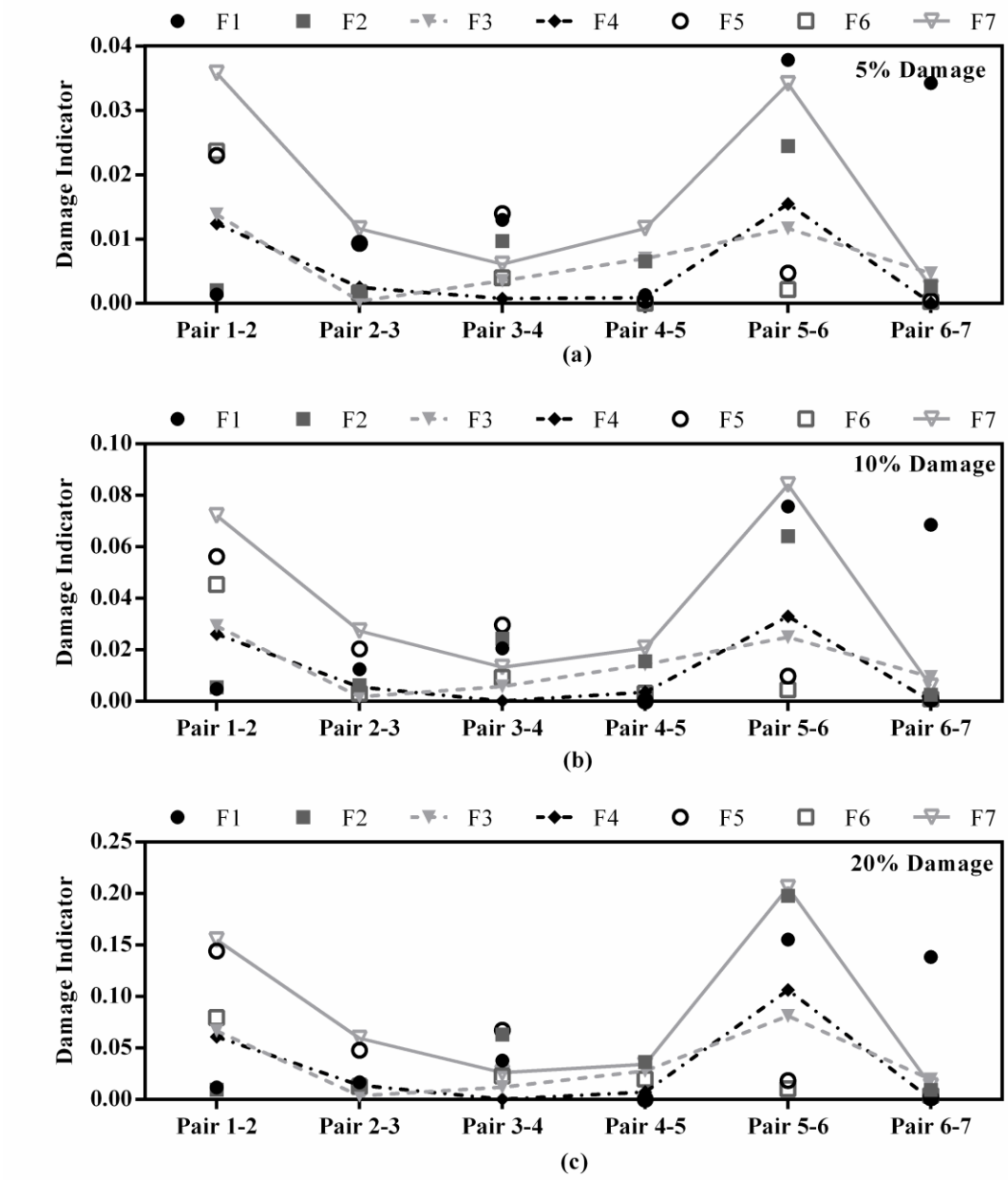

Figure 39 Damage indicator calculated from transmissibility from adjacent pairs of nodes on beam for forces applied at each node. NOTE: Data groups with connecting lines emphasize the data groups in which the force is not applied to either damage location: (a) 5 percent reduction in stiffness at damage locations A and B, (b) 10 percent reduction in stiffness at damage locations A and B, (c) 20 percent reduction in stiffness at damage locations A and B

4.3.3. Parametric Pin-Pin Beam Discussion

Figure 38 shows that the magnitude of the damage indicator is greatest for pair 1-2, which correctly locates the damage at damage location A. It is noted that when the force is at locations 1 or 2 (emphasized by the gray dashed circle), the damage indicator does not accurately detect nor locate the damage. This observation follows the same trend as the cantilever, thus establishing the theory that damage cannot be accurately detected when the force is applied at the damage location, regardless of boundary conditions.

The plots shown in Figure 39 are the results from identical damage applied simultaneously at both damage locations A and B, with connecting lines used to highlight the data sets in which the impulse is not applied to either damage location. It can be seen that for all damage severities, the three highlighted loading scenarios accurately depict the correct damage arrangement. This is seen by the magnitude of the damage indicators being greater at these two locations than at any other location.

Another observation that can be seen in both Figure 38 and Figure 39 is that not only is damage detection and location possible when the force is not applied near the damage location, but that damage quantification can be relatively used. By looking at a single damage indicator for a correctly identified damage location, say the F7 scenario (hollow upside down triangle) for pair 1-2 in Figure 38, as the damage doubles from 5% to 10% to 20%, the damage indicator roughly doubles as well (0.06 to 0.13 to 0.28). This trend is also seen with two damage locations. It should be noted that although identical damage was created for the two damage location scenarios, the damage indicator is not identical at both locations.

4.4. Numerical Parametric Testing on Representation of Sacrificial Specimen

A more realistic simulation was conducted in order to investigate the parametric effects of force and sensor location by modeling the sacrificial specimen that was analyzed previously, along with the strut and floor beam. The purpose of this parametric test was to identify whether or not the observations seen with the previous parametric studies hold true for more realistic structural systems.

4.4.1. Parametric Sacrificial Specimen Setup and Testing Procedure

The numerical model created for this parametric study is shown in Figure 40, which depicts the sacrificial specimen, strut and floor beam system previously investigated. The dimensions of the model match those of the field testing specimens. A single impact force was roved across seven locations (labeled FL1 through FL7), and acceleration responses were collected for thirteen different locations (labeled A1 through A13). Damage was modeled as a 50 mm seam crack at the location shown, which matches the expected crack location for the field testing. The damage indicator methodology was utilized to determine whether or not observations similar to those of the cantilever and pin-pin beam analyses would be identified.

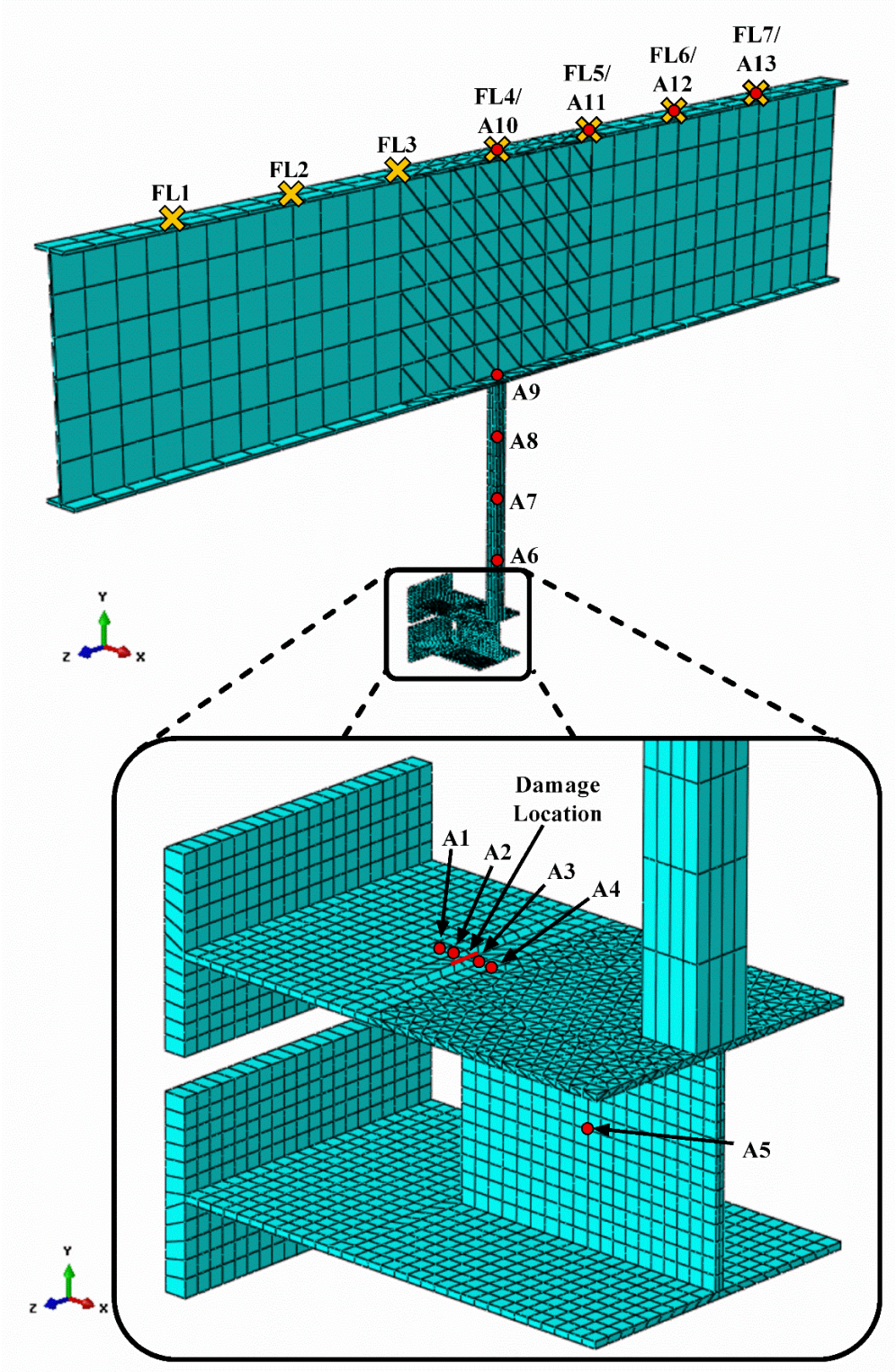

Figure 40 Parametric sacrificial specimen with strut and floor beam modeled. Sensor locations and locations of applied force are shown as red circles and orange 'X's, respectively

4.4.2. Parametric Sacrificial Specimen Results

Utilizing a similar process to the cantilever and pin-pin beam, the acceleration time-history responses were used to calculate the damage indicator between pairs of nodes; however, for this study, the reference node was to remain stationary such that the effect of sensor location could be further investigated. Figure 41 and Figure 42 show the plots for damage indicator for the sacrificial specimen with varying response sensors while keeping the reference sensor (A1 and A2, respectively) stationary, both for varying force locations.

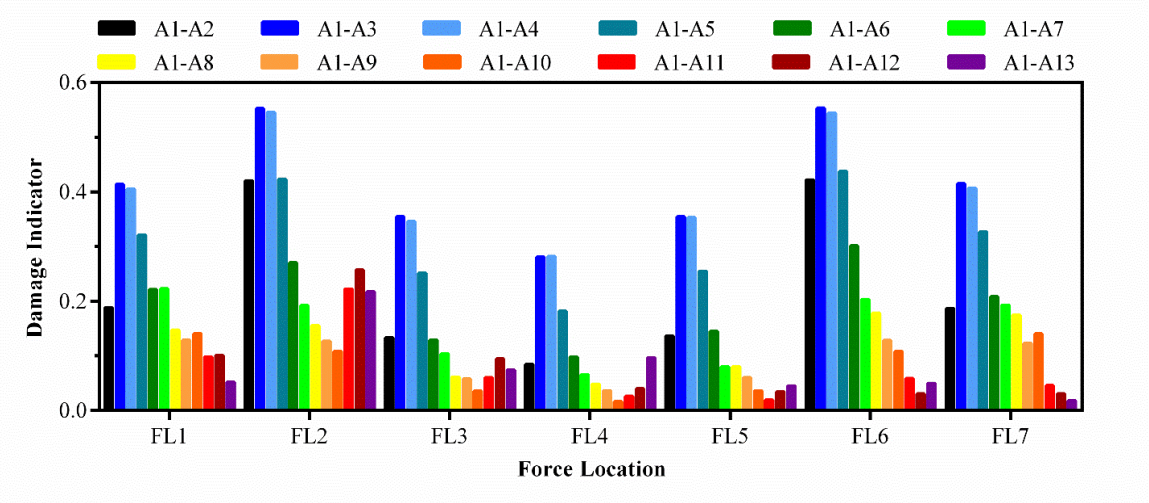

Figure 41 Damage indicator calculated from transmissibility in the Y-direction from non-adjacent pairs of nodes (A1 as reference) on sacrificial specimen system for forces applied at various locations

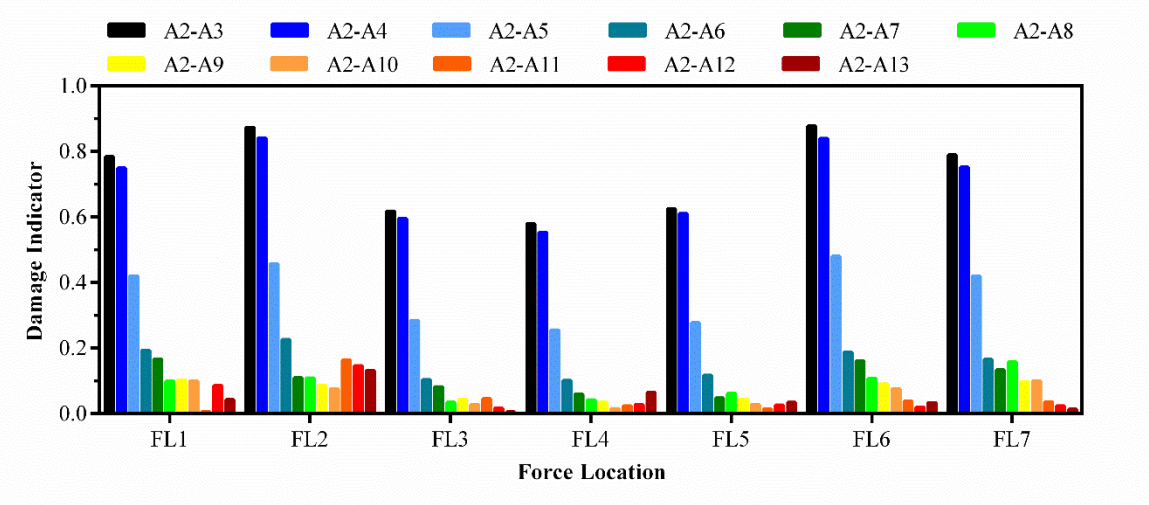

Figure 42 Damage indicator calculated from transmissibility in the Y-direction from non-adjacent pairs of nodes (A2 as reference) on sacrificial specimen system for forces applied at various locations

It can be seen from these two figures that the damage indicator is affected by force location, as indicated by the magnitude change from FL1 to FL4 (FL4 to FL7 mirror the results due to the symmetrical locations in which the force is applied). From this observation, the damage indicator more accurately detects damage at FL2/FL6, which does not contradict the previous findings that the force should be applied away from the damage location. It is hypothesized that FL1/FL7 do not increase the accuracy of the damage detection due to the proximity with the boundary conditions near the ends of the floor beam.

These results also depict that placing the reference sensor closer to the damage location increases the accuracy for detecting damage, as shown by the higher magnitude for damage indicator between A1-A3 and A2-A3. This observation supports the previous findings from the cantilever and the pin-pin beam by how damage was located from utilizing adjacent pairs of nodes. It is seen from this parametric study that as the response sensor gets further away from the damage location/reference sensor, the magnitude of the damage indicator decreases. One possible explanation for this occurrence could be due to the local sensitivity of the transmissibility function, and that the damage sensitive

features for the transmissibility diminish in significance as the sensor is placed further away from the damage.

The same model was re-analyzed with a different loading configuration in order to investigate the presence of multiple forces acting simultaneously. Four simultaneous impact forces were applied to FL1, FL3, FL5, and FL7. The results are shown in Figure 43 for varying response nodes (reference node A2). From these results, it can be observed that sensor location does affect the damage indicator, similar to what was observed when roving single impact forces. Another interesting item to notice is that the fluctuation in damage indicator magnitude near response sensors A8-A13 significantly reduces when simultaneous forces are applied.

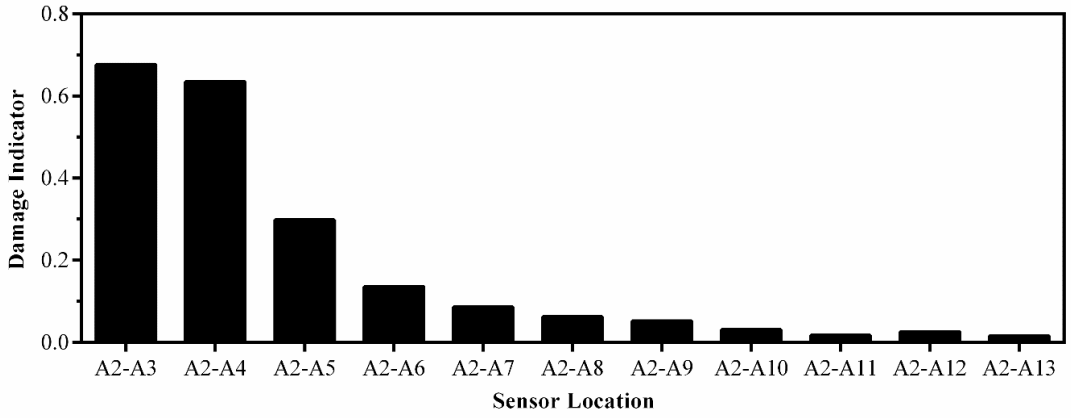

Figure 43 Damage indicator calculated from transmissibility in the Y-direction from non-adjacent pairs of nodes (A2 as reference) on sacrificial specimen system for multiple simultaneous forces

Following a thought process similar to that used in the application of multiple forces, the application of an ambient bridge acceleration time-history was utilized in order to more realistically model the system. The acceleration time history used for analysis is shown in Figure 44, and includes multiple vehicles (of varying sizes) that were measured when analyzing the field sacrificial specimen.

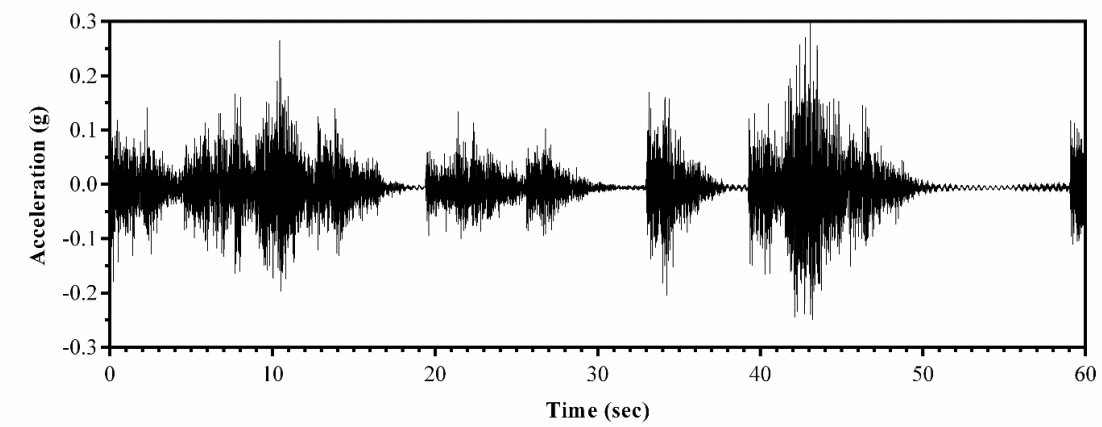

Figure 44 Acceleration time-history of ambient traffic loading measured from field testing and utilized for numerical parametric analysis

The acceleration loading was applied directly to FL1, FL3, FL5 and FL7, and five percent of the same loading was applied in the longitudinal direction of the bridge to simulate traction force, thus creating a multi-directional loading case. The results from this analysis are shown in Figure 45. It is depicted that the response sensors close to the damage, e.g. A3 through A5, were the only sensors that produced significant results. One possible justification for this could be that the application of the acceleration time-history does not excite the damage sensitive frequencies in the nodes far away from the damage.

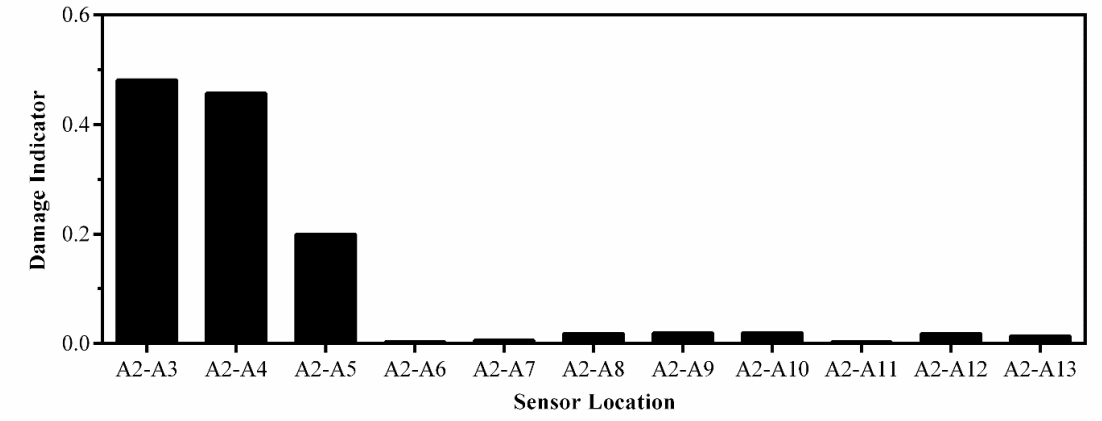

Figure 45 Damage indicator calculated from transmissibility in the Y-direction from non-adjacent pairs of nodes (A2 as reference) on sacrificial specimen system for multiple simultaneous acceleration loadings

The final investigation for this parametric study on the numerical sacrificial specimen was to examine the effect of sensor orientation on the damage indicator. Figure 46 and Figure 47 show the results for the responses taken in the X-direction and Z-direction, respectively, from a single impact force applied at various roved locations. These results are less conclusive for damage detection, primarily due to the direction in which the force is applied. Since the force is applied in the Y-direction, the signal to noise ratio for the responses in the X- and Z-directions will be low, therefore causing distorted results.

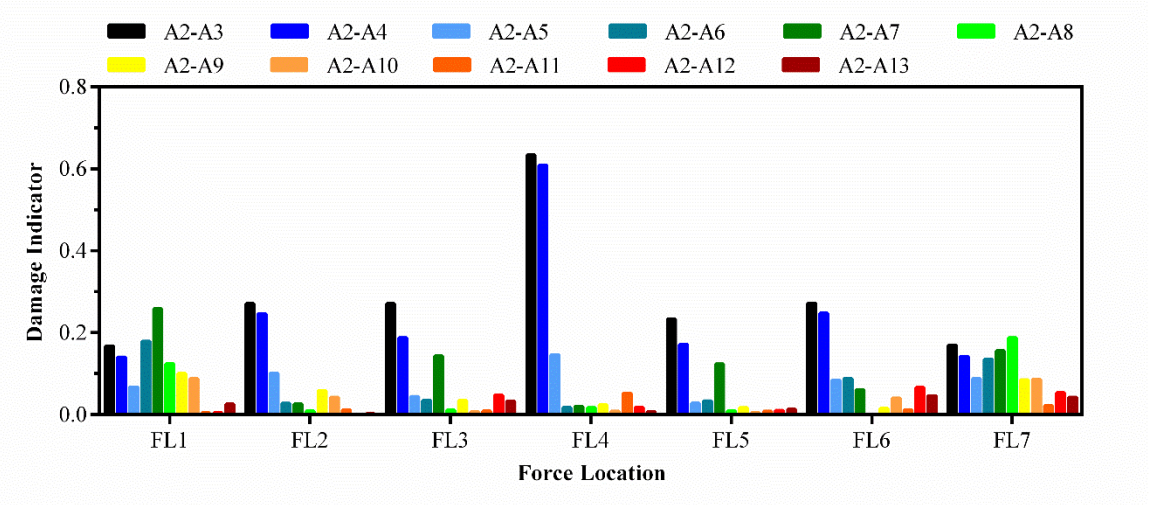

Figure 46 Damage indicator calculated from transmissibility in the X-direction from non-adjacent pairs of nodes (A2 as reference) on sacrificial specimen system for forces applied at various locations

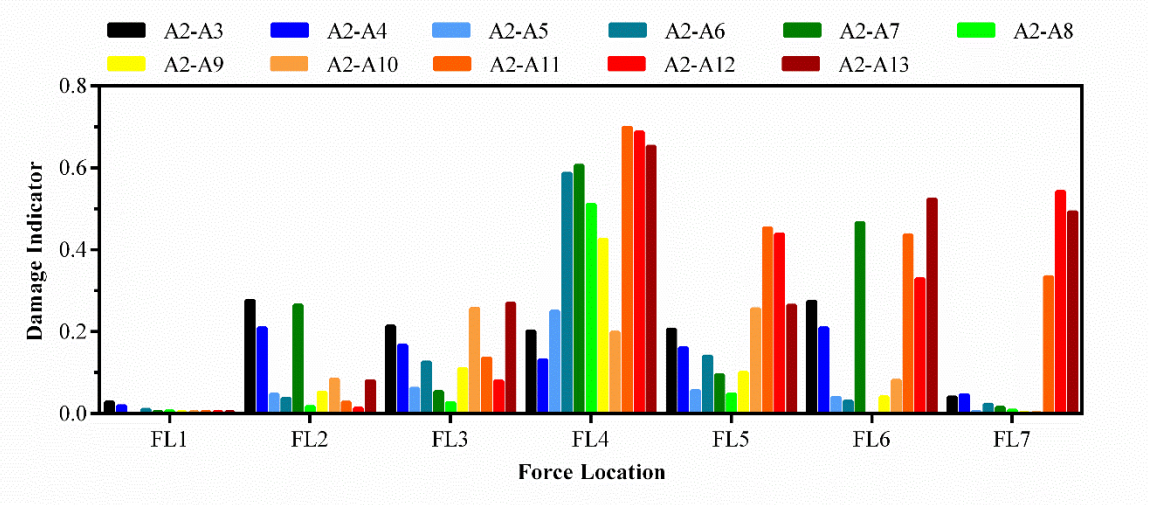

Figure 47 Damage indicator calculated from transmissibility in the Z-direction from non-adjacent pairs of nodes (A2 as reference) on sacrificial specimen system for forces applied at various locations

4.5. Numerical Parametric Testing on Girder–Floor Beam System

A model similar to the numerical sacrificial specimen was created in order to investigate the parametric effects of sensor location and orientation by modeling a girder-floor beam system. The purpose of this analysis was to further analyze the effect of sensor location and orientation on the damage indicator methodology.

4.5.1. Parametric Girder-Floor Beam System Setup and Testing Procedure

The numerical model created for this parametric study is shown in Figure 48, which depicts the girder-floor beam system. The model is a simplified version of a single-span plate-girder bridge. The girders are 27.5 m long by 2.5 deep, while the four floor beams are 8 m long and 2 m deep. Acceleration loading (Figure 44) was applied directly to the two locations shown (FL), and acceleration responses were collected for five different locations (labeled A1 through A5). Sensor location A1 was located at mid-height of the girder, while sensors A2-A5 were located at mid-height of the floor beam. Damage was modeled as a 50 mm seam crack at the location shown, which matches the crack location commonly found for this type of connection. The damage indicator methodology was

utilized to further understand the effect of sensor location and orientation on the damage indicator.

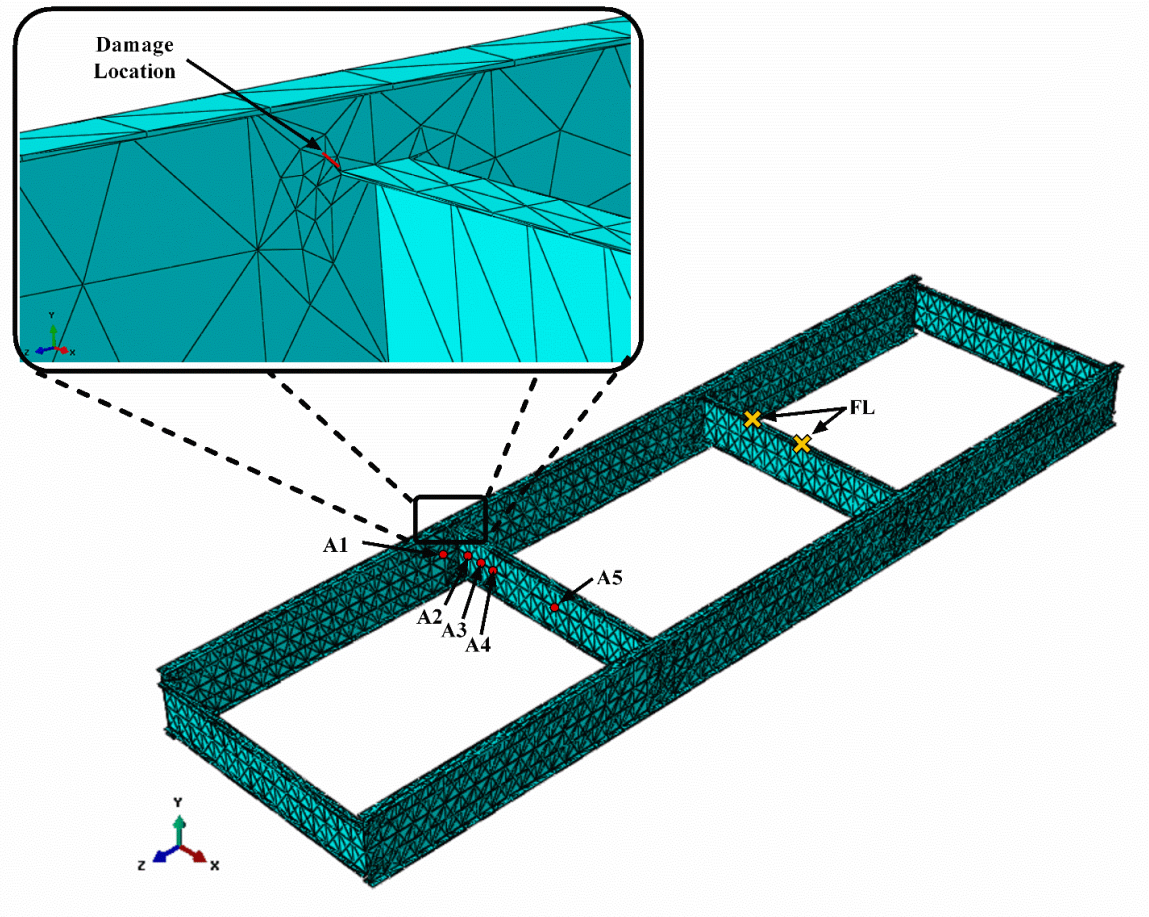

Figure 48 Parametric girder-floor beam system model used to investigate effect of sensor location and orientation. Sensor locations and locations of applied force are shown as red circles and orange 'X's, respectively

4.5.2. Parametric Girder-Floor Beam Results

The acceleration time-history responses were used to calculate the damage indicator between pairs of nodes similar to the process used for the numerical sacrificial specimen. The reference node was to remain stationary such that the effect of sensor location could be further investigated. Figure 49 shows the plots for damage indicator calculated for

different response orientations of the girder-floor beam system with varying response sensors and keeping the reference sensor (A1) stationary. Additionally, the same analysis was completed in which 5% noise was added to the input acceleration time-history.

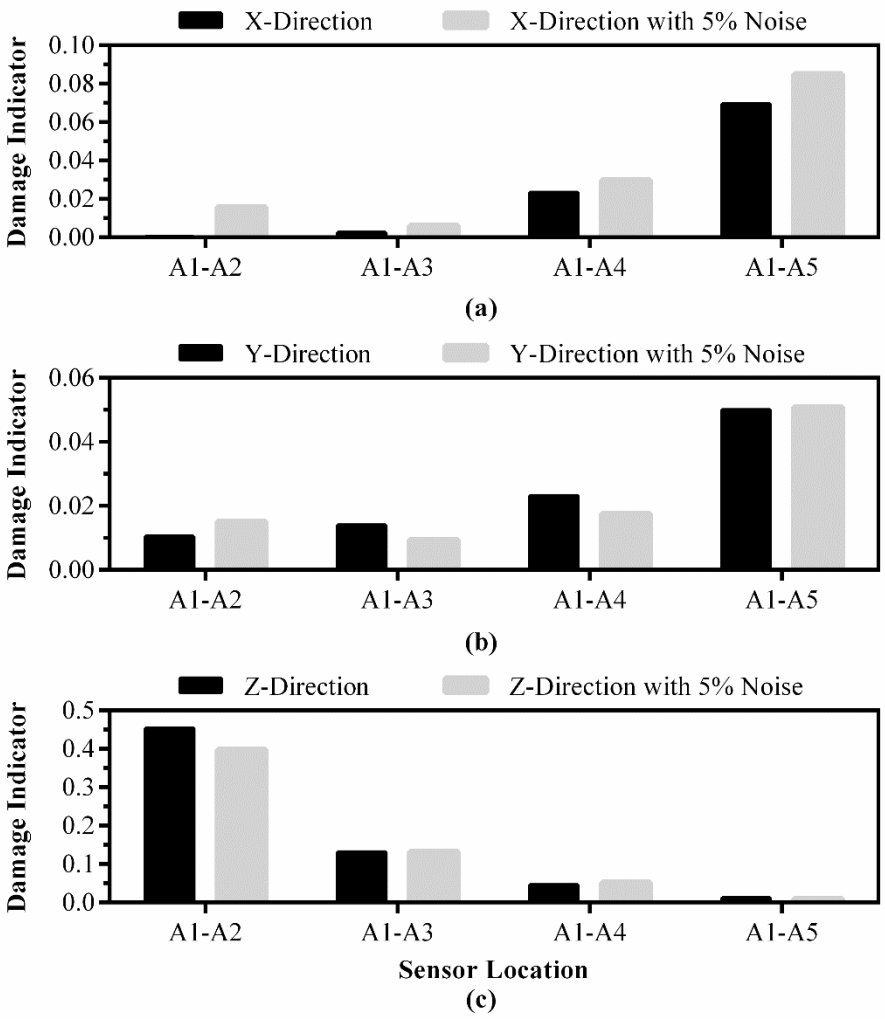

Figure 49 Damage indicator calculated from transmissibility from non-adjacent pairs of nodes (A1 as reference) on girder-floor beam system: (a) responses in the X-direction, (b) responses in the Y-direction, (c) responses in the Z-direction

It can be seen that the Z-direction is the only direction in which damage was correctly identified for response sensors near the damage location. Both the X- and Y-direction

detect damage when the response sensor is furthest from the damage location, which contradicts the findings of the previous analyses. The likely justification for this observation can be explained by understanding the concept of a load path. The load path is how energy is transmitted through the structure. By observing where the load is applied in relation to the damage as well as the sensors, it can be argued that the Z-direction has the larger magnitude of signal-to-noise ratio and/or larger region of high coherence between sensors adjacent to the damage, as compared to the other directions.

4.6. Sensitivity Analysis of Field Testing (Section A)

Throughout the testing on Section A, a sensitivity analysis was conducted to examine the effect of sensor placement and orientation on the damage-detection process. Sensor placement was examined by looking at pairs of sensors in which the reference sensor was either close to the areas of potential damage or far from said areas. Sensor orientation was investigated by comparing results from sensors oriented parallel and perpendicular to the loading direction.

A total of four pairs of sensors (Figure 21) were examined, two of which (A5-A1 and A3-A1) were oriented parallel to the loading direction (vertical), and two of which (A6-A2 and A4-A2) were perpendicular to the loading direction (horizontal). Pairs A5-A1 and A6-A2 had the reference sensor (Acc A5 and Acc A6, respectively) further from the connection, while pairs A3-A1 and A4-A2 had the reference sensor (Acc A3 and Acc A2, respectively) closer to the connection. The results from this study are shown in Figure 50. The basis contained the first two weeks of data for the pair of sensors A5-A1 (shown previously in Figure 26(a)) in order to create a reference from which to make comparisons.

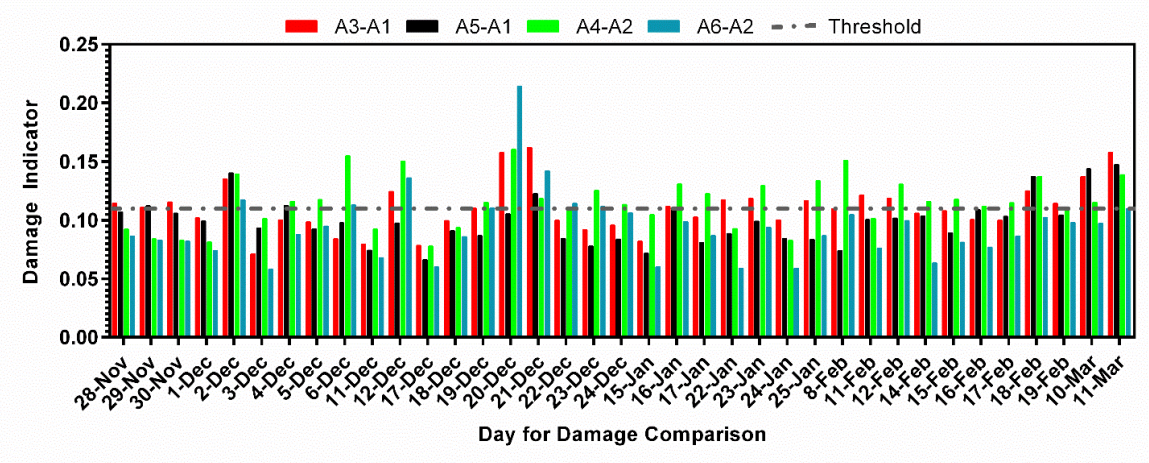

Figure 50 Parametric study using damage indicator of traffic data for multiple days compared to the baseline set for sensors at Section A. Refer to Figure 21 for sensor locations

As stated previously, the pair of sensors A5-A1 did not detect damage for the entire range of time that the bridge was monitored. The sensor pair A3-A1 shows similar characteristics to A5-A1, but there are days (2-Dec, 12-Dec, 20-Dec, and 21-Dec) in which the damage indicator exceeds the threshold. Even though these days would not send any watch or warning alarms, the fluctuation about the threshold was greater than when implementing the reference sensor far from the expected damage location. This same trend can be seen in the horizontal sensors (A4-A2 and A6-A2). It was observed that pair A4-A2 showed higher damage indicator values when compared with other pairs of sensor. This is clearly seen by the number of days that pair A4-A2 exceeded the threshold.

4.7. Overall Results and Discussion for Effect of Force Location and Boundary Conditions

It has been shown that although force location does affect the frequency response function and transmissibility, a damage detection methodology based on these parameters is still able to accurately detect damage by choosing the correct location in which to apply the excitation. This conclusion was shown numerically on a 5 degree-of-freedom spring-mass system where damage was clearly seen regardless of force location for both

FRF and transmissibility. It is noted that more useful results appeared when the force was applied at the response location for the FRF analysis, and when the force was applied away from the damage location for the transmissibility analysis.

Using the presented damage indicator algorithm, multiple damage states were successfully detected, located and relatively quantified for non-dispersive systems with different boundary conditions by applying the force at a node away from the damage. This positively correlates with the results seen with the dispersive system for the transmissibility analysis in that the better results occurred when the force was applied away from damage. This methodology also was successful in identifying dual-damage locations by utilizing this same principle. When applying the force near the location of damage, the damage indicator could not accurately detect the damage and would also falsely detect damage at other positions.

The completed analysis showed the monitoring process can potentially be completed using two sensors; however, the results from the sensitivity analysis have demonstrated the critical role of sensor locations and orientations. It is expected that the monitoring process will become more efficient when utilizing two sensors with optimal locations and orientations. From the results of the completed analyses, it has been observed that placing the sensors near the damage location will provide accurate detection results, as long as the force is applied away from the damage. It was also observed that the load path also has an effect on the orientation in which the sensors should be placed. These observations suggest that it would be more advantageous to place both sensors close to the damage-critical area and have both oriented such that the signal-to-noise ratio is the greatest (the majority of the time it will be in the direction of the load application). The reason for this is based on the perception that accelerometers have global and local sensitivity to damage. By placing one sensor close to the damage-critical area, this sensor may become more sensitive to the damage than the other sensor; thus, damage features may be magnified and more easily detected.

Chapter 5. Effect of Temperature

Previous studies have indicated that environmental parameters, among other things, are a major source of uncertainties in the dynamic response of structures [36], with temperature playing a significant role. The article by Sohn [36] gives an overview of variability types, such as temperature, boundary conditions, mass loading, and wind-induced variation, as well as methods and procedures to accommodate for these inconsistencies. Peeters et al. [65] used the data from the testing on the Z24-bridge in Switzerland to look at the effect of temperature and different loading types and found that the first and second eigen-frequencies of the bridge depict a bi-linear relationship with temperature with the bend around 0 °C. Farrar et al. [66] collected data from the Alamosa Canyon Bridge in New Mexico to study temperature and measurement noise on modal frequencies and found that these parameters do introduce significant variability to the measurements. Cornwell et al. [67] used the data from the Alamosa Canyon Bridge to show the variability in natural frequency over sets of 24-hour periods and found that the modal frequencies could vary as much as 6% during a 24-hour period. Many projects monitored active structures to determine the modal parameters of the first few modes of vibration in hopes of finding a relationship between temperature and natural frequency [62, 63, 68-71]. Gonzales et al. [72] used finite element modeling and field data to examine the variability of modal parameters due to temperature and applied the methods learned to sub-structuring techniques. Kess and Adams [35] conducted a parametric study of field data relating temperature, among other variables, and transmissibility in damage detection, and developed a variability test matrix that isolates the effect of each variability. The relationship between temperature and novelty index, which is based on transmissibility, is also well known [37]. Temperature has also been vaguely grouped with other parameters giving reason for possible sources of error within a damage detection methodology [31, 39]. It is the goal of the author to contribute to this knowledge gap.

The variability of dynamic characteristics of a structure due temperature and other factors has been studied in parallel with the development of damage detection methods. Kim et al. [64], experimented on a model bridge in which damage was created in order to study the effect temperature has on damage detection methods and found that damage could be

located using modal parameters from various temperatures. Yan et al. [40, 73], released a series of work that utilizes a principal component analysis (PCA) method for both linear and nonlinear analyses; they found that damage can be detected without measuring the environmental effects by carefully selecting the principal components not sensitive to temperature.

The goal of this chapter is to conduct a parametric study about the effect that temperature has on transmissibility and the damage indicator presented transmissibility-based methodology. Although the method has already been applied to numerical, experimental and field applications in the previous chapters, the purpose of this chapter is solely to explore the effect of temperature on the damage indicator in a controlled manner, and draw connections from these results to those described in prior chapters. This effect was studied numerically and experimentally by varying the temperature on a specimen both with and without damage. With this data, the fluctuation of the damage indicator was observed for a healthy specimen, which gives indications about how temperature affects transmissibility; furthermore, by varying the temperature for the damaged specimen, the relationship between temperature and damage indicator was observed. Section 5.1 details the background information for the effect of temperature on the dynamic response of structures as well as justifying the use of transmissibility in reducing environmental factors. Section 5.2 explains the setup and results for the numerical testing of the effect of temperature on the damage indicator methodology, and Section 5.3 depicts the setup and results from the experimental testing. The effect of temperature on the field results is provided in Section 5.4, and Section 5.5 discusses the results and presents the conclusions found by the author.

5.1. Background Information

The effect of temperature on the dynamic response of structures can be investigated by applying concepts of thermal expansion along with those from vibration. From thermodynamics, a single-degree-of-freedom bar will generally undergo a volumetric change when the temperature of the bar increases. This process is called thermal expansion and has been categorized as a monotonic relationship between temperature and volume; therefore it can be expressed by the following equation (Equation (5.1)).

$$\alpha = \frac{1}{V}\frac{dV}{dT} \tag{5.1}$$

where α is the coefficient of thermal expansion, V is volume, and T is temperature. For a 1-D problem, the volume can be reduced to the length of the bar, L, and by rearranging terms to solve for dL, the strain caused by thermal expansion, ε_T, can be calculated by Equation (5.2).

$$dL = \alpha L dT = \varepsilon_T \tag{5.2}$$

By assuming linearity and superposing thermal strain with engineering strain, one can investigate the effect of thermal expansion on the modulus of elasticity (Equation (5.3)). It is important to note that not all structures will maintain a linear relationship, and thus certain precautions must be taken to ensure the accuracy of these results. The justification for choosing linear structures is based on the presented algorithm in that the features used for calculating the damage indicator are chosen based on frequency ranges with high coherence, e.g. a strong linear relationship between nodal responses.

$$E = \frac{\sigma}{\varepsilon + \varepsilon_T} = \frac{\sigma}{dL/L + \alpha L dT/L} = \frac{\sigma}{\varepsilon + \alpha dT} \tag{5.3}$$

where E is the modulus of elasticity, σ is stress, and ε is engineering strain. With this equation, it can be seen that the modulus of elasticity is inversely proportional to the change in temperature, e.g. as temperature increases, the modulus of elasticity decreases. This is an important observation to note because the majority of structural health monitoring schemes classify a reduction in Young's modulus as damage. These methods are generally calculated from modal parameters such as natural frequency, frequency response functions (FRF), and transmissibility. Knowing that damage could be falsely detected from temperature effects, one must investigate further how environmental effects play a role in calculating modal parameters.

A simple single-degree-of-freedom (SDOF) system can be used to demonstrate how temperature can alter natural frequency, as well as transfer functions such as the frequency response function (FRF) or transmissibility. Consider the frame shown in

Figure 51(a). By simplifying this structure into an equivalent spring-mass system, a SDOF assembly can be used for analysis (as shown in Figure 51(b)).

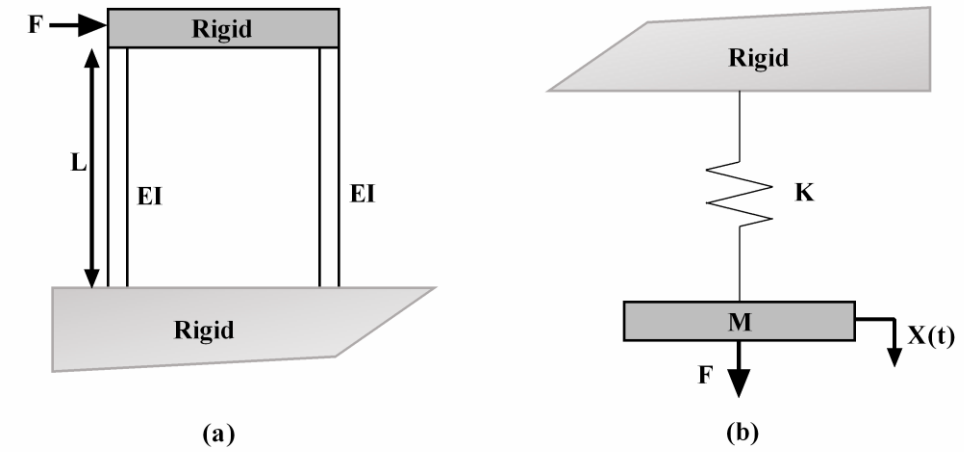

Figure 51 (a) Simple frame model (b) equivalent single-degree-of-freedom system

From the vibration of this simplified system, the natural frequency (ω_n) can easily be computed using Equation (5.4), where $K_{eq} = 6EI/L^3$ is the equivalent stiffness of the frame from Figure 51(a) and M is the mass of the system.

$$\omega_n = \sqrt{\frac{K_{eq}}{M}} = \sqrt{\frac{6EI}{L^3 M}} \tag{5.4}$$

As shown previously, temperature inversely affects the modulus of elasticity, in which E is directly proportional to natural frequency; thus, an increase in temperature will decrease the natural frequency. This observation is confirmed by many of the articles that utilize modal frequency for damage detection when they plot frequency versus temperature [62-71].

Another common modal function utilized in damage detection methodologies is the FRF. This transfer function is calculated from the displacement or acceleration response at one node due to a loading at another node. Equation (5.5) shows how the FRF is calculated for a multiple-degree-of-freedom (MDOF) system due to the lack of relevance an SDOF system would accommodate.

$$H_{jk}(\omega) = \frac{X_j(\omega)}{F_k(\omega)} = \sum_{r=1}^{N} \frac{\Phi_{ir}\Phi_{kr}}{k_r - \omega^2 m_r} \tag{5.5}$$

where $H_{jk}(\omega)$ is the FRF as a function of frequency, $X_j(\omega)$ is the response at node *j* converted to the frequency domain, $F_k(\omega)$ is the force applied at node *k* converted to the frequency domain, and Φ_{ir} and Φ_{kr} are modal matrices constructed from mass-orthogonalized eigenvectors. The summation over *r* is used for superposition of N modes of vibration. From this equation, it can be seen that temperature would affect FRF through the stiffness values and therefore would have problems in damage detection similar to those found with natural frequency.

A third common parameter used for damage detection is transmissibility, which is the major component of this work. Transmissibility is a transfer function similar to FRF with the exception that transmissibility is the ratio of two output responses while FRF is the ratio of one output response to the input force. Since the response at any node can be calculated from the FRF, the transmissibility between two nodes can also be determined by the frequency response function, as shown in Equation (5.6).

$$T_{ij}^{k}(\omega) = 20 * \log_{10}\left[\frac{X_i(\omega)}{X_j(\omega)}\right] = 20 * \log_{10}\left[\frac{\mathrm{H}_{ik}(\omega)F_k(\omega)}{\mathrm{H}_{jk}(\omega)F_k(\omega)}\right] \tag{5.6}$$

One advantage of using transmissibility is that the excitation does not need to be monitored. Work has been completed showing the benefits to using this type of methodology, including the work being presented, thus warranting the investigation into the temperature effect on this transfer function. Equation (5.7) shows that transmissibility can be calculated from the ratio of output response to input response, in which no force measurement is required.

$$T_{ij}^{k}(\omega) = 20 * \log_{10}\left[\frac{X_i(\omega)}{X_j(\omega)}\right] \equiv 20 * \left(\log_{10}\left[X_i(\omega)\right] - \log_{10}\left[X_j(\omega)\right]\right) \tag{5.7}$$

where $T_{ij}^{k}(\omega)$ is the transmissibility (dB) between nodes *i* and *j* due to a loading at node *k*. From Equation (5.7), it is noted that temperature is only related to the transmissibility through the responses at nodes *i* and *j*, and that the environmental effects are likely

reduced through subtraction of these responses by assuming the effects act equivalently at each node. This is an important observation that could lead to significant benefits for choosing transmissibility-based structural health monitoring techniques.

5.2. Numerical Temperature Testing

The following section details the processes used for testing the specimen numerically. A single specimen was designed to be used for the entirety of this work and is shown in Figure 52.

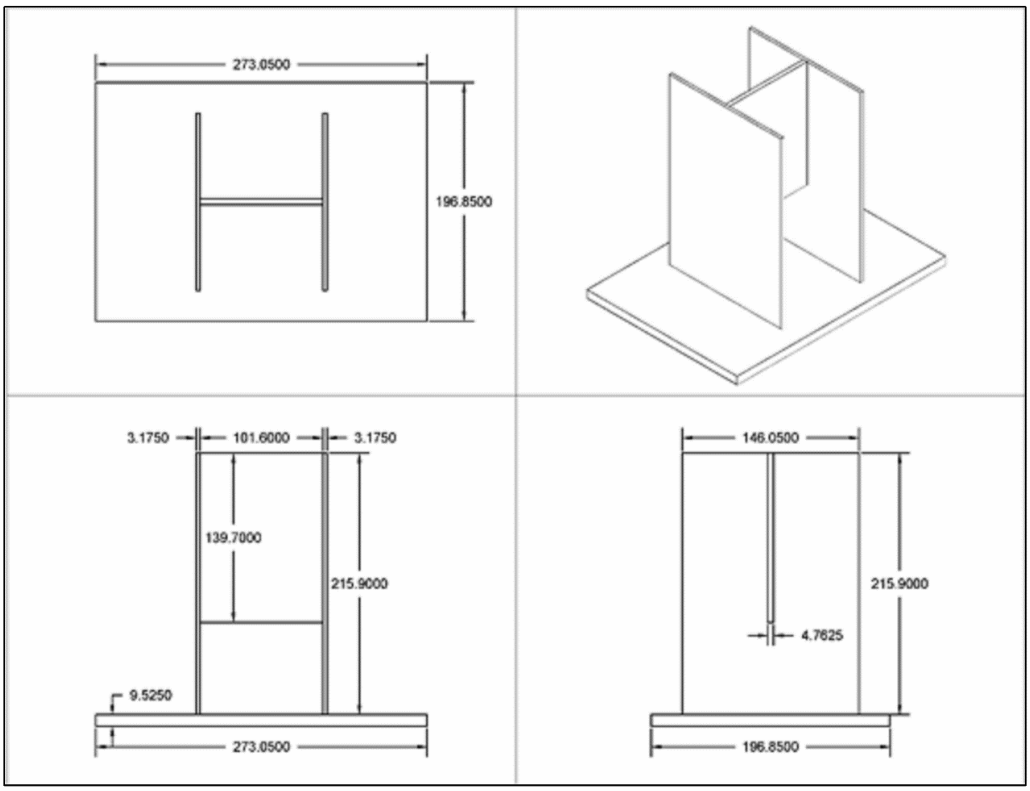

Figure 52 Schematic layout and dimensions for model used in numerical and experimental analyses

This specimen undergoes double beam curvature [50], as depicted in Figure 53. The importance of this deflection motion is that i) it is a real deformation shape found in bridges and similar structures, and ii) it can be easily damaged through accelerated fatigue techniques.

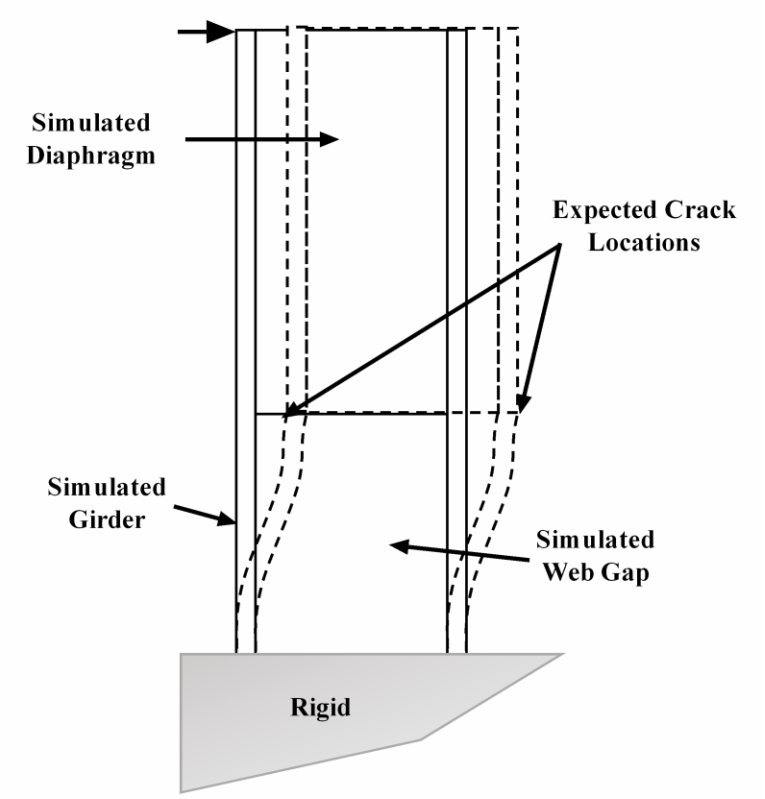

Figure 53 Double beam curvature of model showing expected crack locations due to bending near simulated web gap

5.2.1. Numerical Temperature Setup and Testing Procedure

The numerical testing was completed using the finite element program ABAQUS (ABAQUS 6.12, Dassault Systemes Simulia Corp.). An isometric view of the model created is shown in Figure 54(a). The model consists of approximately 7000 quadratic, coupled temperature-displacement brick elements (C3D20RT). An impact analysis was used for the loading, with the impulse load applied in the direction and location shown in Figure 54(a). Three nodes (located in Figure 54(a)) were used to output the acceleration response due to the impulse loading. These nodes were chosen due to their geometric symmetry, thus allowing for similar transmissibility between symmetric pairs of nodes,

i.e. pairs 2-1 and 2-3. The acceleration time-histories were then inputted into MATLAB (MATLAB R2013a, The MathWorks Inc.) in order to calculate the damage indicator.

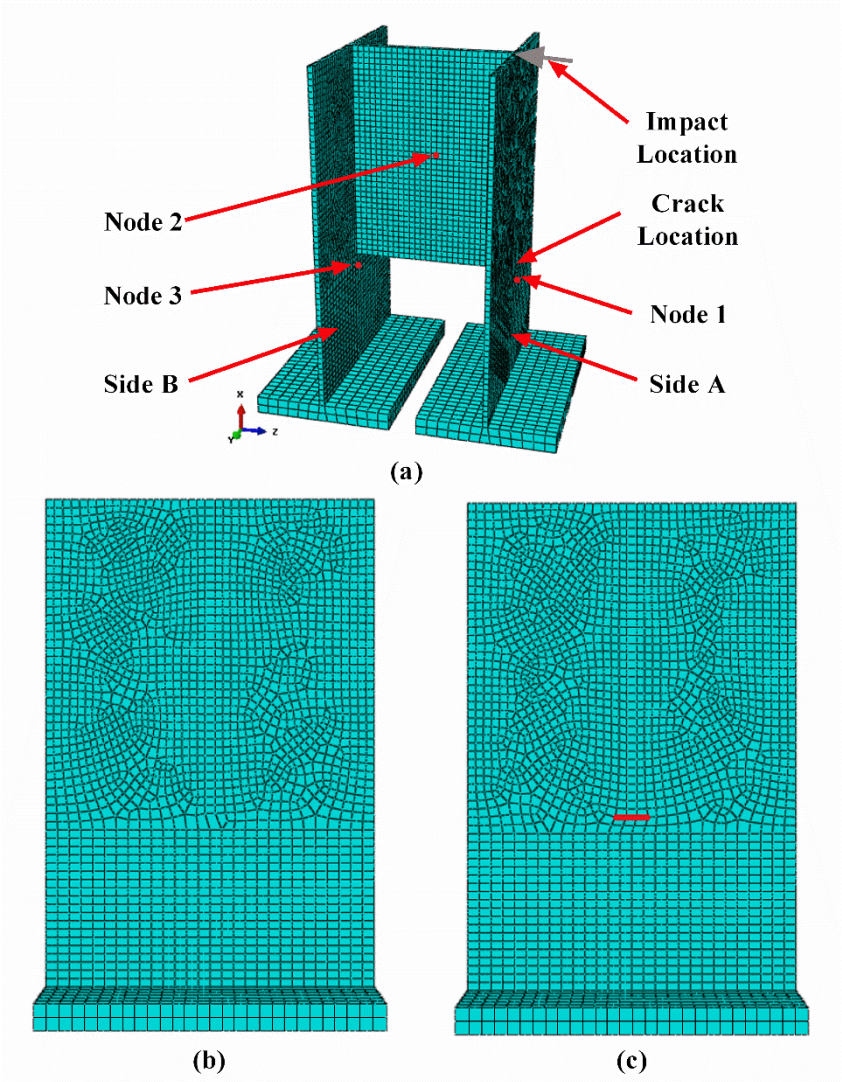

Figure 54 Numerical model used for temperature analysis: (a) isometric view showing location of nodes, force, and crack location, (b) side view of Side A for undamaged model, (c) side view of Side A for damaged model showing crack location

The procedure used to observe the relationship between temperature and the damage indicator was to run the impact analysis on the undamaged model for multiple varying temperatures. The temperature range used for this testing consisted of 31 equally spaced

temperatures from -34 °C to 49 °C. Once completed, damage was introduced into the specimen by modeling a 13 mm seam crack at the expected crack location, as shown in Figure 54(c). The crack was expected in this location due to the high stress concentration caused by the connection with the simulated diaphragm. The impact analysis was then run again for the same temperature range, this time on the damaged model. After all of these analyses were completed, a baseline set was chosen as 21 °C for the undamaged specimen. This baseline temperature was selected based on the results of the field testing from Chapter 3, in that when choosing a baseline, the day in which the temperature is near the average temperature for the testing duration provided percent-violations with a lower threshold. All other analyses were then considered as comparison sets, and the damage indicator was calculated for each temperature and each damage state (healthy or damaged).

5.2.2. Numerical Temperature Results

In order to calculate the damage indicator for the numerical model, the acceleration time-histories from all three nodes were outputted from the finite element model. A typical acceleration response is shown in Figure 55(a). By comparing symmetric pairs of nodes on the model (pair 2-1 and pair 2-3), two transmissibilities were calculated. Figure 55(b) and 55(c) show the typical transmissibility calculated for pair 2-1 and pair 2-3, respectively. Parallel to calculating the transmissibility for the pairs of sensors, the coherence was also computed from the acceleration responses. Typical plots of coherence for pairs 2-1 and 2-3 are shown in Figure 55(d) and 55(e), respectively. By observing the regions of high coherence, the damage indicator calculation was limited to the frequency range of 27 to 41 hertz (Hz.).

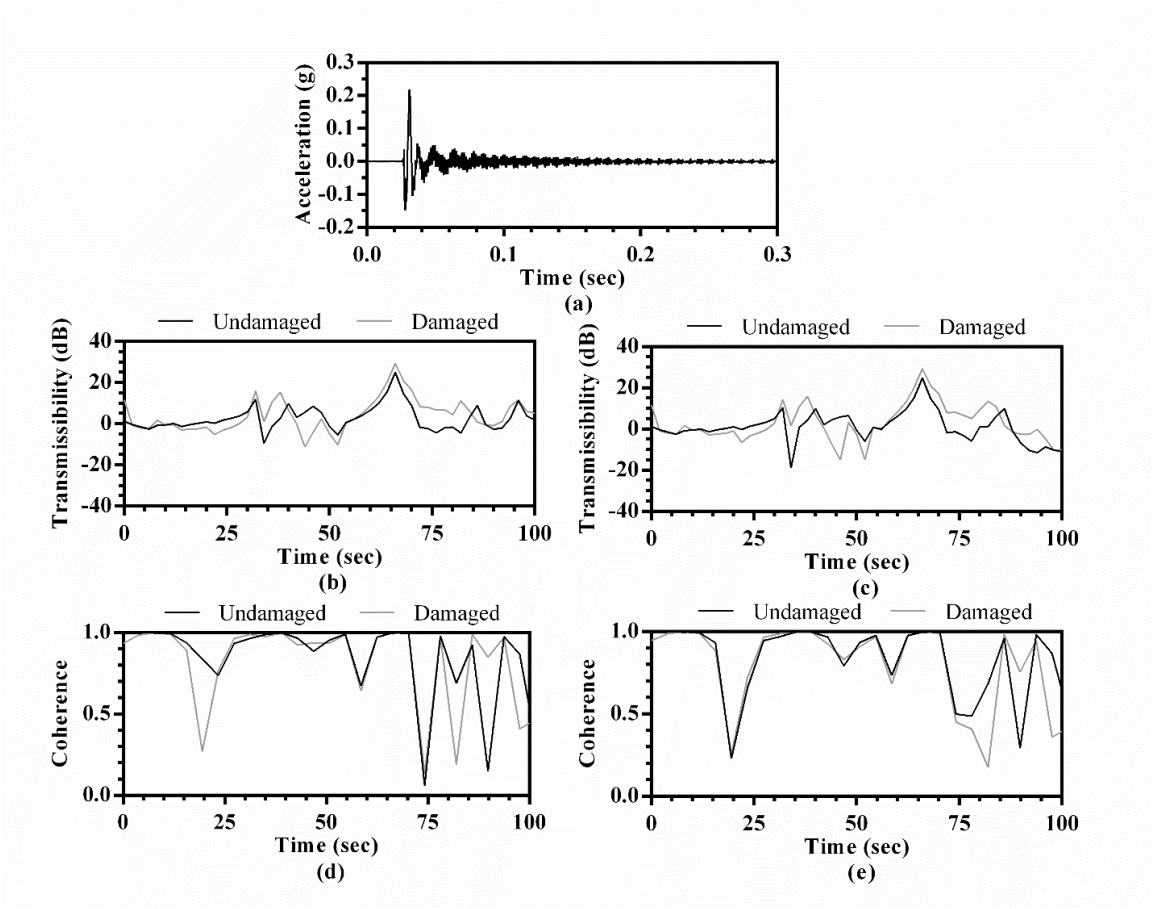

Figure 55 Typical results from numerical testing: (a) acceleration time-history response, (b) transmissibility for pair 2-1 for both damage states, (c) transmissibility for pair 2-3 for both damage states, (d) coherence for pair 2-1 for both damage states, (e) coherence for pair 2-3 for both damage states

With the frequency range limited to the region of high coherence, the damage indicator was calculated using the undamaged model with 21 °C as the baseline. The plot of temperature versus damage indicator is shown in Figure 56, with Figure 56(a) depicting the damage indicator calculated for pair 2-1 and Figure 56(b) depicting pair 2-3.

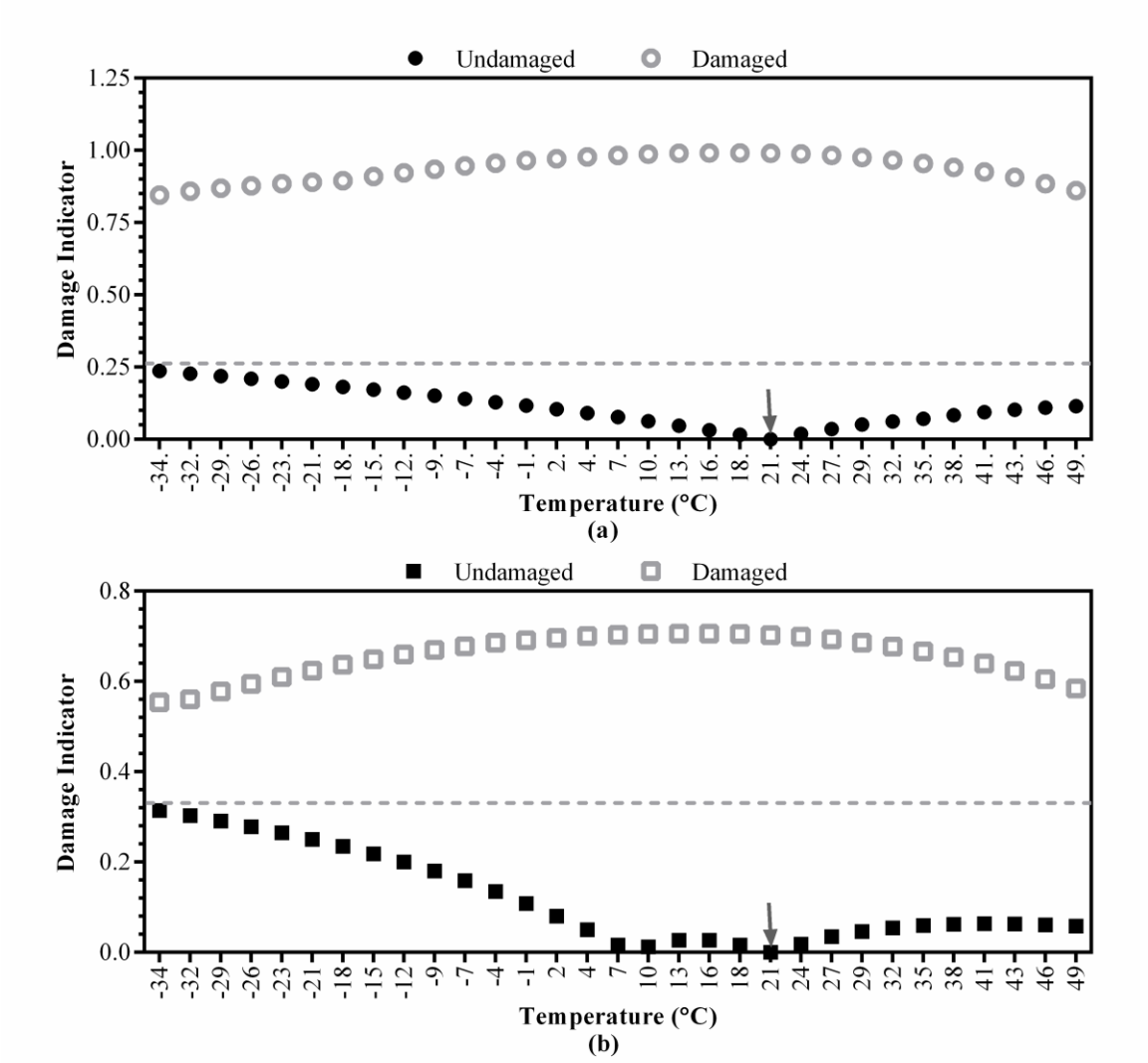

Figure 56 Damage indicator versus temperature for numerical testing. Note: the dark gray arrow points to the baseline temperature. (a) for pair 2-1 with both damage states, (b) for pair 2-3 with both damage states

It can be seen that there are two points for each temperature, one solid black and one hollow gray, which represent the undamaged and damaged model, respectively. The value of the solid black point at the baseline temperature (21 °C) is zero due to the calculation that no damage is detected from the baseline data. It is further noted that the undamaged state is expected to remain relatively close to zero as damage is not present in the model, thus the effect of temperature can be easily identified from the variation in damage indicator for the undamaged model.

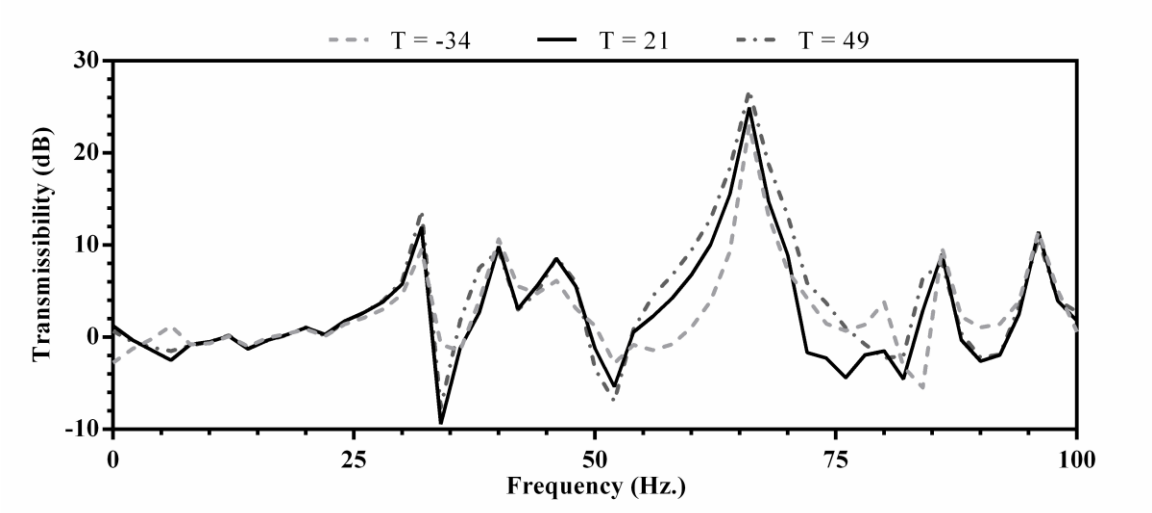

Figure 57 Temperature variation in transmissibility between nodes 1 and 2 of numerical model

It can be seen from Figure 57 that the transmissibility is affected by the temperature change in the undamaged specimen. This figure shows the baseline temperature (21 °C) as well as both extremes used in this analysis (-34 °C and 49 °C). While the overall trend and location of anti-resonances are mostly unaffected, the magnitude of the transmissibility changes with temperature, as seen around 67 Hz. From this, it can be observed that there is a possibility that damage sensitive features may exist that are unaffected by temperature.

5.3. Experimental Temperature Testing

5.3.1. Experimental Temperature Setup and Testing Procedure

The experimental testing was conducted on a specimen with the same layout and dimensions as shown in Figure 52 and constructed by welding plates of structural steel together. The welding was slightly overdesigned to prevent unwanted cracking at the connection between plates, thus forcing the crack to occur in the steel plate at the same location as in the numerical analysis. Figure 58 shows the experimental setup with the sensor locations (five accelerometers and three thermocouples) and the force location (caused by an impact hammer with a silicon tip).

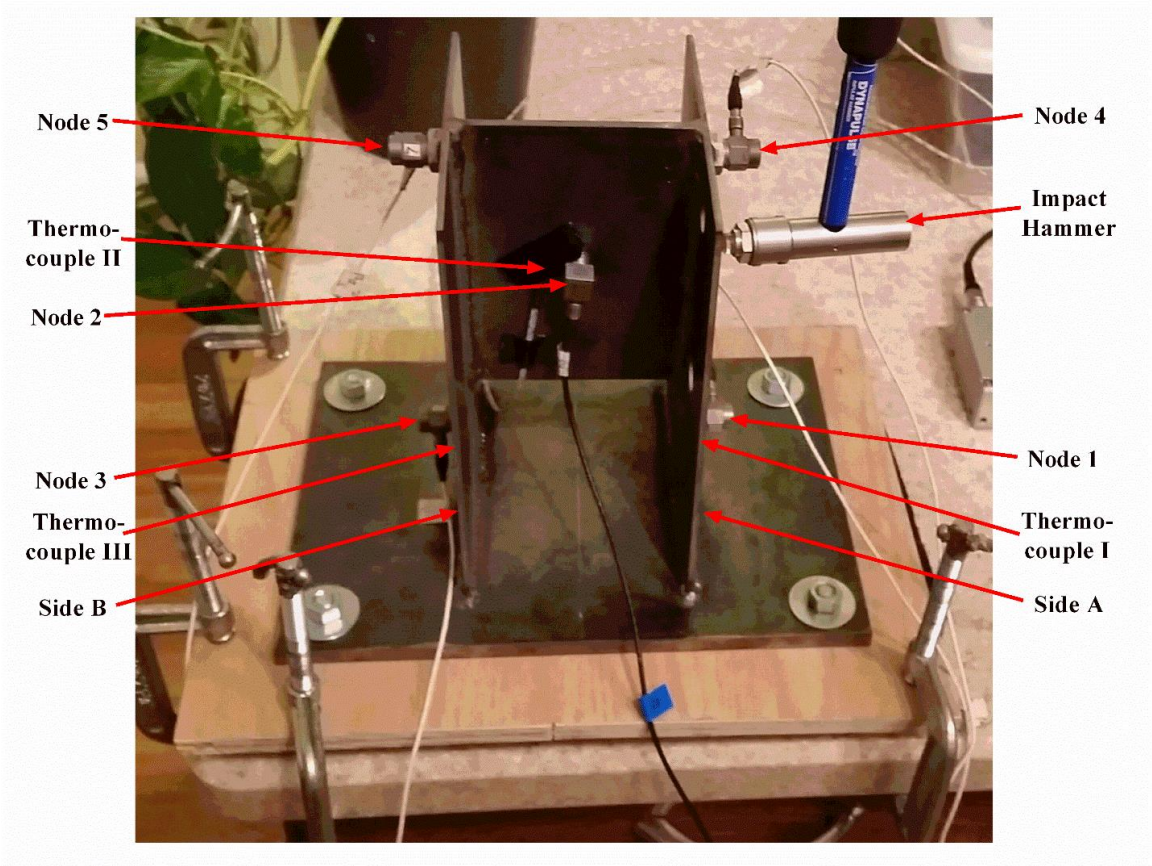

Figure 58 Setup for experimental testing showing location of nodes, force, and thermocouples

The relationship between temperature and the response of the specimen was investigated experimentally by heating and cooling the specimen to various temperatures and measuring the acceleration response due to impacts at pre-determined temperatures. This process was completed in two steps in order to cover both extreme temperatures. First, the specimen was placed in a freezer set to -5 °C for a minimum of 24 hours, as shown in Figure 59(a). With the remainder of the equipment, i.e. sensors, data acquisition hardware, etc., nearby and ready, the specimen was removed from the freezer, placed on rubber pads for vibration isolation, and clamped to a countertop for rigidity. The sensors were quickly attached, and the hardware began monitoring the response of the specimen. The goal of the experiment was to collect twenty impact responses for each one degree Celsius from the beginning of the monitoring process until the specimen reached room temperature (21 °C). The second step of this experiment was to place the specimen in an

oven set to 45 °C, as shown in Figure 59(b), and repeat similar to step one, except starting at a higher temperature and monitoring responses until the specimen reached room temperature (26 °C). Each of these steps took approximately four hours to complete, i.e. it took approximately four hours for the specimen to reach room temperature from both cooled and heated states. It was noted that the temperature increased quickly when initially being pulled from the freezer and quickly decreased when initially pulled from the oven. Since the sensors needed to be placed before monitoring began, a few degrees were not able to be observed, i.e. temperatures were measured from -1 °C to 42 °C in lieu of the equipment's specified temperature range of -5 °C to 45 °C.

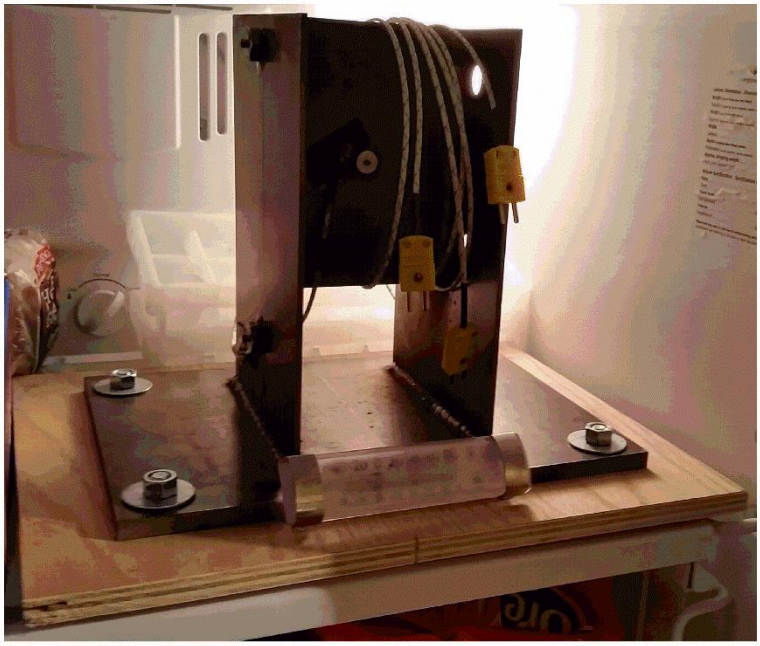

(a)

(b)

Figure 59 Experimental specimen under extreme temperatures: (a) specimen in freezer to reach extreme cold, (b) specimen in oven to reach extreme hot

Damage was also introduced into the specimen such that temperature effects on damage detection could be investigated. In order to create damage within the steel specimen, a variable-speed motor with an eccentric mass (further referred to as a shaker) was used. The shaker (model SCR-200, VIBCO Inc.) and additional masses were attached to the sides of the specimen and vibrated around the natural frequency of the specimen until a fatigue crack initiated. The purpose of the additional masses was to reduce the natural

frequency of the specimen to within the operational range of the shaker, as well as to add more driving force for the vibration.

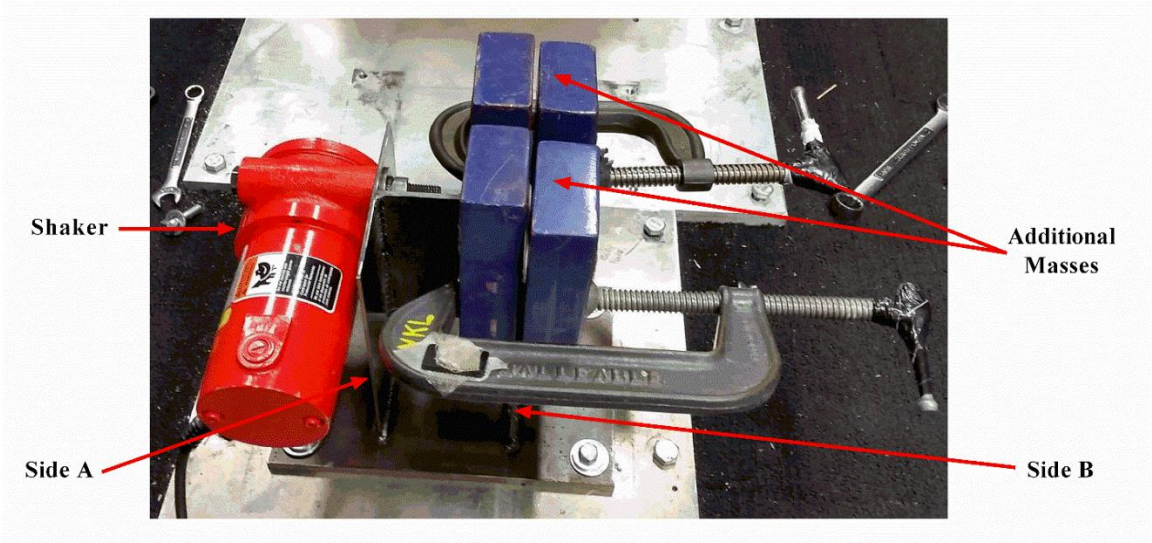

Figure 60 Setup for damage of experimental specimen showing shaker and additional masses

After vibrating the specimen for multiple thirty-second to one-minute intervals, totaling approximately ten minutes, two cracks were observed, one on each side of the specimen. The 50 mm crack on Side A is shown in Figure 61(a) and was likely caused by the connection to the shaker as the crack traces the radial mounting surface. The 26 mm crack on Side B is shown in Figure 61(b) and was the fatigue crack that was expected to occur.

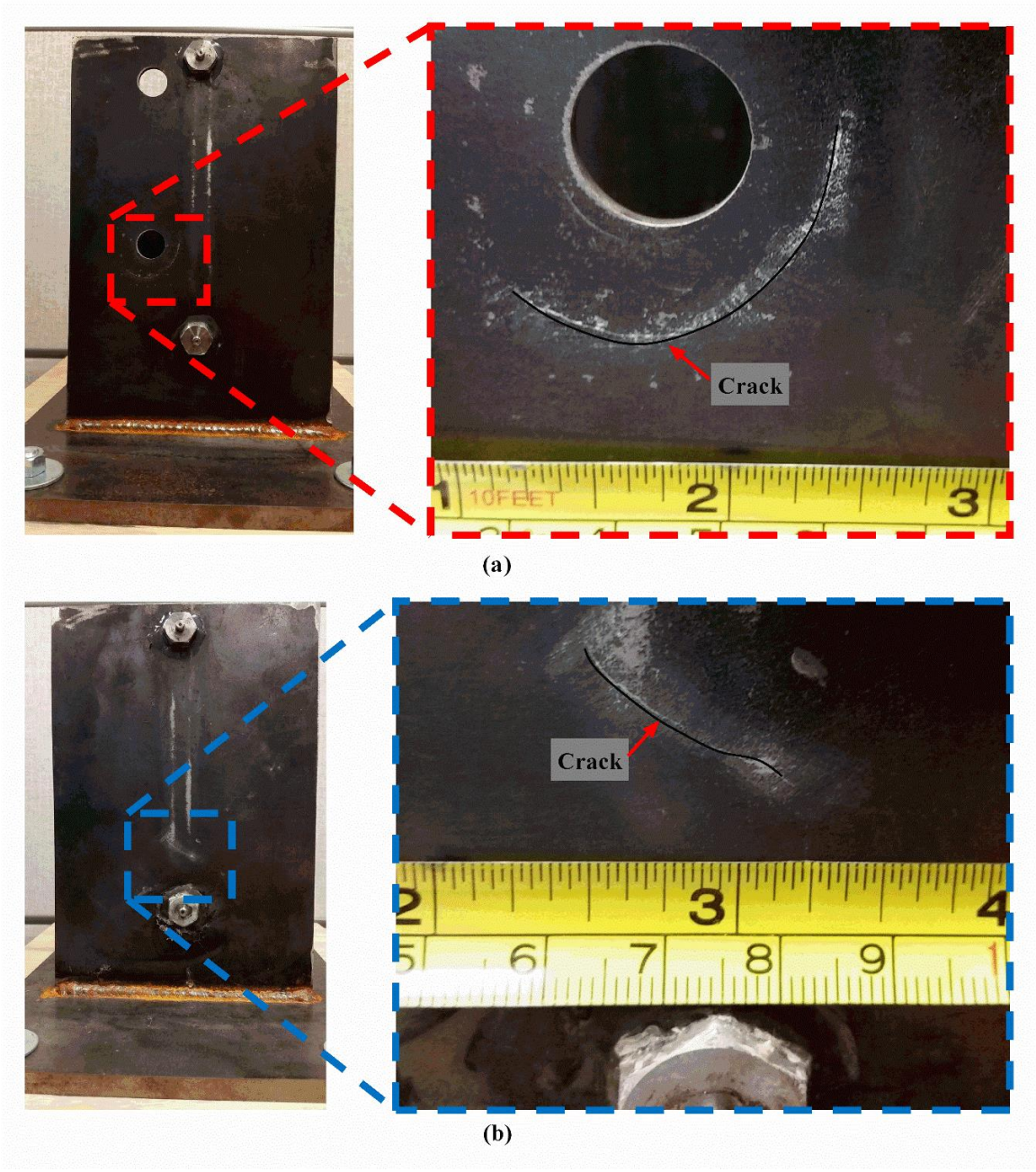

Figure 61 Damage created on experimental specimen: (a) 50 mm crack on Side A near the mounting surface for the shaker, (b) 26 mm crack on Side B in the expected crack location

After initiating the crack in the specimen, the same two-step process for monitoring the cooling and heating of the specimen was conducted. By repeating this thermal process for the damaged specimen, the relationship between temperature and damage indicator was further explored for damage detection.

5.3.2. Experimental Temperature Results

Similar to the numerical testing, the acceleration time-histories from nodes 1, 2, and 3 were used to calculate the damage indicator for symmetric pairs 2-1 and 2-3. Since the heating and cooling of the specimen were completed in two steps, the calculation of damage indicator needed to be prepared in two steps. A typical acceleration response for the cooling stage is shown in Figure 62(a), with the transmissibilities for pairs 2-1 and 2-3 shown in Figure 62(b) and 62(c), respectively. The coherence for pair 2-1 is shown in Figure 62(d) and for pair 2-3 is shown in Figure 62(e). The region of high coherence used to limit the frequency range of the damage indicator was found to be 55 to 300 Hz.

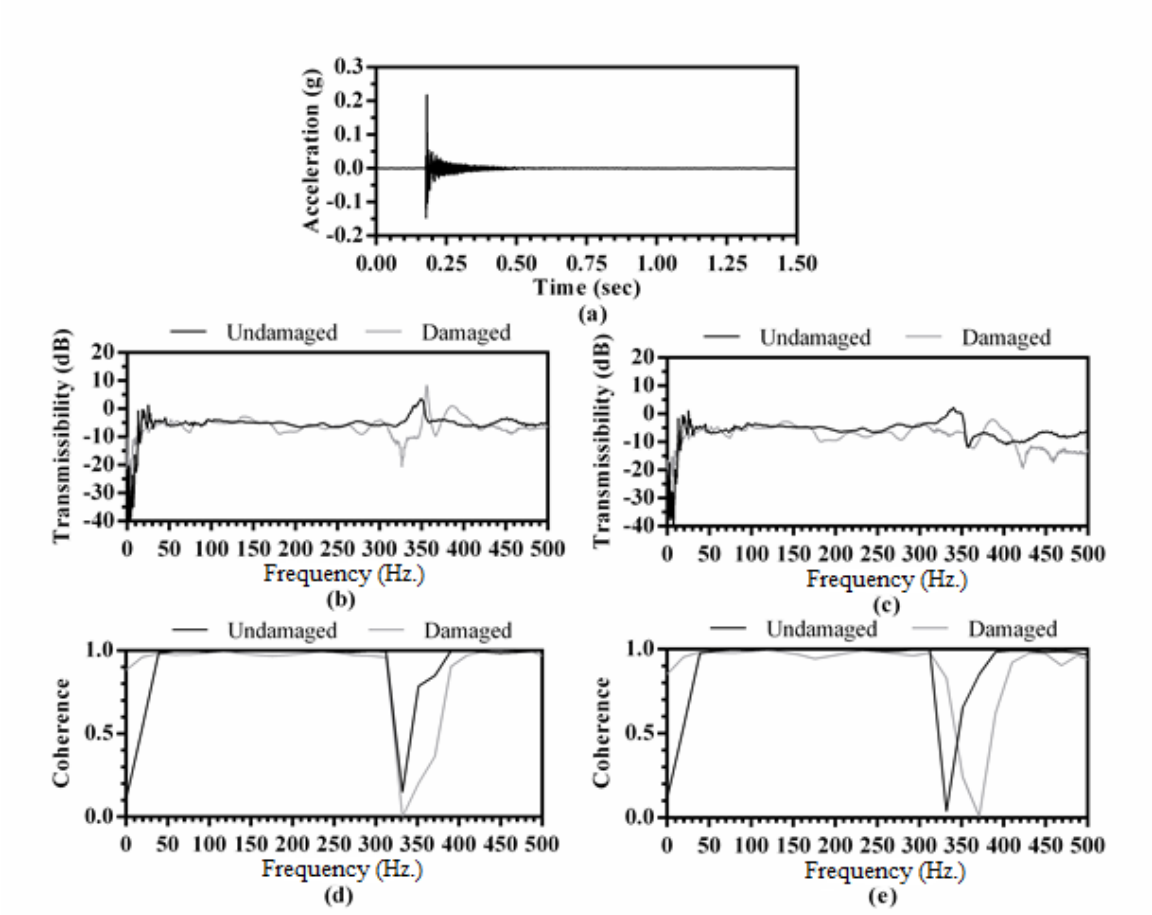

Figure 62 Typical results from experimental testing of cold temperatures: (a) acceleration time-history response, (b) transmissibility for pair 2-1 for both damage states, (c) transmissibility for pair 2-3 for both damage states, (d) coherence for pair 2-1 for both damage states, (e) coherence for pair 2-3 for both damage states

Figure 63(a-e) illustrates the same information as Figure 62(a-e) with the exception that Figure 63 was constructed using the heated specimen data in lieu of the cooled specimen data used for Figure 62. It is noted that the same frequency range (55-300 Hz.) was chosen for the heated specimen.

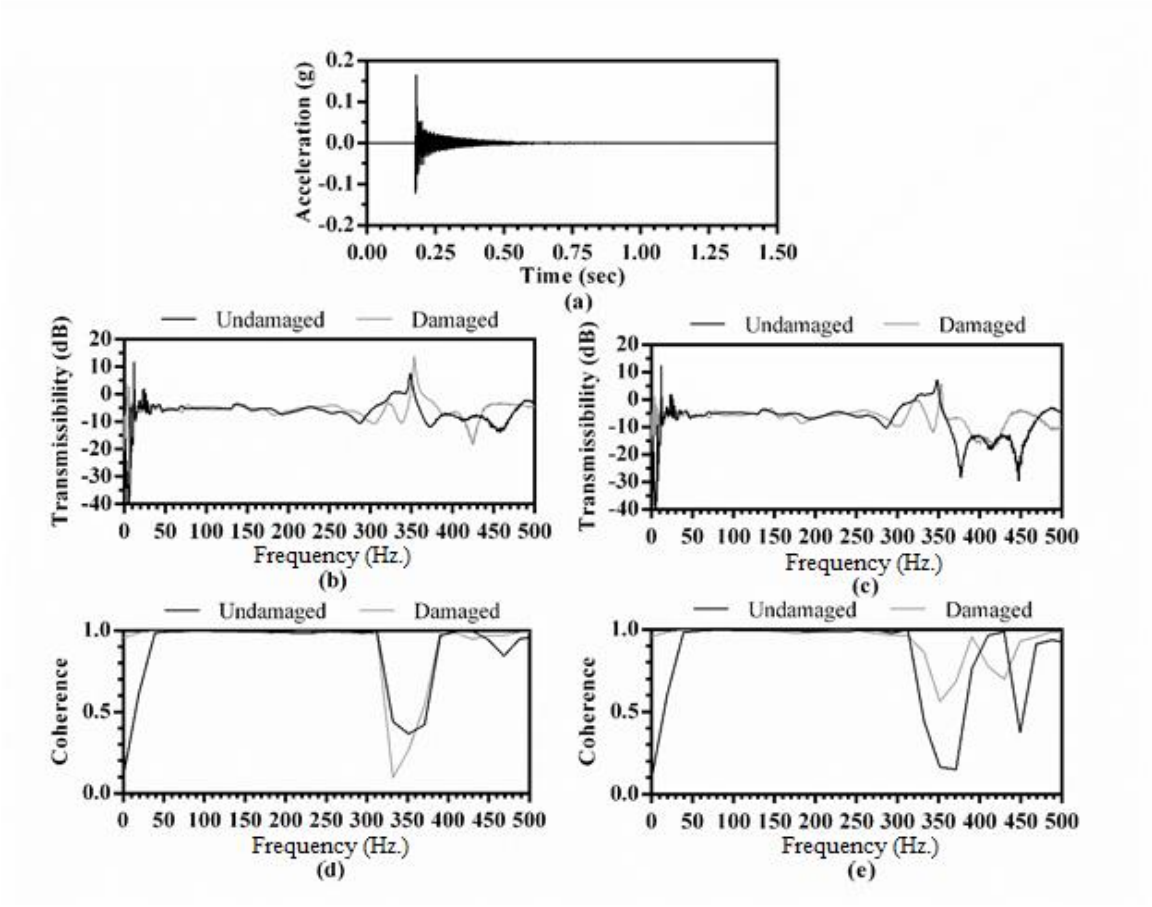

Figure 63 Typical results from experimental testing of hot temperatures: (a) acceleration time-history response, (b) transmissibility for pair 2-1 for both damage states, (c) transmissibility for pair 2-3 for both damage states, (d) coherence for pair 2-1 for both damage states, (e) coherence for pair 2-3 for both damage states

The calculation of the damage indicator was completed twice in order to cover the entire range of temperatures. The first calculation, heretofore referred to as the cold set, used the undamaged model with 21 °C as the baseline, and utilized the cold temperatures (-1 °C to 20 °C) as comparison sets. The second calculation, heretofore referred to as the hot set, used the undamaged model with 26 °C as the baseline with the hot temperatures (27 °C to 42°C) as the comparison sets. The combined plot of temperature versus damage indicator is shown in Figure 64, with Figure 64(a) depicting the damage indicator calculated for pair 2-1 and Figure 64(b) depicting pair 2-3. It is noted that in Figure 64,

the two sets of damage indicator calculations (cold and hot) are separated by a dark gray line and two dark gray arrows point to the baseline temperatures used in each set.

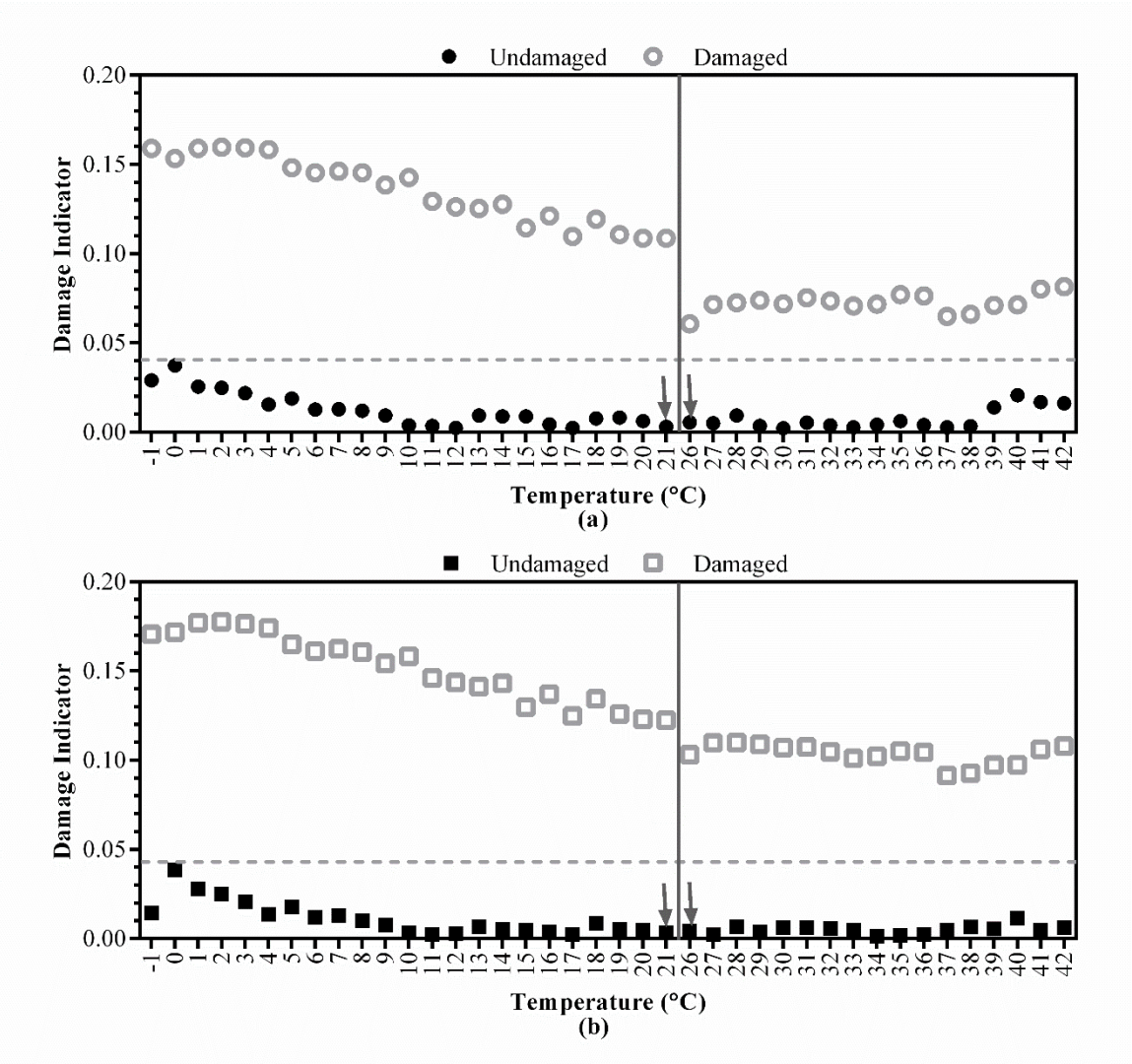

Figure 64 Damage indicator versus temperature for experimental testing. Note: the dark gray arrows point to the baseline temperatures and the dark gray line separates the 'Cold' and 'Hot' data sets. (a) for pair 2-1 with both damage states, (b) for pair 2-3 with both damage states

Similar to Figure 56, it can be seen that there are two points for each temperature, one solid black and one hollow gray, which represent the undamaged and damaged model, respectively. As with the numerical analysis, the undamaged state is expected to remain relatively close to zero as damage had not yet been initiated.

5.4. Field Temperature Testing

5.4.1. Field Temperature Results

5.4.1.1. Sacrificial Specimen Operational Load Results

As previously discussed in Chapter 3, the field testing results showed variation in the damage indicator that could possibly be explained as temperature variation. Figure 23 shows the damage indicators for each day compared to the baseline. As shown, the healthy days (13-Sep through 25-Sep) were used as the basis, thus all the damage indicators are within the threshold, and all other days clearly detect damage within the sacrificial specimen for the consecutive crack levels (D1 – 30 mm), (D2 – 40 mm), and (D3 – 60 mm), shown respectively in Figure 20(b) and 20(c), for the days in the period 13-Sept through 6-Nov. While with damage all damage indicators crosses the threshold, there are some variations between the damage indicator on different days, and that may be related to the effect of the changes in the environmental and loading parameters during the testing period, with temperature probably playing a major part [62-64] in masking damage features. The average daily temperature was calculated by determining the arithmetic mean of temperatures from each data file used in the baseline and comparison sets, resulting in a single temperature value for each day. As shown in Figure 66(a), the temperature ranged from 10 °C to 28 °C during the testing period, and there are some similarities between the temperature's variation trend and those of the damage indicator presented in Figure 23(a). The proposed algorithm was also tested under a new baseline day with an average daily temperature of 11 °C (22 September 2012, representing the coldest day for the healthy data). Figure 23(b) shows that the new baseline did not much change the characteristics being seen in Figure 23(a).

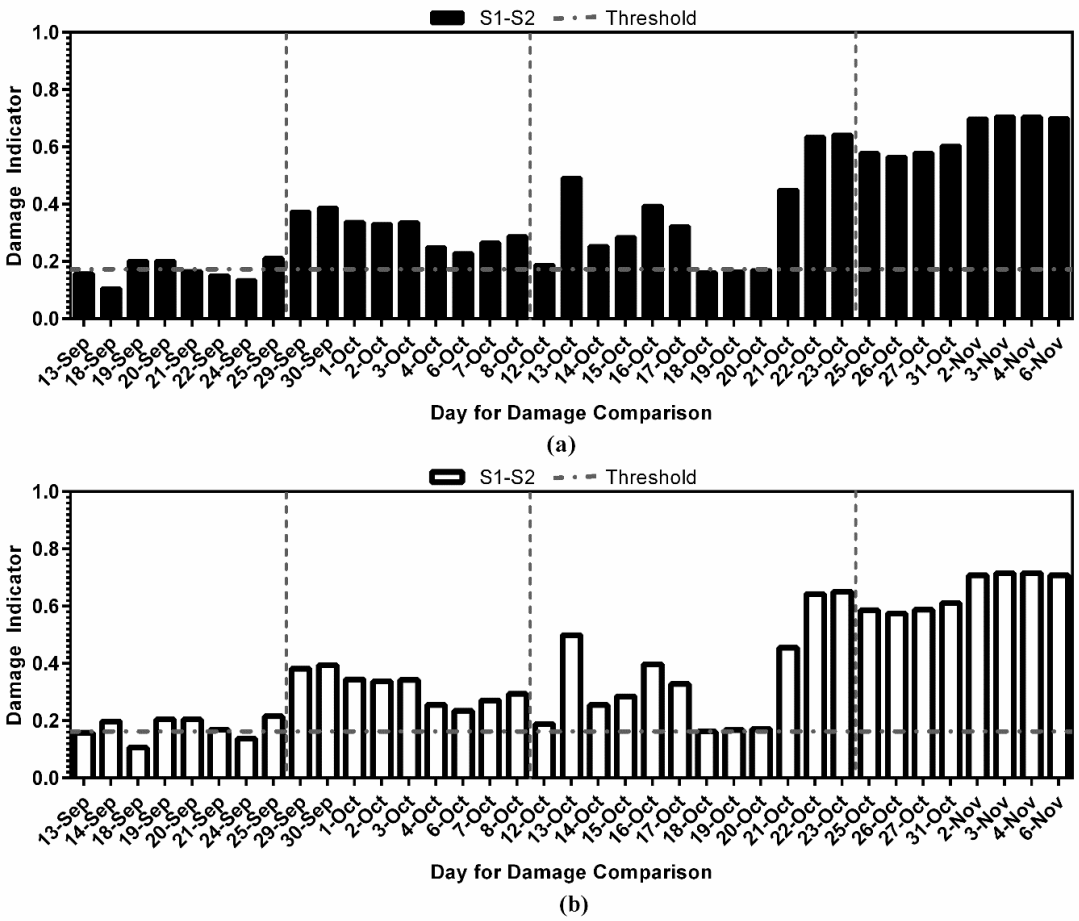

Figure 65 Damage indicator of traffic data for multiple days compared to baseline set for sacrificial specimen: (a) baseline set comprised from 14-Sep (19 °C), (b) baseline set comprised from 22-Sep (12 °C). Refer to Figure 16 for sensor locations. Vertical dashed lines refer to creation/propagation of damage

Each of the damage states is grouped separately to clearly show the relationship between damage severities. A linear regression line has been fitted to the data to observe any relationship between damage indicator and temperature.

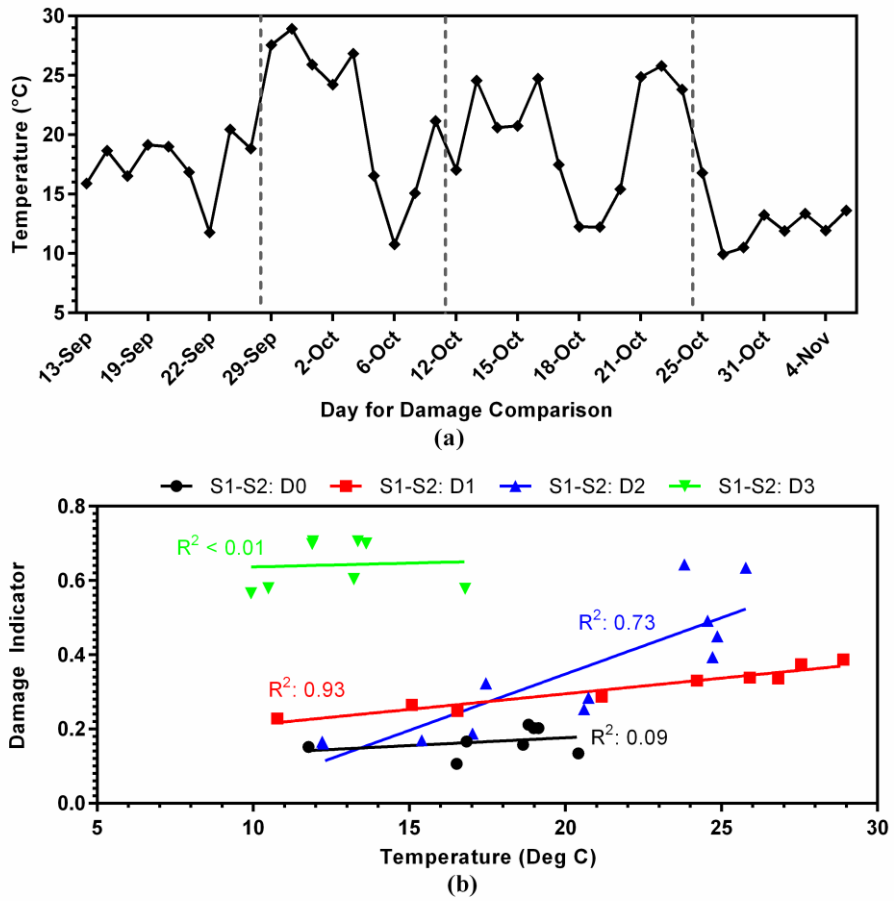

Figure 66 (a) Average daily temperature of steel floor beam for duration of specimen testing. Vertical dashed lines refer to creation/propagation of damage. (b) Damage indicator vs average daily temperature for multiple damage states with linear regression lines for each damage state

5.4.1.2. Section A Operational Load Results

Following the same procedure as that used for the sacrificial specimen, the acceleration data from the traffic vibrations were used to determine the transmissibility between the pair of sensors A5-A1 (Figure 21).

Each day of data (set of 1440 data files) was used for comparison, and the damage indicator was calculated based on these evaluations. The damage indicators, as compared to the baseline set (27 November 2012), are shown in Figure 26(a). The threshold was constructed for a basis containing the first two weeks of data. The results did not show

any damage indicator crossing the threshold, except for two days (10-Mar and 11-Mar). As per the algorithm, this day would not send a warning alarm (as the prior seven days did not exceed the threshold), nor would a watch alarm be given (as the prior three days did not exceed the threshold). Two other days were chosen as baseline sets (3-Dec and 24-Jan) in order to observe the effect of temperature on the damage indicator. These days were chosen because they represent the extremes for temperature variation (3-Dec was the day with the highest temperature recorded for the testing duration (14 °C), and 24-Jan was the coldest day (-9 °C)). The plots of these investigations are in Figure 26(b) and 26(c), respectively. Similar to the 27-Nov baseline set, the analysis with these new baselines shows that the damage indicator does not exceed the threshold for the majority of the testing, and that alarms would not be given due to the non-consecutive threshold violation. From these observations, it can be concluded that damage is not detected on Section A for the entirety of the work completed, which is consistent with the physical health condition of that portion of the bridge.

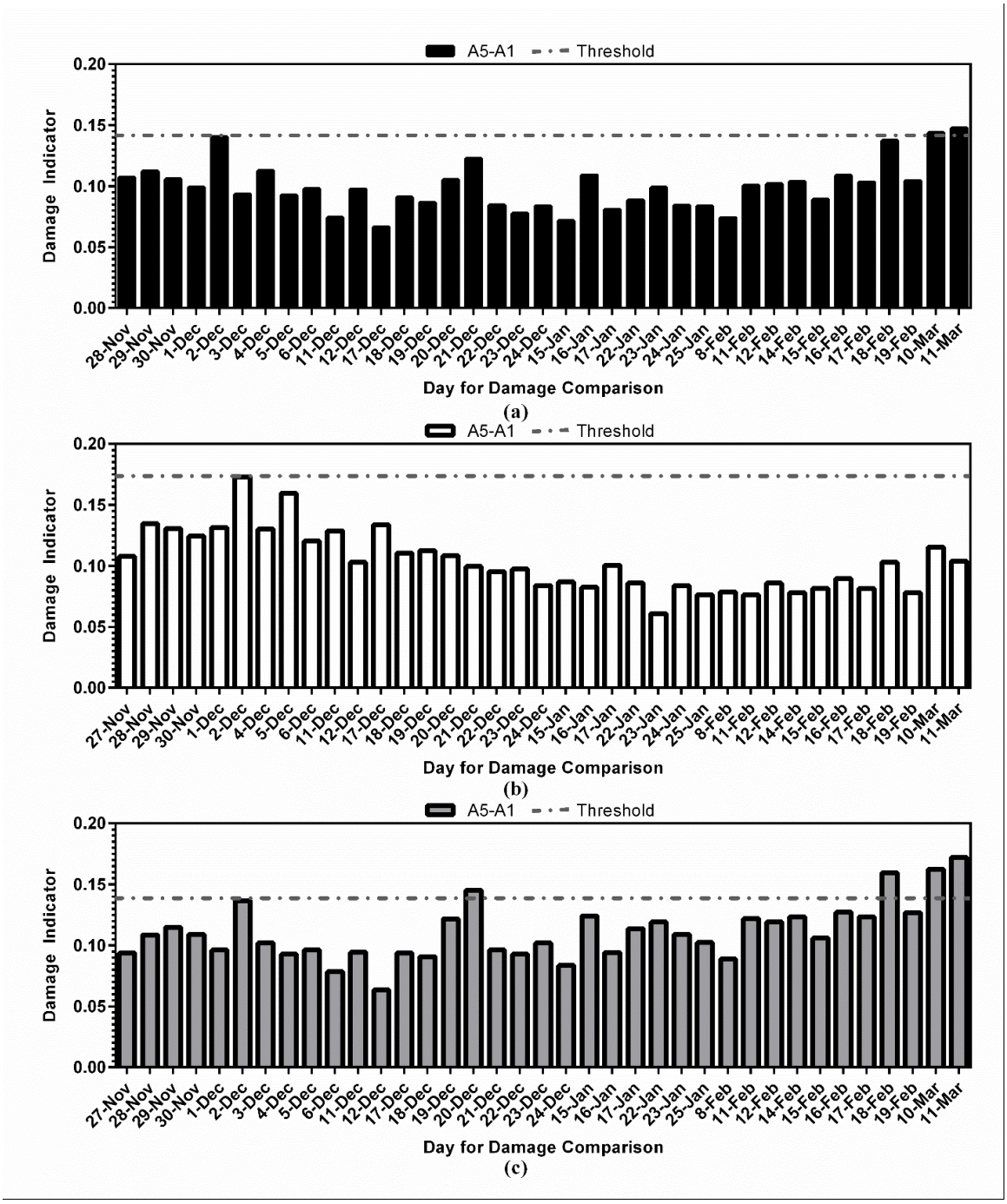

Figure 67 Damage indicators of traffic data for multiple days compared to baseline set for sensors at Section A: (a) baseline set comprised from 27-Nov (3 °C), (b) baseline set comprised from 3-Dec (14 °C), (c) baseline set comprised from 24-Jan (-9 °C). Refer to Figure 21 for sensor locations

The relationship between the variation trend in the damage indicator (Figure 26(a)) and temperature changes (15 °C to -10 °C during the testing period of 28-Nov to 11-Mar) presented in Figure 68(a) depicts characteristics similar to those of the specimen, indicating again that the temperature changes created some uncertainties in the bridge response; however, the damage indicator remained under the threshold that was objectively selected.

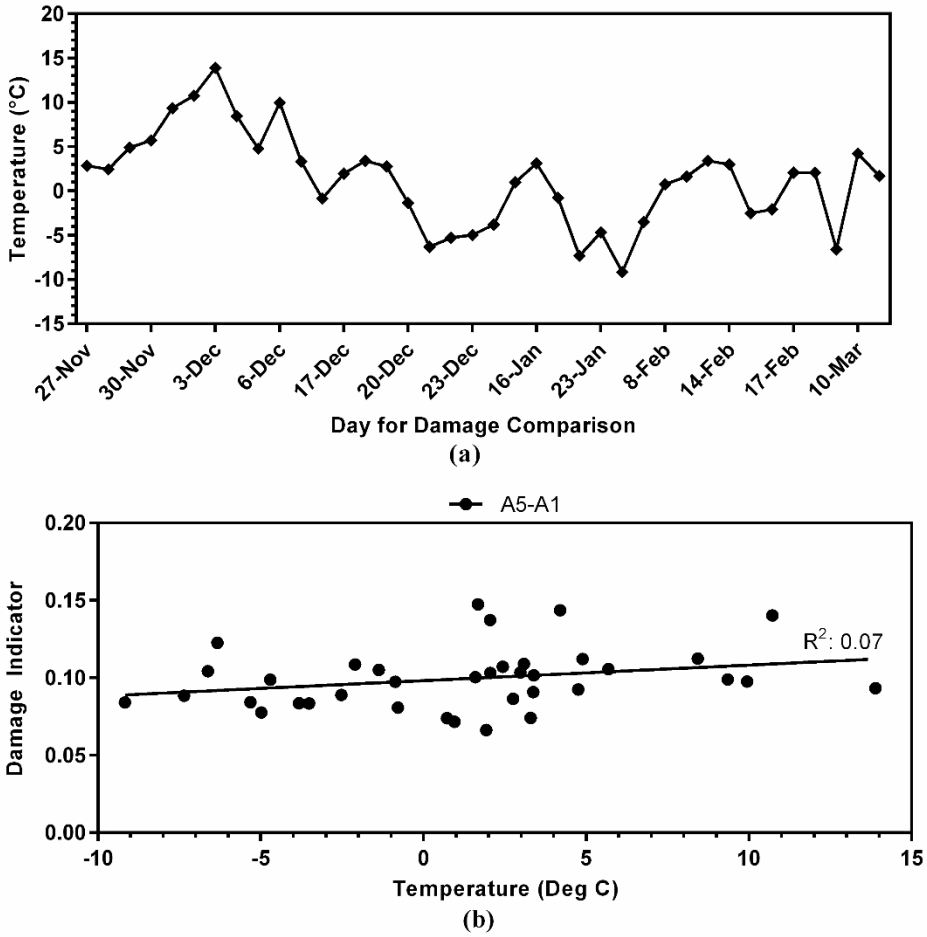

Figure 68 (a) Average daily temperature of steel floor beam for duration of Section A testing. (b) Damage indicator vs average daily temperature with regression line

Figure 68(b) shows the relationship between the variation in damage indicator and temperature for Section A. Again, the results showed scattered points that may be fitted with a regression line (R^2=0.07). This characteristic is similar, to a certain degree, to that of the specimen in Figure 66(b), with significant changes in damage indicator with some temperatures.

5.5. Overall Results and Discussion for Effect of Temperature

From the numerical results, it is observed that as the temperature changes from the baseline temperature (21 °C), the damage indicator for the undamaged specimen increases. This temperature change can be in either direction, hotter or colder, and will cause this increase in the damage indicator. It is noted, however, that this trend is not monotonic for the undamaged pair of nodes 2-3, where a low point arises at 10 °C. One possible explanation for this could be due to the anti-symmetric loading on the specimen causing this non-similar behavior between symmetric pairs of nodes. As for the damage indicators for the damaged specimen, the inverse can be seen in that as the absolute change in temperature increases, the damage indicator decreases. This tendency occurs in both pairs of nodes without abnormalities or deviations.

By comparing the numerical results with those from the experimental testing, it can be seen that both results behave in a similar manner. For both analyses, the temperature does create fluctuations in the damage indicator for the undamaged states, and these fluctuations increase as the change in temperature rises, as seen by the greatest magnitude of damage indicator at the extreme temperatures. Also, both analyses show that the damaged state can be visibly distinguished from the undamaged state. The horizontal dashed lines in Figure 56 and Figure 64 have the sole purpose of illustrating this claim. The fluctuations in the damage indicators can be quantified by calculating the standard deviation for each damage state. The variation in the undamaged numerical structure (standard deviation of 0.068 and 0.103 for pairs 2-1 and 2-3, respectively) is more than that of the damaged numerical structure (standard deviation of 0.047 for both pairs), which suggests that the effect of temperature causes greater variability for the undamaged structure. This is the reverse for the experimental analysis, with the standard deviations being calculated as 0.008 for both pairs of the undamaged structure and 0.035 and 0.028

for pairs 2-1 and 2-3, respectively, for the damaged structure. It is observed that even though temperature does cause variability to the damage indicator, the presence of damage significantly (P-value < 0.001 for all scenarios) overweighs this variability. To further investigate this claim and to observe whether or not the baseline temperature has an effect on the methodology, the same damage indicator calculations were completed using the extreme temperatures in lieu of an average temperature. The numerical results using extreme cold as the baseline (-34 °C) are shown in Figure 69, and the numerical results using extreme hot as the baseline (49 °C) are shown in Figure 70.

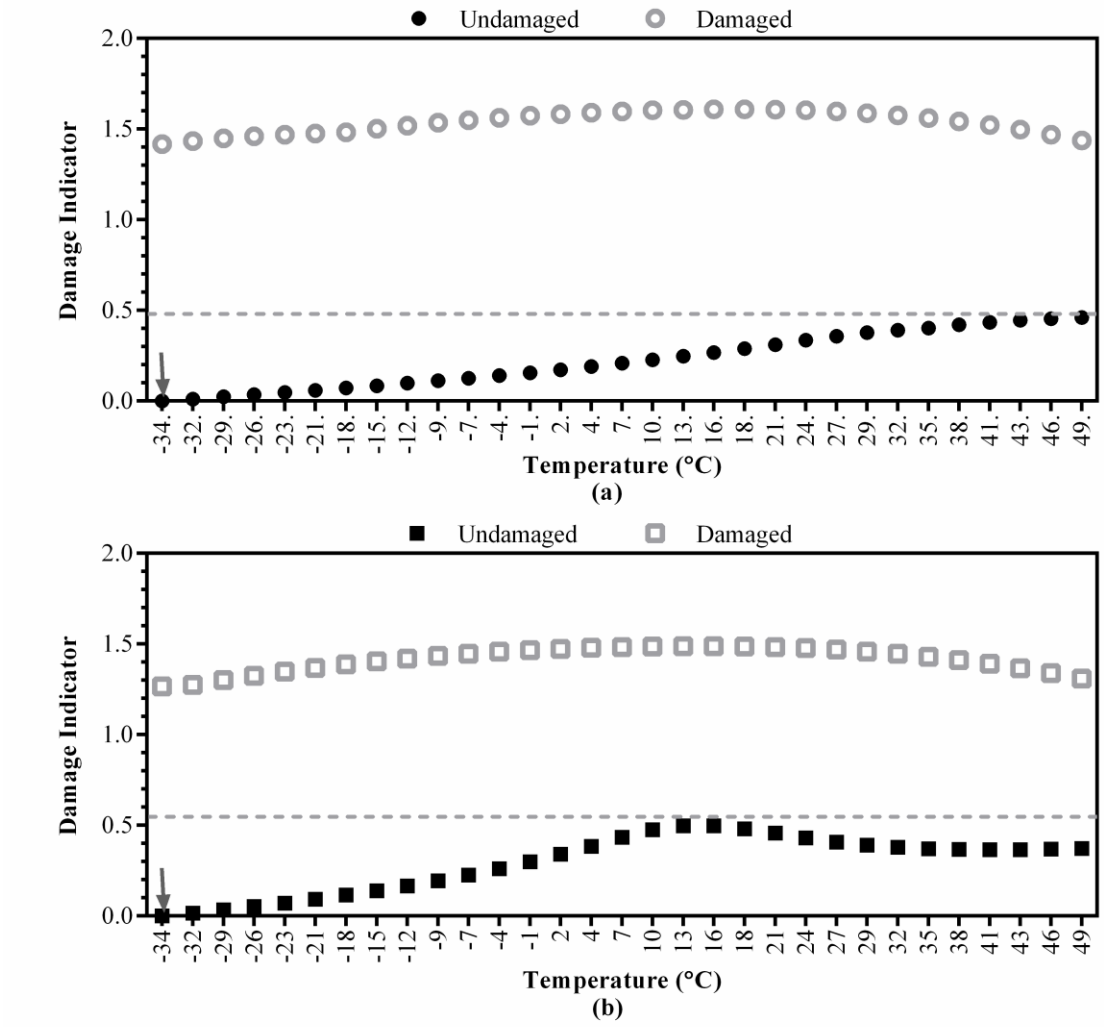

Figure 69 Damage indicator versus temperature for numerical testing. Note: the dark gray arrow points to the baseline temperature. (a) for pair 2-1 with both damage states, (b) for pair 2-3 with both damage states

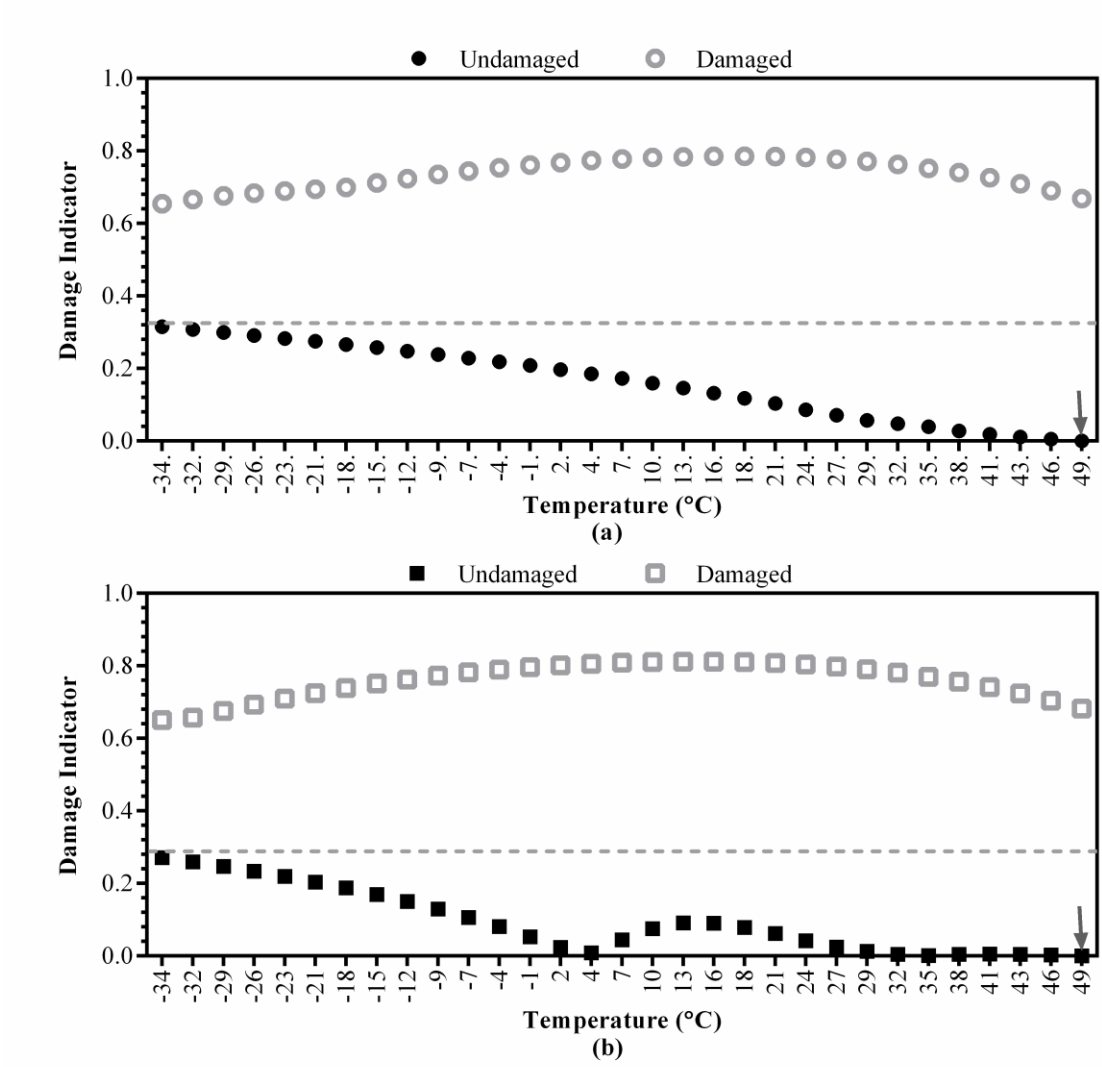

Figure 70 Damage indicator versus temperature for numerical testing. Note: the dark gray arrow points to the baseline temperature. (a) for pair 2-1 with both damage states, (b) for pair 2-3 with both damage states

A similar test was conducted using the data from the experimental testing and the result is shown in Figure 71. It is noted that since the experimental results were calculated from two sets of data (cold and hot), the entire range could not be analyzed from a single extreme temperature. Figure 71 shows the damage indicator for the cold set with the baseline of -1 °C to the left of the dark gray vertical line, and also shows the hot set with the baseline of 43 °C to the right of the dark gray vertical line.

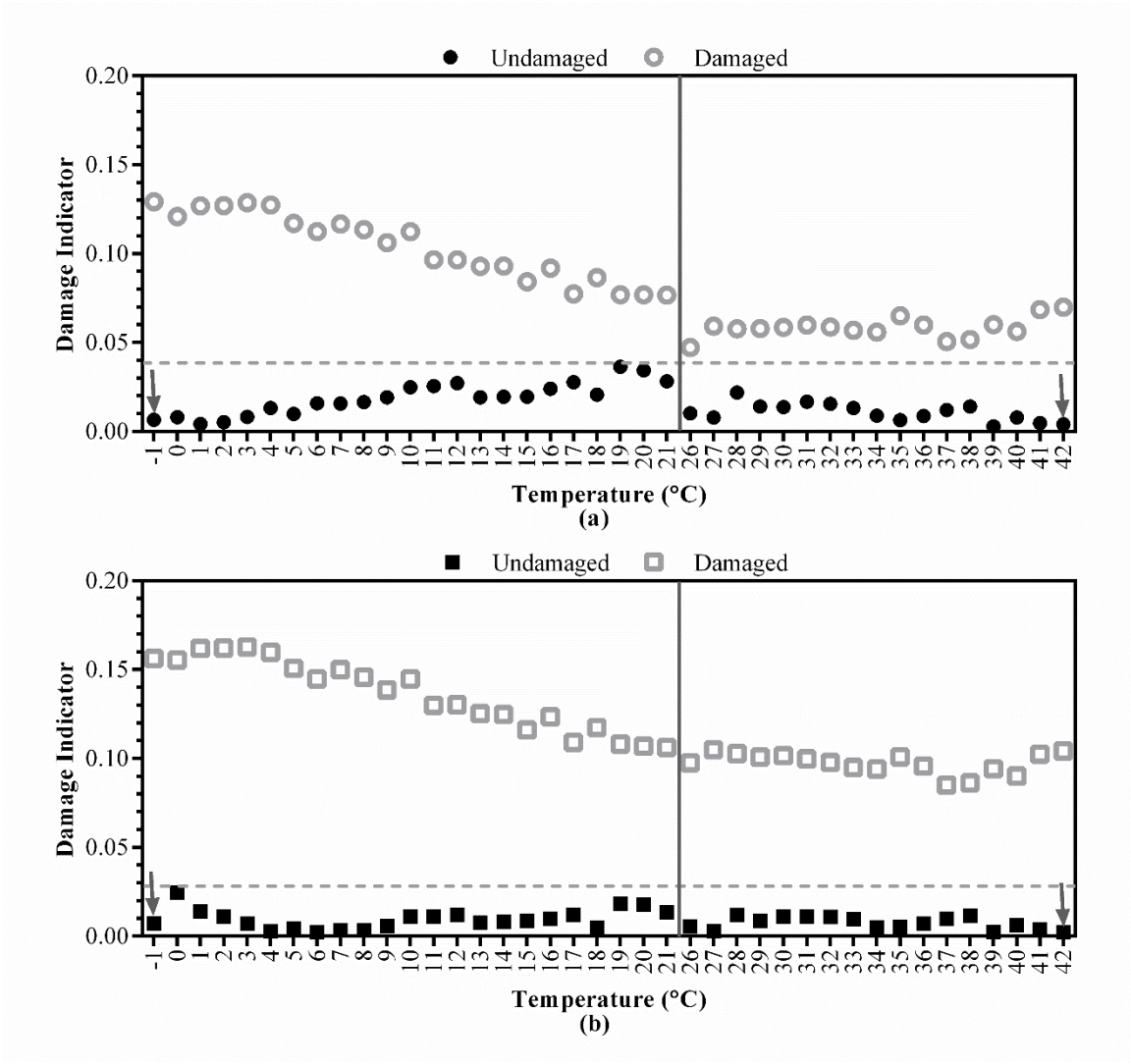

Figure 71 Damage indicator versus temperature for experimental testing. Note: the dark gray arrows point to the baseline temperatures and the dark gray line separates the 'Cold' and 'Hot' data sets. (a) for pair 2-1 with both damage states, (b) for pair 2-3 with both damage states

From these graphs, it can be seen that regardless of the temperature of the baseline, the significance that damage has on the damage indicator clearly outweighs the variability of the environmental effects (P-value < 0.0001 for all scenarios). This observation has very important potential for structural health monitoring methodologies due to the fact that a baseline set of data could be measured at any temperature and damage could be identified

even with changes in the environment. It is also observed from these graphs that there may not be any specific range of temperatures that cause sensitivity to the damage indicator; however, the sensitivity most likely stems from large deviations in temperature from the baseline since the majority of the fluctuations with the damage indicator occur at temperatures away from the baseline.

For the field results, the baseline set was selected as the first day of testing for convenience purposes. However, this day can be arbitrarily selected and therefore can affect the threshold determined from healthy data depending on the time of the year the monitoring process begins. Additional investigation has shown that by choosing a different day as the baseline set (3-Dec and 24-Jan, which had a high percent-violation) for the analysis on Section A, the algorithm did not give a warning alarm, nor a watch alarm. Results based on selecting baseline days with the warmest (3-Dec) and coldest (24-Jan) days of the testing period of Section A did not show signs of alarms. It was found that the choice of the coldest day had generated a high threshold, which may mask small cracks and may generate difficulties in detecting damage. Nevertheless, the results from Figure 23 of the sacrificial specimen testing have indicated that damage can be identified. Based on these results, it may be more appropriate to select the baseline day using a day with a moderate average daily temperature rather than days with extreme temperatures.

Figure 66(a) and Figure 68(a) show some similarities between the temperature's variation trend and those of the damage indicator for the specimen and Section A, respectively. Trends in the regression line for the specimen (Figure 66(b)) and Section A (Figure 68(b)) have suggested a weak increasing trend in the damage indicators with temperature (R^2 ranged from 0.01 to 0.93). Still, in both cases, significant variations in the damage indicator were observed with days that have similar temperature. These results indicate that the damage indicator may also be sensitive to other parameters besides the temperature, including the variation in the loading conditions and other unknown parameters such as noise.

Chapter 6. Conclusion

This work presented a methodology to monitor the health condition of highway steel-girder bridges. The methodology combines the transmissibility function, coherence function, and probabilistic schemes and calculated a damage indicator that gives critical information about the health condition of the bridge. The importance and major contribution of this work is that the coherence function has been proven numerically, experimentally, and in the field to focus the transmissibility on regions where damage significantly outweighs geometric and environmental effects. The functionality that damage can be detected in field applications of this methodology contributes greatly to the already extensive knowledge on this subject. Another function of this methodology is the capability to detect multiple damage locations in simple structures.

This damage indicator has been shown, through this work, to be a useful tool for damage detection. The coherence function is calculated to objectively determine regions of transmissibility that could be trusted for repeatability, in that the signals within the selected regions maintain a near-linear relationship. The probabilistic schemes used within the field testing portion of this algorithm allow for the threshold to be determined equitably by placing an upper limit on a large set of healthy data, thus encompassing many of the uncertainties that can arise.

Based on the numerical and experimental analyses, it is concluded that the presented coherence-based damage-detection algorithm can accurately detect, comparatively locate, and relatively quantify damage for complex structures and damage severities. Damage is correctly not detected when comparing with additional impacts from the baseline state, and damage is clearly detected for any damage state by observing the significant increase in the magnitude of the damage indicator. A relative quantification can be perceived, in that the greater the magnitude of the damage indicator, the greater the change in the dynamic characteristics from the baseline set. Damage can also be comparatively located by assessing the difference in magnitudes of the damage indicator between symmetric pairs of sensors. A greater magnitude is caused by more significant changes in the dynamic characteristics of the structure.

In general, the presented algorithm proved successful in detecting fatigue crack initiation and propagation before retrofitting, as well as crack branching after retrofitting. One significant benefit to this algorithm is the ability to arbitrarily choose the baseline set, e.g. the ability to set the baseline as any state, healthy or damaged, and still maintain accurate damage detection. That gives the proposed method the potential to be used as a prognostic tool for monitoring structures with different initial damage conditions.

Field results using stochastic operational traffic loading during the period of mid-September 2012 to mid-March 2013 have indicated the capability of the proposed methodology in evaluating the changes in the health condition of a section of the bridge, and in consistently detecting cracks of various sizes on a sacrificial specimen integrated with the bridge abutment and a floor beam.

In states with extreme fluctuation in environmental and loading conditions, large variation in the response data is expected, including when monitoring healthy data, which may generate different forms of uncertainty in the decision-making process on bridge maintenance. Therefore, the implementation of an objective threshold that generates watch and warning alarms becomes a very important measure in reducing the uncertainties in detecting damage. While this is a real concern, redundancy in the bridge design allows for operative structural integrity, even after damage can be detected, albeit for a short duration.

Overall, the presented damage-detection algorithm has shown success in detecting small abnormalities in the all facets of analysis, i.e. numerically, experimentally, and in the field under both controlled loading and operational loading scenarios. Also, the use of an objective threshold for the field analyses in combination with the detection decision process allocates alarm severities, i.e., watch and warning alarms, thus allowing for variations in environmental and loading characteristics without causing false warnings. The significance of the threshold is observed through the analysis of Section A, in which damage was correctly not identified, even though environmental and loading conditions were fluctuating. It should be noted that the false damage-detection testing on Section A was limited to false positive detection (damage detected when no damage on bridge) and

that false negative detection (damage not detected when damage on bridge) could not be investigated.

Results have shown that the effects of force location and sensor orientation do contribute to the damage detection algorithm. It has been shown that although force location does affect the frequency response function and transmissibility, a damage detection methodology based on these parameters is still able to accurately detect damage by choosing an excitation location away from the damage location. This conclusion was shown numerically on a 5 degree-of-freedom spring-mass system where damage was clearly seen regardless of force location for both FRF and transmissibility. It is noted that more useful results appeared when the force was applied at the response location for the FRF analysis, and when the force was applied away from the damage location for the transmissibility analysis.

Using the presented damage indicator algorithm, multiple damage states were successfully detected, located and relatively quantified for non-dispersive systems with different boundary conditions by applying the force at a node away from the damage. This positively correlates with the results seen with the dispersive system for the transmissibility analysis in that the better results occurred when the force was applied away from damage. This methodology also was successful in identifying dual-damage locations by utilizing this same principle. When applying the force near the location of damage, the damage indicator could not accurately detect the damage and would also falsely detect damage at other positions.

The completed analysis showed that the monitoring process can potentially be completed using two sensors; however, the results from the sensitivity analysis have demonstrated the critical role of sensor locations and orientations. It is expected that the monitoring process will become more efficient when utilizing two sensors with optimal locations and orientations. From the results of the completed analyses, it has been observed that placing the sensors near the damage location will provide accurate detection results, as long as the force is applied away from the damage. It was also observed that the load path also has an effect on the orientation in which the sensors should be placed. These observations suggest that it would be more advantageous to place both sensors close to

the damage-critical area and have both oriented such that the signal-to-noise ratio is the greatest (the majority of the time, this will be in the direction of the load application). The reason for this is based on the perception that accelerometers have global and local sensitivity to damage. By placing one sensor close to the damage-critical area, this sensor may become more sensitive to the damage than the other sensor; thus, damage features may be magnified and more easily detected.

Temperature variability is a large uncertainty parameter for many damage detection methodologies, especially for field applications; however, the presented work has shown that while temperature does cause variability to the damage indicator, the presence of damage significantly outweighs this inconsistency by focusing on regions of high coherence. By comparing the numerical results with those from the experimental testing, it can be seen that both results behave in a similar manner. For both analyses, the temperature does create relatively small fluctuations in the damage indicator for the undamaged states, and these fluctuations increase as the change in temperature rises, as seen by the greatest magnitude of damage indicator at the extreme temperatures. Also, both analyses show that the damaged state can be visibly distinguished from the undamaged state. The fluctuations in the damage indicators can be quantified by calculating the standard deviation for each damage state. The variation in the undamaged numerical structure is more than that of the damaged numerical structure, which suggests that the effect of temperature causes greater variability for the undamaged structure. It is observed that even though temperature does cause variability to the damage indicator, the presence of damage significantly outweighs this variability.

Results have shown that regardless of the temperature of the baseline, the significance that damage has on the damage indicator clearly outweighs the variability of the environmental effects. This observation has very important potential for structural health monitoring methodologies due to the fact that a baseline set of data could be measured at any temperature, and damage could be identified even with changes in the environment. It is also observed from these graphs that there may not be any specific range of temperatures that cause sensitivity to the damage indicator; however, the sensitivity most

likely stems from large deviations in temperature from the baseline since the majority of the fluctuations with the damage indicator occur at temperatures away from the baseline.

For the field results, the baseline set was selected as the first day of testing for convenience purposes. However, this day can be arbitrarily selected and therefore can affect the threshold determined from healthy data depending on the time of the year the monitoring process begins. Additional investigation has shown that by choosing a different day as the baseline set (3-Dec and 24-Jan) for the analysis on Section A, the algorithm did not give a warning alarm, nor a watch alarm. Results based on selecting baseline days with the warmest (3-Dec) and coldest (24-Jan) days of the testing period of Section A did not show signs of alarms. It was found that the choice of the coldest day generated a high threshold, which may mask small cracks and may generate difficulties in detecting damage. Nevertheless, the results of the sacrificial specimen testing have indicated that damage can be identified. Based on these results, it may be more appropriate to select the baseline day using a day with a moderate average daily temperature rather than days with extreme temperatures.

Bibliography

1. Deficient Bridges by State and Highway System (2012). Available from: http://www.fhwa.dot.gov/bridge/nbi/no10/defbr12.cfm.
2. Connor, R.J. and Fisher, J.W. (2006), "Identifying effective and ineffective retrofits for distortion fatigue cracking in steel bridges using field instrumentation", *Journal of Bridge Engineering*, **11**(6), 745-752.
3. Haghani R, Al-Emrani M, and Heshmati M. (2012), "Fatigue-prone details in steel bridges." *Buildings*. **2**(4):456-76.
4. United States Department of Transportation (2013), Manual for repair and retrofit of fatigue cracks in steel bridges. FHWA Publication No. FHWA-IF-13-020.
5. Wipf, T.J., Greimann, L.F., Phares, B., and Tarries, D. (2003), Retrofit methods of distortion cracking problems in plate girder bridges. Iowa DOT Project No. TR-436.
6. Grondin, G.Y. and Kulak, G.L. (2010), "Distortion-induced fatigue cracking of bridge girders—design issues", In *ASCE Structures Congress 2010*, 484-495.
7. Cousins, T. E., Stallings, J.M., Lower, D.A., and Stafford, T.E. (1998), "Field evaluation of fatigue cracking in diaphragm-girder connections", *Journal of Performance of Constructed Facilities*, **12**(1), 25-32.
8. Wipf, T.J., Greimann, L.F., Khalil, A.H., and Wood, D. (1998), Preventing cracking at diaphragm/plate girder connections in steel bridges. No. Iowa DOT Project HR-393.
9. Tarries, D.J. (2002), "Diaphragm bolt loosening retrofit for web gap fatigue cracking in steel girder bridges." PhD Dissertation, Iowa State University, Ames, IA.
10. Rahmatalla, S. and Schallhorn, C. (2013), "Diagnosis of retrofit fatigue crack re-initiation and growth in steel-girder bridges for proactive repair and emergency planning", MATC TRB RiP No. 34765.
11. Adewuyi AP, Wu Z, and Serker NK. (2009), "Assessment of vibration-based damage identification methods using displacement and distributed strain measurements." *Structural Health Monitoring*. **8**(6):443-61.
12. Humar, J., Bagchi, A., and Xu, H. (2006), "Performance of vibration-based techniques for the identification of structural damage", *Structural Health Monitoring*, **5**(3), 215-241.

13. Chang PC, Flatau A, and Liu S. (2003), “Review paper: health monitoring of civil infrastructure.” *Structural Health Monitoring*. **2**(3):257-67.
14. Adams, DE. (2007), “Health monitoring of structural materials and components.” *Methods with Applications*. John Wiley and Sons, Inc.
15. US Department of Transportation, Federal Highway Administration (2012), Deficient Bridges by State and Highway System. Accessed at: http://www.fhwa.dot.gov/bridge/nbi/no10/defbr12.cfm.
16. Fan W, and Qiao P. (2011), “Vibration-based damage identification methods: a review and comparative study.” *Structural Health Monitoring*. **10**(1):83-111.
17. Doebling, S.W., Farrar, C.R., and Prime, M.B. (1998), “A summary review of vibration-based damage identification methods", *Shock and Vibration Digest,* **30**(2), 91-105.
18. Yan, Y.J., Cheng, L., Wu, Z.Y., and Yam L.H. (2007), "Development in vibration-based structural damage detection technique", *Mechanical Systems and Signal Processing,* **21**(5), 2198-2211.
19. Chesné, S. and Deraemaeker, A. (2013), “Damage localization using transmissibility functions: a critical review." *Mechanical Systems and Signal Processing,* **38**(2), 569-584.
20. Rahmatalla, S., Hudson, K., Liu, Y., and Eun, H-C. (2014), “Finite element modal analysis and vibration-waveforms in health inspection of old bridges”, *Finite Elements in Analysis and Design,* **78**, 40-46.
21. Rytter A. (1993), “Vibrational based inspection of civil engineering structures”, *Ph.D. Dissertation*, Department of Building Technology and Structural Engineering, Aalborg University, Denmark.
22. Maia, N., Silva, J., Almas, E., and Sampaio, R. (2003), “Damage detection in structures: from mode shape to frequency response function methods”, *Mechanical Systems and Signal Processing*, **17**(3), 489-498.
23. Thyagarajan, S. K., Schulz, M.J., Pai, P.F., and Chung, J. (1998), "Detecting structural damage using frequency response functions", *Journal of Sound and Vibration*, **210**(1), 162-170.

24. Abdel Wahab, M. and De Roeck, G. (1999), “Damage detection in bridges using modal curvatures: application to a real damage scenario”, *Journal of Sound and Vibration*, **226**(2), 217-235.
25. Pandey, A., Biswas, M., and Samman, M. (1991), “Damage detection from changes in curvature mode shapes”, *Journal of Sound and Vibration*, **145**(2), 321-332.
26. Cruz, P.J. and Salgado, R. (2009), “Performance of vibration-based damage detection methods in bridges”, *Computer-Aided Civil and Infrastructure Engineering*, **24**(1), 62-79.
27. Johnson T, Adams D, and Schiefer M. (2002), “An analytical and experimental study to assess structural damage and integrity using dynamic transmissibility.” *The Proceedings of the 20th International Modal Analysis Conference*.
28. Maia, N.M.M., Urgueira, A.P.V., and Almeida, R.A.B. (2011), "Whys and wherefores of transmissibility", Chapter 10: 197-216. Vibration Analysis and Control - New Trends and Developments, Dr. Francisco Beltran-Carbajal (Ed.), ISBN: 978-953-307-433-7, InTech, DOI: 10.5772/24869. Available from: http://www.intechopen.com/books/vibration-analysis-and-control-new-trends-and-developments/whys-and-wherefores-of-transmissibility.
29. Maia, N.M.M., Almeida, R.A.B., Urgueira, A.P.V., and Sampaio, R.PC. (2011), "Damage detection and quantification using transmissibility", *Mechanical Systems and Signal Processing*, **25**(7), 2475-2483.
30. Devriendt, C. and Guillaume, P. (2008), "Identification of modal parameters from transmissibility measurements", *Journal of Sound and Vibration* **314**(1), 343-356.
31. Johnson, T. J., and Adams, D. E. (2002), “Transmissibility as a differential indicator of structural damage,” *Journal of Vibration and Acoustics*, **124**(4), 634-641.
32. Li, J. and Hao, H. (2013), "Damage detection of shear connectors based on power spectral density transmissibility", *Key Engineering Materials*, 569, 1241-1248.
33. Worden, K. (1997), “Structural fault detection using a novelty measure.” *Journal of Sound and Vibration*. **201**(1):85-101.
34. Worden, K. and Manson, G. (2003), “Experimental validation of structural health monitoring methodology: part 1, novelty detection on a laboratory structure”, *Journal of Sound and Vibration*, **259**(2), 323-343.

35. Kess, H. R., and Adams, D. E. (2007), “Investigation of operational and environmental variability effects on damage detection algorithms in a woven composite plate.” *Mechanical Systems and Signal Processing*, **21**(6), 2394-2405.
36. Sohn, H. (2007), "Effects of environmental and operational variability on structural health monitoring." *Philosophical Transactions of the Royal Society A: Mathematical, Physical and Engineering Sciences* **365**(1851), 539-560
37. Worden, K., Farrar, C. R., Manson, G., and Park, G. (2007). “The fundamental axioms of structural health monitoring.” *Proceedings of the Royal Society A: Mathematical, Physical and Engineering Science*, **463**(2082), 1639-1664.
38. Kerschen, G., Worden, K., Vakakis, A. F., and Golinval, J. C. (2006), “Past, present and future of nonlinear system identification in structural dynamics.” *Mechanical Systems and Signal Processing*, **20**(3), 505-592.
39. Deraemaeker, A., and Preumont, A. (2006), “Vibration based damage detection using large array sensors and spatial filters,” *Mechanical Systems and Signal Processing*, **20**(7), 1615-1630.
40. Yan, A-M., Kerschen, G., De Boe, P., and Golinval, J.C. (2005), "Structural damage diagnosis under varying environmental conditions—part I: a linear analysis." *Mechanical Systems and Signal Processing* **19**(4), 847-864.
41. Worden, K., Farrar, C. R., Haywood, J., and Todd, M. (2008), “A review of nonlinear dynamics applications to structural health monitoring.” *Structural Control and Health Monitoring*, **15**(4), 540-567.
42. Fisher, J.W. (1997), "Evolution of fatigue-resistant steel bridges", *Transportation Research Record: Journal of the Transportation Research Board*, **1594**(1), 5-17.
43. Al-Emrani, M. and Kliger, R. (2003), "FE analysis of stringer-to-floor-beam connections in riveted railway bridges", *Journal of Constructional Steel Research*, **59**(7), 803-818.
44. Lu, Z. and Liu, Y. (2010), "Small time scale fatigue crack growth analysis", *International Journal of Fatigue*, **32**(8), 1306-1321.
45. Liu, M., Frangopol, D.M., and Kwon, K. (2010), “Fatigue reliability assessment of retrofitted steel bridges integrating monitored data", *Structural Safety*, **32**(1), 77-89.

46. Garesci, F., Catalano, L., and Petrone, F. (2006), “Experimental results of a damage detection methodology using variations in modal parameters”, *Experimental Mechanics*, **46**(4), 441-451.
47. Fraraccio, G., Brügger, A., and Betti, R. (2008), “Identification and damage detection in structures subjected to base excitation”, *Experimental Mechanics*, **48**(4), 521-528.
48. Schallhorn, C. and Rahmatalla, S. (2014), “Crack detection and health monitoring of highway steel-girder bridges”, submitted to *Structural Health Monitoring*.
49. Phares, B., Lu, P., Wipf, T., Greimann, L., and Seo, J. (2013), "Field validation of a statistical-based bridge damage-detection algorithm", *Journal of Bridge Engineering,* **18**(11), 1227-1238.
50. Pohlkamp, M. (2010), “An experimental validation of a statistical based damage detection approach”, Master’s Thesis, Iowa State University, Ames, IA.
51. Amiri A, and Allahyari S. (2012), “Change point estimation methods for control chart postsignal diagnostics: a literature review.” *Quality and Reliability Engineering International*. **28**(7):673-85.
52. Fugate ML, Sohn H, and Farrar CR. (2001), “Vibration-based damage detection using statistical process control.” *Mechanical Systems and Signal Processing*. **15**(4):707-21.
53. Kullaa J. (2003), “Damage detection of the Z24 bridge using control charts.” *Mechanical Systems and Signal Processing*. **17**(1):163-70.
54. Mosavi A, Dickey D, Seracino R, and Rizkalla S. (2012), “Identifying damage locations under ambient vibrations utilizing vector autoregressive models and Mahalanobis distances.” *Mechanical Systems and Signal Processing*. **26**:254-67.
55. Wang Z, and Ong K. (2009), “Structural damage detection using autoregressive-model-incorporating multivariate exponentially weighted moving average control chart.” *Engineering Structures*. **31**(5):1265-75.
56. Michaels, J.E., and Michaels, T.E. (2005), “Detection of structural damage from the local temporal coherence of diffuse ultrasonic signals.” *IEEE Transaction of Ultrasonic, Ferroelectrics, and Frequency Control*. **52**(10): 1769-1782.
57. Phares BM, Greimann L, and Choi H. (2013), “Integration of bridge damage detection concepts and components volume I: strain-based damage detection.”

58. Rahmatalla S, Schallhorn C, and Swadi G. (2013), “Integration of bridge damage detection concepts and components volume II: acceleration-based damage detection.”
59. ASTM Standard D5265. (2009), “Standard test method for bridge impact testing.” *ASTM International*.
60. ASTM Standard E122e1. (2009), “Standard practice for calculating sample size to estimate, with specified precision, the average for a characteristic of a lot of process.” *ASTM International*.
61. Zhao, J., and DeWolf, J.T. (2002), "Dynamic monitoring of steel girder highway bridge." *Journal of Bridge Engineering* **7**(6), 350-356.
62. Mosavi, A.A., Seracino, R., and Rizkalla, S. (2012), “Effect of temperature on daily modal variability of a steel-concrete composite bridge,” *Journal of Bridge Engineering*, **17**(6), 979–983.
63. Kim, J.T., Park, J.H., and Lee, B.J. (2007), “Vibration-based damage monitoring in model plate-girder bridges under uncertain temperature conditions,” *Engineering Structures*, **29**(7), 1354–1365.
64. Peeters, B., Maeck, J., and De Roeck, G. (2001), “Vibration-based damage detection in civil engineering: excitation sources and temperature effects,” *SmartMaterials and Structures*, **10**(3), 518–527.
65. Farrar, C.R., Doebling, S.W., Cornwell, P.J., and Straser, E.G. (1997), “Variability of modal parameters measured on the Alamosa Canyon Bridge,” in *Proceedings of the 15th International Modal Analysis Conference (IMAC ’97)*, 257–263.
66. Cornwell, P., Farrar, C.R., Doebling, S.W., and Sohn, H. (1999), “Environmental variability of modal properties,” *Experimental Techniques*, **23**(6), 45–48.
67. Moser, P., and Moaveni, B. (2011), “Environmental effects on the identified natural frequencies of the dowling hall footbridge,” *Mechanical Systems and Signal Processing*, **25**(7), 2336–2357.
68. Xu, Z-D., and Wu, Z. (2007), "Simulation of the effect of temperature variation on damage detection in a long-span cable-stayed bridge." *Structural Health Monitoring* **6**(3), 177-189.

69. Ding, Y.L., and Li, A.Q. (2011), “Temperature-induced variations of measured modal frequencies of steel box girder for a long-span suspension bridge,” *International Journal of Steel Structures*, **11**(2), 145–155.
70. Liu, C., and DeWolf, J.T. (2007), “Effect of temperature on modal variability of a curved concrete bridge under ambient loads,” *Journal of Structural Engineering*, **133**(12), 1742–1751.
71. Gonzales, I., Ulker-Kaustell, M.,, and Karoumi, R. (2013), “Seasonal effects on the stiffness properties of a ballasted railway bridge,” *Engineering Structures*, **57**, 63–72.
72. Yan, A-M., Kerschen, G., De Boe, P., and Golinval, J.C. (2005), "Structural damage diagnosis under varying environmental conditions—part II: local PCA for non-linear cases." *Mechanical Systems and Signal Processing* **19**(4), 865-880.
73. Kim, C. Y., Jung, D. S., Kim, N. S., Kwon, S. D., and Feng, M. Q. (2003). “Effect of vehicle weight on natural frequencies of bridges measured from traffic-induced vibration.” *Earthquake Engineering and Engineering Vibration*, **2**(1), 109-115.
74. Cawley, P. (1997). “Long range inspection of structures using low frequency ultrasound.” *Structural Damage Assessment Using Advanced Signal Processing Procedures*, 1-17.
75. Quek, S. T., Wang, Q., Zhang, L., and Ang, K. K. (2001). “Sensitivity analysis of crack detection in beams by wavelet technique.” *International Journal of Mechanical Sciences*, **43**(12), 2899-2910.
76. Carrella, A., and Ewins, D. J. (2011), “Identifying and quantifying structural nonlinearities in engineering applications from measured frequency response functions.” *Mechanical Systems and Signal Processing*, **25**(3), 1011-1027.
77. Pai, P. F., Huang, L., Hu, J., and Langewisch, D. R. (2008), “Time-frequency method for nonlinear system identification and damage detection.” *Structural Health Monitoring*, **7**(2), 103-127.
78. D’Souza, K., and Epureanu, B. I. (2005), “Damage detection in nonlinear systems using system augmentation and generalized minimum rank perturbation theory.” *Smart Materials and Structures*, **14**(5), 989.

79. Mojtahedi, A., Yaghin, L., Ettefagh, M. M., Hassanzadeh, Y., and Fujikubo, M. (2013), "Detection of nonlinearity effects in structural integrity monitoring methods for offshore jacket-type structures based on principal component analysis." *Marine Structures*, **33**, 100-119.
80. Epureanu, B. I., Yin, S. H., and Derriso, M. M. (2005), "High-sensitivity damage detection based on enhanced nonlinear dynamics." *Smart Materials and Structures*, **14**(2), 321.
81. Masri, S. F., Mariamy, Y. A., and Anderson, J. C. (1981), "Dynamic response of a beam with a geometric nonlinearity." *Journal of Applied Mechanics*, **48**(2), 404-410.
82. Pai, P. F., and Palazotto, A. N. (1996), "Large-deformation analysis of flexible beams." *International Journal of Solids and Structures*, **33**(9), 1335-1353.
83. Adeli, H., and Zhang, J. (1995), "Fully nonlinear analysis of composite girder cable-stayed bridges." *Computers and Structures*, **54**(2), 267-277.
84. Hua, X. G., Ni, Y. Q., Chen, Z. Q., and Ko, J. M. (2009), "Structural damage detection of cable-stayed bridges using changes in cable forces and model updating." *Journal of Structural Engineering*, **135**(9), 1093-1106.
85. Manoach, E., and Trendafilova, I. (2008), "Large amplitude vibrations and damage detection of rectangular plates." *Journal of Sound and Vibration*, **315**(3), 591-606.
86. Adams, D. E., and Farrar, C. R. (2002), "Classifying linear and nonlinear structural damage using frequency domain ARX models." *Structural Health Monitoring*, **1**(2), 185-201.
87. Milovanovic, Z., Kovacic, I., and Brennan, M. J. (2009), "On the displacement transmissibility of a base excited viscously damped nonlinear vibration isolator." *Journal of Vibration and Acoustics*, **131**(5), 054502.
88. Carrella, A., Brennan, M. J., Waters, T. P., and Lopes Jr, V. (2012), "Force and displacement transmissibility of a nonlinear isolator with high-static-low-dynamic-stiffness." *International Journal of Mechanical Sciences*, **55**(1), 22-29.
89. Guo, P. F., Lang, Z. Q., & Peng, Z. K. (2012), "Analysis and design of the force and displacement transmissibility of nonlinear viscous damper based vibration isolation systems." *Nonlinear Dynamics*, **67**(4), 2671-2687.